SHAPE MEMORY RESPONSE OF Ni_2MnGa AND NiMnCoIn MAGNETIC SHAPE MEMORY ALLOYS UNDER COMPRESSION

A Thesis

by

ANDREW LEE BREWER

Submitted to the Office of Graduate Studies of
Texas A&M University
in partial fulfillment of the requirements for the degree of

MASTER OF SCIENCE

May 2007

Major Subject: Mechanical Engineering

SHAPE MEMORY RESPONSE OF Ni_2MnGa AND NiMnCoIn MAGNETIC SHAPE MEMORY ALLOYS UNDER COMPRESSION

A Thesis

by

ANDREW LEE BREWER

Submitted to the Office of Graduate Studies of
Texas A&M University
in partial fulfillment of the requirements for the degree of

MASTER OF SCIENCE

Approved by:

Chair of Committee,	Ibrahim Karaman
Committee Members,	Richard Griffin
	Zoubeida Ounaies
Head of Department,	Dennis O'Neal

May 2007

Major Subject: Mechanical Engineering

ABSTRACT

Shape Memory Response of Ni_2MnGa and NiMnCoIn Magnetic Shape Memory Alloys Under Compression. (May 2007)

Andrew Lee Brewer, B.S., University of New Mexico

Chair of Advisory Committee: Dr. Ibrahim Karaman

In this study, the shape memory response of Ni_2MnGa and NiMnCoIn magnetic shape memory alloys was observed under compressive stresses. Ni_2MnGa is a magnetic shape memory alloy (MSMA) that has been shown to exhibit fully reversible, stress-assisted magnetic field induced phase transformation (MFIPT) in the I ↔ X-phase transformation because of a large magnetostress of 7 MPa and small stress hysteresis. The X-phase is a recently discovered phase that is mechanically induced, however, the crystal structure is unknown. To better understand the transformation behavior of Ni_2MnGa single crystal with [100] orientation, thermal cycling and pseudoelasticity tests were conducted with the goal of determining the Clausius-Clapeyron relationships for the various phase transformations. This information was then used to construct a stress-temperature phase diagram that illustrates the stress and temperature ranges where MFIPT is possible, as well as where the X-phase may be found.

NiMnCoIn is a recently discovered meta-magnetic shape memory alloy (MMSMA) that exhibits unique magnetic properties. The ferromagnetic parent phase and the paramagnetic martensite phase allow the exploitation of the Zeeman energy. To gain a better understanding of the transformation behavior of NiMnCoIn, thermal cycling and pseudoelasticity tests were conducted on single crystals from two different batches with crystallographic orientations along the [100](011), [087], and [25 7 15] directions. A stress-temperature phase diagram was created that illustrates the Clausius-Clapeyron relationships for each orientation and batch. SQUID tests revealed the magnetic response of the alloy as well as the suppression of the martensite start temperature with increasing magnetic field. Pseudoelasticity experiments with and

without magnetic field were conducted to experimentally quantify the magnetostress as a function of magnetic field. For the first time, it has been shown that NiMnCoIn is capable of exhibiting magnetostress levels of 18-36 MPa depending upon orientation, as well as nearly 6.5% transformation strain in the [100] direction.

The results of this study reveal increased actuation stress levels in NiMnCoIn, which is the main limitation in most MSMAs. With this increased blocking stress, NiMnCoIn is a strong candidate for MFIPT.

To My Family, with Love

ACKNOWLEDGMENTS

First and foremost, I would like to extend my deepest gratitude to my advisor, Professor Ibrahim Karaman, for his help and mentorship throughout the course of this research. Without his encouragement and instruction this research would have never been possible. His high expectations have given me the additional tools needed to become a better engineer, researcher, and critical thinker. Thank you!

I would also like to thank Professor Richard Griffin and Professor Zoubeida Ounaies for being my committee members.

Special thanks to Professor Yuriy Chumlyakov for not only providing the samples used in this experiment, but also for sharing with me his intimate knowledge of shape memory alloys. His insight and guidance have aided me well in this research.

I am also grateful to Bill Merka in the chemistry glass shop for sealing our samples for heat treatment and for his captivating discussions on bow hunting and modern archery technology.

I would like to thank my officemates: Burak Basaran, Haluk Karaca, Benat Kockar, James "Floating Head" Monroe, Cathleen Hutchins, Majid Al-Maharbi, Guven Yapici, Dr. Mohammed Haouaoui, Hans-Gerd Lambers, Andre "Awesome" Leifeld, and Ji Ma for all their help and wonderful social interactions. Special thanks to Burak Basaran, Haluk Karaca, and Professor Karaman for teaching me about their wonderful Turkish culture and to Burak Basaran for giving me the chance to sample delicious Turkish cuisine. I would like to extend particular thanks to Burak Basaran and Haluk Karaca for all of their help and encouragement during this research.

I would also like to thank my friends: 1st Lt. Adam Harris, Bill Harris, Karen Harris, Sara Harris, Kara and Abby Schubert, Kirk Rhoades, Jennifer Brecheisen, Jason Jan, Daniel LaCroix, Dr. Yetzi Urthaler, and Ysidoro "Izzy" Ramirez for their thoughts and prayers, as well as their support.

Lastly, I would like to thank my family for all their love and support; I never would have been able to attempt or complete this research without them. They are my life and I appreciate all they have ever done for me.

TABLE OF CONTENTS

Page

ABSTRACT iii

DEDICATION v

ACKNOWLEDGMENTS vi

TABLE OF CONTENTS vii

LIST OF FIGURES ix

LIST OF TABLES xiv

CHAPTER

I INTRODUCTION 1

1.1 Background 1
1.2 Magnetic Shape Memory Effect 6
1.3 Thermodynamic Framework for Martensitic Transformation 9
1.4 Clausius-Clapeyron Relationship 13
1.5 Brief History of Ni_2MnGa and NiMnCoIn 14

II MOTIVATION AND OBJECTIVES 16

III EXPERIMENTAL TECHNIQUES 21

3.1 Materials and Sample Preparation 21
a. Ni_2MnGa 21
b. NiMnCoIn 21
3.2 Experimental Setup 22
a. Servo-Hydraulic Load Frame 23
b. Custom-Built Compression Grips 24
c. Custom-Built Thermal Control System 25
d. Electromagnet 31
e. Experimental Details 32

IV Ni_2MnGa RESULTS AND DISCUSSION 34

4.1 Testing Procedure 34
a. Differential Scanning Calorimetry (DSC) 34
b. Superconducting Quantum Interference Device (SQUID) 34
c. Thermal Cycling 35
d. Pseudoelasticity 35
4.2 DSC Results 36
4.3 SQUID Results 37
4.4 Thermal Cycling Results 38
4.5 Pseudoelasticity Results 43

CHAPTER Page

4.6 Stress-Temperature Phase Diagram 46

V NiMnCoIn RESULTS AND DISCUSSION 49

5.1 Theoretical Predictions 49
5.2 Testing Procedure 49
a. Differential Scanning Calorimetry (DSC) 50
b. Superconducting Quantum Interference Device (SQUID) 51
c. Thermal Cycling 51
d. Pseudoelasticity 51
e. Optical Microscopy 52
5.3 DSC Results 52
a. NiMnCoIn Batch 1 52
b. NiMnCoIn Batch 2 53
5.4 SQUID Results 54
a. NiMnCoIn Batch 1 54
b. NiMnCoIn Batch 2 58
5.5 Thermal Cycling Results 60
a. NiMnCoIn_[100](110) Batch 1 60
b. NiMnCoIn_[087] Batch 1 63
c. NiMnCoIn_[25 7 15] Batch 1 63
d. NiMnCoIn_[100](110) Batch 2 64
5.6 Pseudoelasticity Results 66
a. NiMnCoIn_[25 7 15] Batch 1 66
b. NiMnCoIn_[100](110) Batch 2 67
5.7 Clausius-Clapeyron Relationship 68
5.8 Transformation Strain 69
5.9 Entropy of Transformation 71
5.10 Thermal and Stress Hysteresis 72
5.11 Magnetostress in NiMnCoIn 74
5.12 Optical Microscopy Results 76

VI CONCLUSIONS AND FUTURE RECOMMENDATIONS 81

6.1 Conclusions 81
6.2 Future Recommendations 83

REFERENCES 84

VITA 87

LIST OF FIGURES

Page

Figure 1.1 Electric resistance vs. temperature curves representative of thermoelastic (small thermal hysteresis) and nonthermoelastic (large thermal hysteresis) shape memory alloys [2] 3

Figure 1.2 A schematic detailing the typical stress-strain behavior of shape memory alloys [5] 5

Figure 1.3 A schematic illustrating the magnetic shape memory effect process via magnetic field induced martensite variant reorientation [7] 7

Figure 1.4 Schematic representation of free energy curves for parent and martensite phases, and their relation to transformation temperatures [2] 10

Figure 2.1 Temperature and field dependence of the critical stress levels and stress hysteresis during the first stage transformation. Solid lines demonstrate the response under zero magnetic field, while the dotted lines show the response under 1.6T [29]. 16

Figure 3.1 Magneto-Thermo-Mechanical (MTM) test setup used in this study.... 22

Figure 3.2 MTS 810 servo-hydraulic load frame and load cells used in this study 23

Figure 3.3 Custom compression grips with inserts. 24

Figure 3.4 Custom compression grips installed using hydraulic collet grips. 25

Figure 3.5 The complete custom-made thermal management system. 26

Figure 3.6 Custom lexan box with recess holes for electromagnet pole pieces and compression grips. 27

Figure 3.7 Cu coil windings used to channel liquid nitrogen. 28

Figure 3.8 Watlow thin-band mica heater used to heat compression grips 28

Figure 3.9 ACME step-up transformer used to increase the voltage supplied to heaters. 29

Page

Figure 3.10 Temperature controller used to control thermal management system . 30

Figure 3.11 Lake Shore Model EM4-CS electromagnet 31

Figure 3.12 LakeShore 450 Gaussmeter and cryogenic transverse Hall Probe used to control electromagnet 32

Figure 4.1 DSC results, showing heat flow vs. temperature, for Ni_2MnGa single crystal sample. 36

Figure 4.2 Magnetization as a function of temperature under magnetic field of 200 Gauss, as well as the derivative of the response detailing the transformation temperatures for the parent to I-phase to 10M martensite transformation sequence 37

Figure 4.3 Low-stress thermal cycling results showing the increase in transformation temperatures with increasing stress levels. 39

Figure 4.4 Low-stress thermal cycling results detailing the X-phase transformation. 40

Figure 4.5 Thermal cycling response under a compressive load of 20 MPa illustrating the parent phase to X-phase to I-phase to 10M martensite transformation sequence in detail. 41

Figure 4.6 The phase transformation from austenite to X-phase to 10M martensite at stress levels greater than 25 MPa. 42

Figure 4.7 Low temperature pseudoelastic response for Ni_2MnGa showing two-stage phase transformations: I-phase to X-phase and X-phase to 10M martensite. 44

Figure 4.8 Stress-strain behavior of Ni_2MnGa detailing the first stage, I-phase to X-phase, transformation. The first stage exhibits a decrease in critical stress as temperature increases. 45

Figure 4.9 High temperature stress-strain behavior of Ni_2MnGa showing the parent to 10M martensite phase transformation. 46

Figure 4.10 Stress-temperature diagram for Ni_2MnGa illustrating the multiple phase transformations. 47

Page

Figure 5.1	DSC results showing heat flow as a function of temperature for NiMnCoIn batch 1 specimen. Martensite start temperature is shown to be about -26°C.	53
Figure 5.2	DSC results showing heat flow as a function of temperature for the NiMnCoIn batch 2 specimen. Martensitic transformation is expected below -60°C	54
Figure 5.3	Magnetization of NiMnCoIn batch 1 sample as a function of externally applied magnetic field demonstrating fully reversible MFIPT.	55
Figure 5.4	Magnetization of NiMnCoIn batch 1 sample as a function of temperature at different magnetic fields	56
Figure 5.5	Magnetization as a function of temperature under 500 Oe externally applied magnetic field for NiMnCoIn batch 1. The dM/dT curve identifies the transformation temperatures	57
Figure 5.6	Temperature as a function of externally applied magnetic field for NiMnCoIn batch 1, as derived from the magnetization data obtained from SQUID measurements	58
Figure 5.7	Magnetization as a function of temperature for different magnetic fields for NiMnCoIn batch 2, as obtained from SQUID measurements.	59
Figure 5.8	Magnetization as a function of temperature under 500 Oe externally applied magnetic field for NiMnCoIn batch 2.	60
Figure 5.9	Thermal cycling results for NiMnCoIn_[100](011) batch 1 single crystal at different stress levels	61
Figure 5.10	Thermal cycling results for NiMnCoIn_[087] batch 1 single crystals under various stress levels.	62
Figure 5.11	Thermal cycling results for NiMnCoIn_[25 7 15] batch 1 single crystal under a compressive stress of 50 MPa.	63
Figure 5.12	Thermal cycling results for NiMnCoIn_[100](011) batch 2 single crystal under different stress levels.	65

Page

Figure 5.13 Pseudoelastic response for the NiMnCoIn_[25 7 15] batch 1 single crystal at different temperatures. 66

Figure 5.14 Pseudoelastic response for the NiMnCoIn_[100](011) batch 2 single crystal at different temperatures. 67

Figure 5.15 NiMnCoIn stress-temperature phase diagram illustrating the Clausius-Clapeyron relationship for the different crystallographic orientations of both batches 1 and 2. 68

Figure 5.16 Transformation strain, for different crystallographic orientations and batches, as a function of applied compressive stress in NiMnCoIn single crystals. 70

Figure 5.17 Transformation strain as a function of temperature for the [100](011) batch 2 specimen as determined from the pseudoelastic responses at 0°C and 20°C. 71

Figure 5.18 Thermal hysteresis, for different crystallographic orientations and batches, as a function of applied compressive stress in NiMnCoIn single crystals 73

Figure 5.19 Stress hysteresis, for the NiMnCoIn_[100](011) batch 2 single crystal as a function of temperature. 74

Figure 5.20 Pseudoelasticity at different magnetic field magnitudes for the NiMnCoIn [100](011) batch 2 single crystal. 75

Figure 5.21 Critical stress for phase transformation under different magnetic fields for NiMnCoIn [100](011) batch 2 sample. The sample exhibits ~20 MPa magnetostress under 1.6T magnetic field. 76

Figure 5.22 Optical microscopy (5x) of the NiMnCoIn [100](011) batch 1 single crystal, showing that several precipitates exist in the matrix. 77

Figure 5.23 Optical microscopy (5x) of the NiMnCoIn [100](011) batch 2 single crystal, showing that several precipitates exist in the matrix. 77

Figure 5.24 Close-up view (20x) of second phase in the NiMnCoIn [100](011) batch 2 single crystal. 78

Page

Figure 5.25 Optical microscopy (5x) of the NiMnCoIn [25 7 15] batch 1 single crystal, showing a clean surface without the presence of precipitates. 79

Figure 5.26 Optical microscopy (5x) of the NiMnCoIn [087] batch 1 single crystal, showing a fractured surface without the presence of precipitates. 79

LIST OF TABLES

Page

Table 5.1 Summary of theoretical transformation strains for different crystallographic orientations in the NiMnCoIn single crystal system. 49

Table 5.2 Summary of Clausius-Clapeyron slopes, theoretical transformation strains, and estimations of transformation entropy for each crystallographic orientation and batch 72

CHAPTER I
INTRODUCTION

The basic objectives of this study are twofold: to establish the stress-temperature phase diagram detailing the multiple phase transformations in Ni_2MnGa magnetic shape memory alloy (MSMA) single crystals, and to characterize the shape memory response of NiMnCoIn MSMA single crystals. First, a short introduction to the basic concepts in MSMAs and the work previously performed on Ni_2MnGa and NiMnCoIn will be presented. Next, the primary motivations for this work will be outlined, followed by brief descriptions of the experimental techniques utilized during this study. Lastly, the results will be presented in detail with accompanying discussion followed by conclusions and recommendations for future work.

1.1 Background

Shape memory alloys (SMAs) have unique properties, such as high recoverable strains as a result of reversible, diffusionless martensitic transformation (MT). Solid to solid phase transformations may be initiated in many different ways including temperature change, externally applied stress, or upon application of magnetic field. The martensitic phase transformation occurs when a high temperature phase, known as austenite or parent phase, transforms to a low temperature phase with a lower symmetry called martensite, and vice versa.

MT may be defined simply as lattice deformation involving shear deformation and is a result of cooperative atomic movement. There is a one-to-one correspondence called “lattice correspondence” between the lattice points of the parent and martensite phases. The habit plane is a specific plane between the parent and martensite phases, along which the shear occurs during transformation, and since the habit plane is strain and rotation free throughout the entire transformation, this type of deformation is termed invariant shear strain. Martensites with different habit planes that are from the same family of planes are called variants [1].

This thesis follows the style and format of Acta Materialia.

MT is a first order transformation which results in large transformation strain. In order to reduce the strain during nucleation and growth, one of two types of lattice invariant shear (LIS) mechanisms may potentially take place: twinning or dislocation slip [2]. These are called LIS mechanisms because they do not change the structure or habit plane of the martensite. In most cases, twinning is the controlling LIS mechanism for most SMAs.

The driving force for diffusionless phase transformation in SMAs is the difference in the chemical free energies between the phases. When the difference in chemical free energies is enough to overcome the energy required to nucleate the other phase, transformation will commence and continue to propagate as the energy for growth is supplied by further increase in the chemical energy difference. The transformation start and finish temperatures from austenite to martensite are called M_s and M_f, respectively, while the transformation start and finish temperatures from martensite to austenite are called A_s and A_f, respectively, where the former transformation is called a forward transformation and the latter one a reverse transformation.

When the MT starts during cooling, a second step of strain minimization takes place in addition to LIS in order to minimize the transformation strain, which is self accommodation of the martensite variants. Martensite variants form side by side and they mutually reduce the transformation strain accompanying their formation. This effect is known as self accommodation and the specimen as a whole will not experience any external shape change.

MTs can be classified into two categories: thermoelastic and nonthermoelastic. For thermoelastic MT, the transformation temperature hysteresis is small, the interface between parent and martensite is mobile, and the transformation is crystallographically reversible. For nonthermoelastic MTs, the transformation temperature hysteresis is large, the interface between the martensite and the parent phase is immobile, and once the martensite grows beyond some critical size, the reverse transformation takes place by renucleation of the parent phase. Figure 1.1 shows the difference in transformation temperature hysteresis between the thermoelastic and nonthermoelastic MTs. Most of

the thermoelastic shape memory alloys are intermetallic alloys since they have an ordered structure, which means that lattice sites are occupied by a particular species of atoms. Since MT is a diffusionless process, the product martensite is also ordered and the process is crystallographically reversible. Ordering also promotes higher flow in stress in the parent phase, which prevents damage of the martensite/parent interface during growth of martensite.

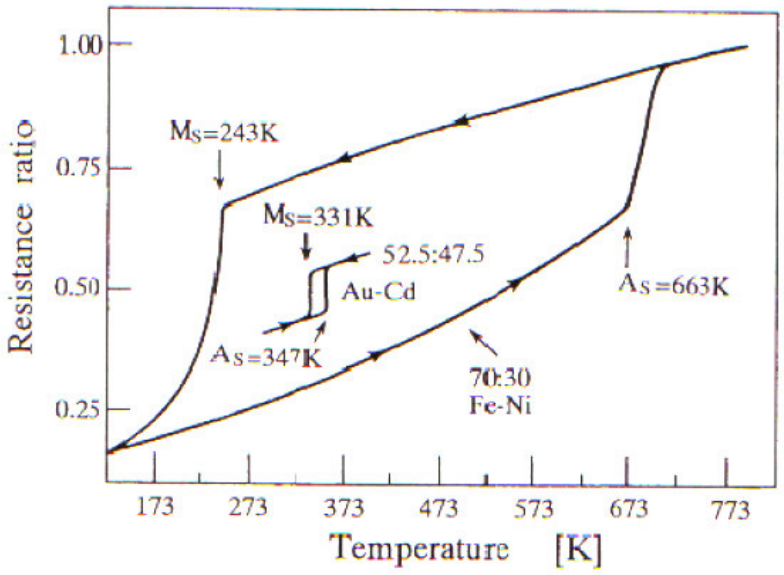

Figure 1.1 Electric resistance vs. temperature curves representative of thermoelastic (small thermal hysteresis) and nonthermoelastic (large thermal hysteresis) shape memory alloys [2].

There are two types of deformation in SMAs, which lead to high recoverable strains: reorientation of martensite and stress induced martensite. When SMAs are cooled under zero stress, the parent phase transforms to martensite and internally twinned martensite variants form self accommodating structures to minimize the macroscopic volume change [1]. The applied stress biases the self accommodating structure and favors the growth of selected martensite variants at the expense of others. When this bias structure is heated above the A_f temperature, it transforms back to its

original shape. This process is called shape memory effect (SME), and results in no net transformation strain with the following forward transformation under zero applied stress. If the self accommodated structure is permanently biased (generally forming dislocations or internal stresses), large macroscopic strain will be experienced under zero applied stress with forward and reverse transformations. This process is called two-way shape memory effect (TWSME) [3, 4].

It is well known that deformation of austenite in the range of A_f to a certain temperature, M_d, results in the stress induced martensitic transformation (SIM). Favored martensite variants are formed during the loading of the parent phase, likewise these martensite variants transform back to the parent phase upon unloading since they are not chemically stable at that temperature. This deformation behavior is known as pseudoelasticity or superelasticity. Pseudoelasticity is a more generic term than superelasticity as it encompasses rubber-like behavior, which is observed in some SMAs when martensite twins are bent and aged to recover its original shape. Pseudoelasticity can be used for both martensite and austenite phases, whereas superelasticity is used only for the parent phase. As the temperature increases, the stress required for inducing martensite also increases exceeding the stress necessary for dislocation slip, which deteriorates the pseudoelastic response. Deformations at temperatures higher than M_d do not lead to SIM because dislocation slip is the only deformation mechanism. In other words, M_d is the highest temperature at which pseudoelasticity is observed.

Figure 1.2 shows a typical stress-strain response of a shape memory alloy. There are three possible deformation cases present. Case I: If the material is initially in the austenitic state, then in Stage I, austenite is elastically deformed; in Stage II, stress induced martensite develops; and in Stage III, slip deformation of martensite occurs. Case II: If the material is initially in the martensite state, then in Stage I, martensite is elastically deformed; in Stage II, detwinning of martensite occurs with the favored variants growing at the expense of others; and in Stage III, slip deformation of martensite occurs. Case III: If the initial material is a mixture of austenite and martensite phases, some combination of the previous deformation types will occur.

Upon unloading, the martensite structure will unload elastically (in all cases), followed by pseudoelastic strain (reverse transformation from martensite to austenite) in Cases I and III. Further strain can be recovered if the deformed samples are heated above the A_f temperature. The remaining permanent strain is inelastic and is a result of dislocations formed during loading. The recoverable strain decreases with increased plastic deformation due to the fact that slip formation inhibits reverse transformation due to the relaxation of stored elastic energy [6].

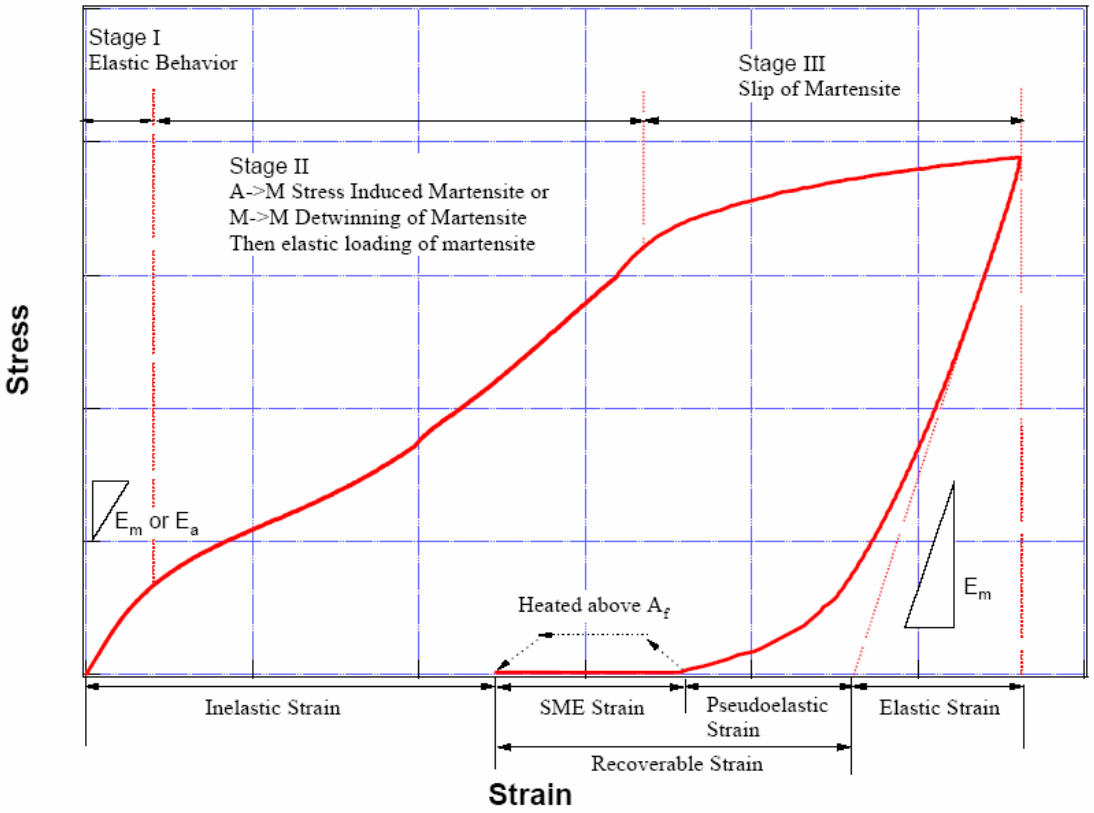

Figure 1.2 A schematic detailing the typical stress-strain behavior of shape memory alloys [5].

1.2 Magnetic Shape Memory Effect

As stated earlier, some shape memory alloys may exhibit an external change in shape as a response to an externally applied magnetic field. This type of behavior is known as magnetic field induced strain (MFIS) and materials exhibiting this unique behavior are known as MSMAs. Under the application of external magnetic fields, MSMAs demonstrate large inelastic strains in the martensite state. This phenomenon is known as magnetic shape memory effect (MSME). Typically, there are two mechanisms that induce MFIS in these alloys: martensite variant reorientation and magnetic field induced phase transformation (MFIPT).

Upon cooling, the parent phase transforms into a lower symmetry martensite state, and the low-temperature martensite contains multiple variants, each magnetized along a preferred crystallographic orientation, termed the magnetic easy axis. The magnetization of the variant can be oriented in either the positive or negative easy axis direction. With this notion of preferred magnetization directions, it is apparent that a certain martensite variant will be energetically favored over others upon the application of an external magnetic field. If the direction of magnetization in the martensite variant is parallel to the direction of applied magnetic field, the energy required for motion of the martensite twin interface is very small. On the other hand, if the direction of magnetization in the martensite variant is perpendicular to the direction of applied magnetic field, the energy required for martensite twin interface motion is very large. Therefore, the martensite variant whose direction of magnetization is parallel (or near parallel) to the direction of the externally applied magnetic field will be energetically favored and the volume fraction of that variant will increase at the expense of the others. In other words, the application of an external magnetic field initiates the motion of twin interfaces such that martensite twins with favorably oriented easy axis of magnetization grow at the expense of the other martensite twins leading to an external shape change. This concept is known as magnetic field induced reorientation of martensite variants. In order to observe reversible martensite variant reorientation, the simultaneous application of an external magnetic field and stress is required. Likewise, the magnetic field

induced reorientation of martensite variants is only possible in materials with a low energy requirement for twin boundary motion and high magnetocrystalline anisotropy energy (MAE). MAE will be discussed in more detail in the following section.

A schematic representing the process of martensite variant reorientation by magnetic field is shown in Figure 1.3. Initially, the undeformed austenite phase is oriented with the [100] crystallographic axis along the x-direction and the [010] crystallographic axis along the y-direction.

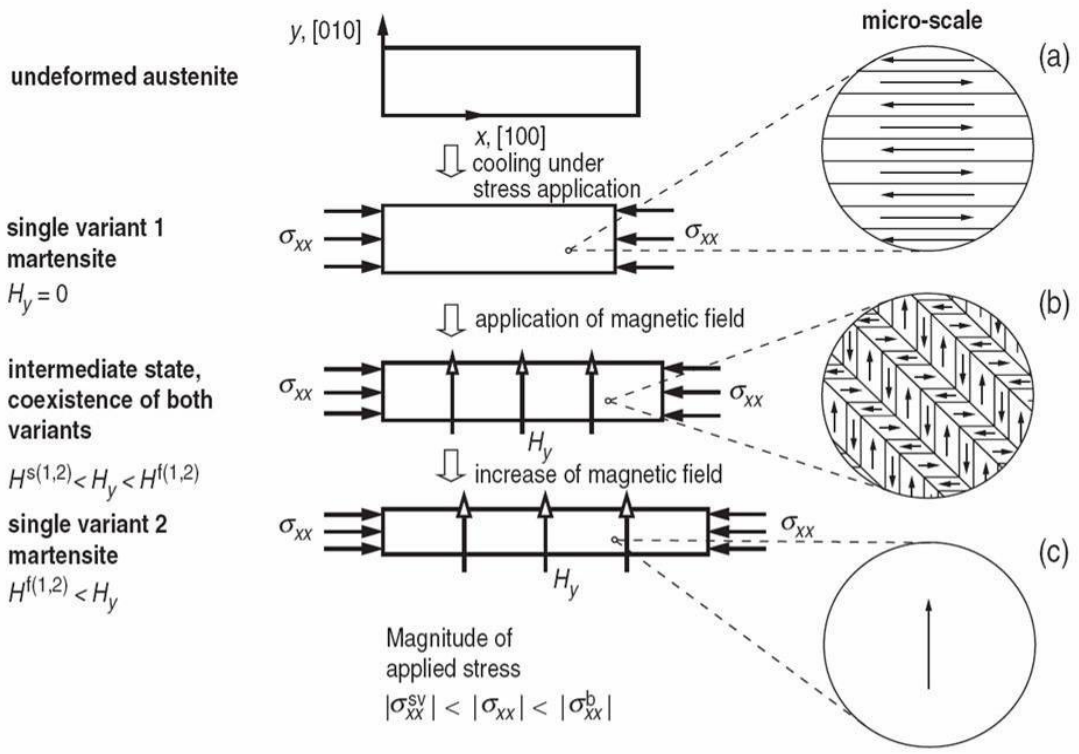

Figure 1.3 A schematic illustrating the magnetic shape memory effect process via magnetic field induced martensite variant reorientation [7].

While cooling under an applied compressive stress the material transforms from the austenite parent phase to a single variant martensite state (variant 1) with individual magnetic domains as shown in inset (a). The applied compressive stress yields a single variant arrangement of detwinned martensite. The application of a transverse magnetic

field, H_y, that is great enough to overcome magnetic domain wall motion, induces the nucleation of variant 2 martensite. The volume fraction of variant 2 martensite then increases with increasing H_y. As can be seen in inset (b), the volume fraction of variant 2 increases at the expense of variant 1 as the magnitude of the applied magnetic field is increased. The growth of variant 2 martensite results in axial reorientation strain. Upon reaching saturation magnetization, variant 1 is completely eradicated, leaving only variant 2 martensite, and maximum reorientation strain is obtained.

The primary limitation associated with magnetic field induced variant reorientation is low actuation levels. The maximum actuation stress, known as blocking stress, is the stress level above which magnetic field induced microstructural changes (except magnetorestriction) and MFIS are not possible. The blocking stress in field induced variant reorientation is the difference in the magnetostress (i.e. energy acquired upon application of magnetic field) and the detwinning.

$$\sigma_{blocking} = \sigma_{magnetostress} - \sigma_{dtwng} \tag{1}$$

As shown by equation 1, the externally applied stress opposes the magnetostress. Therefore, once the energy supplied by the externally applied stress exceeds that gained from the application of the magnetic field (i.e. MAE), then the effect of the magnetostress is suppressed and magnetic field induced variant reorientation is no longer possible.

For MFIPT, the energy contributed upon the application of the external magnetic field must be great enough to move the phase front from austenite to martensite, resulting in phase transformation. Upon the application of an external magnetic field, two magnetic energy contributions are made: the Zeeman energy and MAE. The Zeeman energy, which will be discussed more in the following section, is a function of magnetic field magnitude and difference in saturation magnetizations of both the parent and martensite phases. In most MSMAs, the saturation magnetizations of the parent and martensite phases are similar therefore the contribution from the Zeeman energy is

negligible. Thus, the remaining magnetic driving force is the MAE, which is typically too small to induce phase front motion.

The blocking stress for MFIPT slightly differs than that for variant reorientation. In MFIPT, the blocking stress is the difference between the stress required for phase transformation and the magnetostress.

$$\sigma_{blocking} = \sigma_{PT} - \sigma_{magnetostress} \tag{2}$$

Equation 2 illustrates that the externally applied stress assists the magnetostress, whereas in variant reorientation, the two counteract each other. The reason for this is due to the additional magnetic driving force supplied by the Zeeman energy, which provides the additional energy to overcome the chemical energy differences between the two phases, similar to mechanical work. Therefore, for MFIPT, the maximum actuation stress is solely dependent upon the available magnetic field rather than the MAE.

Thus, magnetic field induced variant reorientation begins with the martensite phase and, upon application of an external magnetic field, MFIS is realized via twin boundary motion. Whereas for MFIPT, the transformation from parent phase to martensite phase is induced by the application of an external magnetic field via phase front movement. Typically, the MAE is not sufficient to achieve phase front motion; however with the additional driving force from the Zeeman energy MFIPT becomes possible.

1.3 Thermodynamic Framework for Martensitic Transformation

Since martensitic transformations are not associated with a compositional change, the free energy curves for both parent and martensite phases as functions of temperature can be plotted as shown in Figure 1.4.

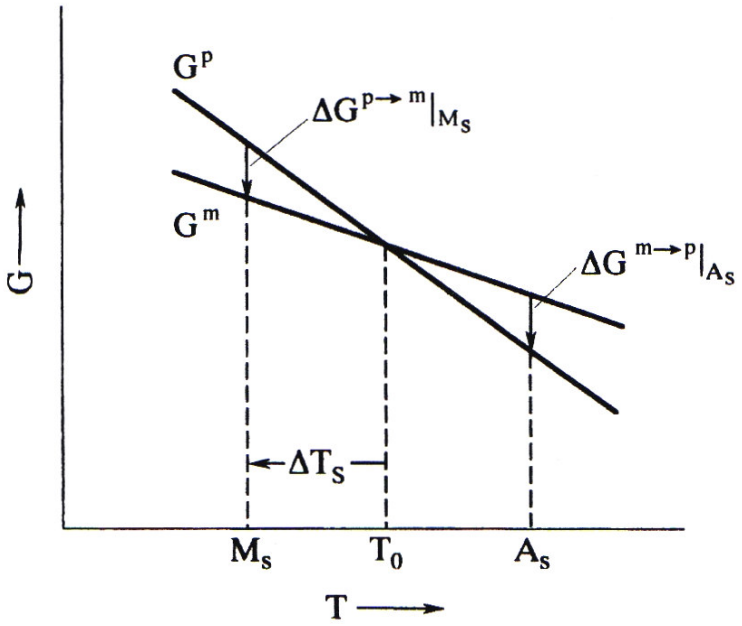

Figure 1.4 Schematic representation of free energy curves for parent and martensite phases, and their relation to transformation temperatures [2].

Here, T_o represents the equilibrium temperature between the parent and martensite phases, and $\Delta G^{P\rightarrow M}\Big|_{M_s} = G^M - G^P$ represents the driving force for the nucleation of martensite. G^M and G^P represent the Gibbs free energy of martensite and parent phases, respectively. The equilibrium temperature may be approximated by using equation 3.

$$T_o = \frac{1}{2}\left(M_s + A_s\right) \tag{3}$$

The difference in Gibbs free energy between the parent and martensite phases during a thermoelastic martensitic transformation is defined by equation 4 [2].

$$\Delta G_{total}^{P\rightarrow M}(T,\sigma) = \Delta G_{ch}^{P\rightarrow M} - \Delta E_{mech}^{P\rightarrow M} + \Delta G_{el}^{P\rightarrow M} + \Delta E_{irr} \tag{4}$$

The $\Delta G_{total}^{P\to M}(T,\sigma)$ term represents the total difference in Gibbs free energy, which should be less than zero in order to trigger the phase transformation. ΔG_{ch} is the chemical free energy difference between martensite and parent phases, ΔE_{mech} is the mechanical energy provided by the externally applied load during the phase transformation, ΔG_{el} is the stored elastic energy, and ΔE_{irr} is the dissipation energy due to defect and dislocation generation and frictional energy spent on the movement of phase fronts. ΔG_{el} and ΔE_{irr} are also known as non-chemical energy terms (ΔG_{nonch}). The chemical free energy difference can be expressed as;

$$\Delta G_{\mathrm{ch}}^{\mathrm{P}\to\mathrm{M}}(T) = \Delta H - T\cdot\Delta S = G_{\mathrm{ch}}^{\mathrm{M}} - G_{\mathrm{ch}}^{\mathrm{P}} \tag{5}$$

In equation 5, ΔH and ΔS represent the change in enthalpy and entropy, respectively, upon transformation, while G_{ch}^{M} and G_{ch}^{P} are the chemical free energies of the martensite and parent phases, respectively.

In the presence of an externally applied magnetic field, equation 4 may be modified and rewritten as equation 6.

$$\begin{aligned}\Delta G_{total}^{P\to M}(T,H_y) = \Delta G_{ch}^{P\to M} - \Delta E_{mech}^{P\to M} + \Delta G_{el}^{P\to M} \\ + \Delta E_{irr} - \Delta G_{mag}^{P\to M} + \Delta G_{MAE}^{P\to M}\end{aligned} \tag{6}$$

In the above equation, ΔG_{mag} is the magnetic driving force due to the difference between the saturation magnetizations of the martensite and parent phases (i.e. Zeeman Energy difference) and is defined by equation 7 [8].

$$\Delta G_{mag}^{P\to M} = H_y(M^{s}_{martensite} - M^{s}_{parent}) \tag{7}$$

Here, H_y represents the magnitude of the externally applied magnetic field and M^s is the saturation magnetization. The $\Delta G_{mag}^{P\to M}$ term has a negative sign in equation 5 because the available Zeeman energy difference provides the additional energy to overcome the chemical energy difference between transforming phases similar to external mechanical work. This term is more noticeable when the transformation occurs between a ferromagnetic parent phase and a paramagnetic martensite phase (or vice versa). $\Delta G_{MAE}^{P\to M}$ is the difference between the MAEs of the martensite and parent phases, and can be expressed by equation 8.

$$\Delta G_{MAE}^{P\to M} = \left(K_u \sin\theta\right)_{martensite} - \left(K_u \sin\theta\right)_{parent} \tag{8}$$

K_u represents MAE and θ is the angle between the applied magnetic field direction and easy axis of magnetization of the corresponding phase. The $\Delta G_{MAE}^{P\to M}$ term has a positive sign in equation 6 since it represents another energy storage contribution to total free energy similar to $\Delta G_{el}^{P\to M}$. Magnetoelastic effects may also be taken into account in the $\Delta G_{el}^{P\to M}$ term in equation 6, however, they are usually negligible as compared to $\Delta G_{mag}^{P\to M}$ and $\Delta G_{MAE}^{P\to M}$ [9, 10].

The two separate magnetic energies may either augment or cancel each other, depending upon the saturation magnetization and MAE differences of the two phases, which may be manipulated with compositional modifications and/or temperature. If $-\Delta G_{mag}^{P\to M} + \Delta G_{MAE}^{P\to M}$ is positive, then the parent phase is more stable in the presence of a magnetic field. In other words, the application of magnetic field can be used to trigger martensite to parent phase transformation. If it is negative, then martensite is more stable under magnetic field and parent to martensite phase transformation may be activated with applied magnetic field. It is also possible to maximize or minimize $\Delta G_{MAE}^{P\to M}$ by simultaneously applying stress and magnetic field, however, this requires the selection of favorable field and axial stress directions such that the stress would reorient

the magnetic easy axis of the martensite perpendicular or parallel to the applied field direction upon phase transformation. For example, simultaneous application of the field and compressive stress perpendicular to each other in Ni_2MnGa MSMAs would maximize $(K_u \sin\theta)_{martensite}$ because the stress would bias the martensite twin variant upon phase transformation with $\theta = 90^o$ [11]. In summary, $\Delta G_{mag}^{P\to M}$ is primarily composition and temperature dependent, while $\Delta G_{MAE}^{P\to M}$ depends also upon the crystallographic direction of the applied stress and magnetic field.

1.4 Clausius-Clapeyron Relationship

One of the most common methods used to analyze the effect of stress on martensitic transformation is the use of Clausius-Clapeyron equation, which is defined as [1];

$$\frac{d\sigma}{dT} = -\frac{\Delta S^{P\to M}}{\varepsilon_{tr}^{P\to M}} = -\frac{\Delta H^{*P\to M}}{T_o \varepsilon_{tr}^{P\to M}} \tag{9}$$

In equation 9, σ represents the externally applied uniaxial stress, T_o is the equilibrium temperature, $\varepsilon_{tr}^{P\to M}$ is the theoretical transformation strain, $\Delta S^{P\to M}$ is the change in entropy, and $\Delta H^{*P\to M}$ is the change in enthalpy during the transformation. Recall from Figure 1.4, the M_s temperature is defined to be the temperature at which the difference in chemical energies between the parent and martensite phases is large enough to induce phase transformation. As temperature is increased from M_s, the available chemical energy linearly decreases, which means that an additional driving force, such as external stress, must be supplied in order to induce phase transformation. Since the energy required for phase transformation is constant and the available chemical energy linearly decreases, the additional driving force (i.e. external stress) required for phase transformation as a function of the difference between the M_s and test temperatures is known as the Clausius-Clapeyron relationship. Therefore, the Clausius-Clapeyron

relationship describes how the M_s temperature changes as a function of externally applied uniaxial stress.

1.5 Brief History of Ni_2MnGa and NiMnCoIn

MSMAs have recently received a significant amount of attention due to their ability to generate one order of magnitude higher MFIS than traditional magnetorestrictive materials, as well as their inimitable actuation, sensing, and power generation capabilities [11-19]. The development of the NiMnGa ferromagnetic shape memory alloy (FSMA) system began nearly two decades ago, and since then NiMnGa alloys have become some of the most widely examined MSMAs to date [14-16]. NiMnGa alloys are capable of producing approximately 6% MFIS in 10M martensite [20] and about 10% MFIS in 14M martensite [12], where 10M refers to the five layered tetragonal structure and 14M corresponds to the seven layered orthorhombic structure [9]. In addition, NiMnGa alloys have been known to exhibit multiple phase transformations depending upon composition, single crystal orientation, and temperature [21-26]. Reliant upon the aforementioned factors, NiMnGa alloys may experience the complete or part of the following four stage transformation process: $L2_1$ parent to intermediate (I-phase) to 10M tetragonal (or X-phase: a new phase with an unknown crystal structure which is observed only under stress) to 14M orthorhombic (or monoclinic) to nonmodulated (2M) tetragonal martensitic transformations [21, 27-29]. Despite several studies on the structural and magnetic properties of the various NiMnGa martensite phases [30-38], very few studies have focused on the effects of magnetic field on the intermartensitic phase transformations [28, 29, 39]. By examining the effects of magnetic field on the intermartensitic phase transformations (I-phase in particular), it has been found that Ni_2MnGa MSMA is capable of exhibiting both one-way [28] and reversible [29] stress-assisted MFIS. The requirements for obtaining this behavior and the thermodynamic framework (including magnetic energies) describing this magnetic field induced phase transformation have recently been identified [28, 29].

Within the past two years a new class of FSMAs has emerged with great potential. This new class of materials, known as meta-magnetic shape memory alloys (MMSMAs), includes NiMnIn, NiMnSn, NiMnSb, NiMnCoIn, and NiMnCoSn [40-49]. Magnetization tests have revealed that these materials exhibit unique magnetic properties for both the parent and martensite phases [40-46], such as ferromagnetic parent and paramagnetic (or non-magnetic) martensite phases. Similar to NiMnGa MSMAs, these new materials have been shown to exhibit MFIS [44, 47] and magnetic field induced shape recovery [43-46]. In efforts to better understand these MMSMAs, few recent studies have been conducted in order to determine the structural and magnetic properties of both the parent and martensite phases [41, 42, 45, 46, 48, 49]. Despite several tests on this new class of SMAs, very few of the experiments conducted have been focused on NiMnCoIn [44, 49]. The work conducted on NiMnCoIn has been concentrated on the magnetic domain structure of the parent and martensite phases during transformation [49] and the materials candidacy as a MSMA [44]. However, there have not yet been any experiments to reveal the traditional shape memory response of this new alloy.

CHAPTER II

MOTIVATION AND OBJECTIVES

As previously stated, Ni_2MnGa has been shown to exhibit one-way [28] and fully reversible [29] stress-assisted magnetic field induced phase transformation. The capacity of this alloy to demonstrate such behavior depends upon its ability to meet certain mechanical and magnetic property requirements [29]. In order to achieve fully reversible field induced phase transformation, the pseudoelastic stress-strain response, hysteresis loops in particular, both with and without the application of magnetic field must be separated. In other words, the increase in critical stress for phase transformation due to the application of magnetic field (i.e. magnetostress) must be greater than the stress hysteresis.

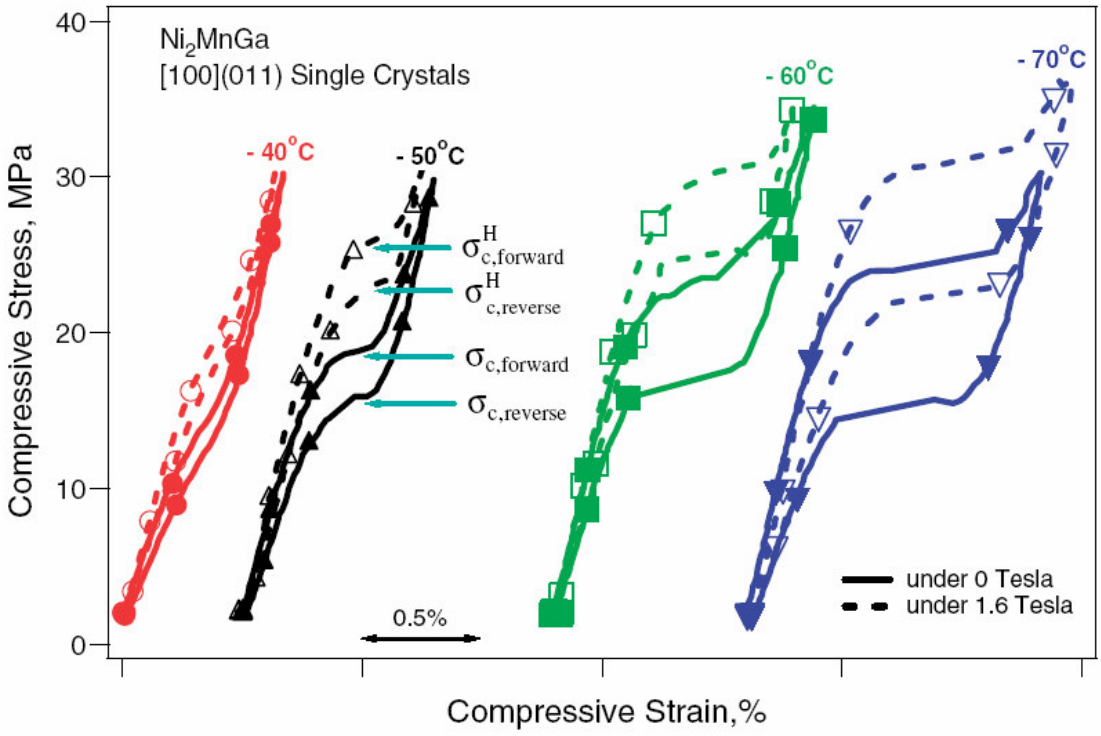

Figure 2.1 Temperature and field dependence of the critical stress levels and stress hysteresis during the first stage transformation. Solid lines demonstrate the response under zero magnetic field, while the dotted lines show the response under 1.6T [29].

Therefore, the alloy must demonstrate large magnetostress and small stress hysteresis for the field induced phase transformation to occur. Recently, Ni_2MnGa has been shown to demonstrate this behavior in the I-phase to X-phase transformation [28, 29], which may be seen in Figure 2.1.

In addition to discovering the ability of Ni_2MnGa to demonstrate fully reversible stress-assisted magnetic field induced phase transformation, the existence of a previously unidentified martensite phase (X-phase) was revealed [27-29]. It has been determined that the X-phase exists between the intermediate and 10M martensite phases and is mechanically induced under low stress levels [27-29]. Due to the recent discovery of the X-phase, very little is known about its crystal structure, magnetic properties, shape memory characteristics, or the effects of magnetic field on phase transformation.

Even though Ni_2MnGa is one of the most studied MSMAs, recent discoveries have shown that several unanswered questions still exist. The discovery of reversible field induced phase transformation in the I-phase and the existence of a mechanically induced martensite phase (X-phase) demonstrate that further investigation into the magnetic shape memory response in Ni_2MnGa is required. For this reason, the establishment of a stress-temperature phase diagram of the Ni_2MnGa system would prove beneficial in future experimentation. This phase diagram will provide insight into the transformation behavior of Ni_2MnGa, as well as define the stress and temperature ranges where the X-phase exists and where reversible field induced phase transformation may be observed.

NiMnCoIn is a new MMSMA and has great potential as a functional material due to its innate ability to exhibit MFIPT with much lower field requirements (~4T) than currently available MSMAs such as FeNiCoTi. Experiments recently conducted on this alloy have revealed phase transformation from a ferromagnetic parent phase to a paramagnetic martensite phase. This feature is unique because it greatly increases the contribution from the Zeeman energy ultimately providing an additional magnetic driving force, which also increases the possibility of MFIPT. Therefore, the contribution of the magnetic energies as a driving force for phase transformation is not limited by the

MAE. In other words, magnetic field induced phase transformation is possible in NiMnCoIn, despite a slightly elevated field requirement [44]. NiMnCoIn has also shown a separation in thermomagnetization curves under different magnetic field magnitudes [44] demonstrating this alloys ability to exhibit large magnetostress, resulting in a strong candidacy for reversible field induced phase transformation. In order to prove this behavior, field induced shape recovery tests were performed on NiMnCoIn, which resulted in the near full recovery of 3% prestrain [44].

In addition to the exploration of metamagnetic shape memory behavior in NiMnCoIn, an x-ray diffraction study was conducted in order to determine the lattice parameters of both the parent and martensite phases [44]. From the results, it is apparent that NiMnCoIn exhibits lattice distortion that is similar in magnitude to Ni_2MnGa, which is known for demonstrating large transformation strains and large MFIS [44].

The aforementioned study [44] has shown that NiMnCoIn exhibits shape memory effect and pseudoelastic response. However, very little has been done to characterize the complete shape memory response of this new alloy. In order to further examine the potential of this alloy as a functional material it is imperative to first understand the basic shape memory behavior of this material. By examining the thermoelastic behavior under different stress levels and the pseudoelastic response at different temperatures, the stress-strain behavior may be characterized. Despite an elevated field requirement for MFIPT in NiMnCoIn, the stress-strain behavior may be used to reduce the magnetic field requirement by assisting in the phase transformation, similar to that in Ni_2MnGa [28, 29]. However, NiMnCoIn is promising in the fact that, unlike Ni_2MnGa, the available magnetic energy is greater due to the presence of the Zeeman energy. This is advantageous because it will ultimately result in increased blocking stress for MFIPT, which is beneficial for engineering applications.

Thus, the main objectives of the present study are to examine both Ni_2MnGa and NiMnCoIn to determine the following:

1) Perform Differential Scanning Calorimetry (DSC) experiments to determine the transformation temperatures of Ni_2MnGa.

2) Determine the magnetization of both the parent and martensite phases of Ni_2MnGa as well as the transformation temperatures using a Superconducting Quantum Interference Device (SQUID).
3) Perform thermal cycling and pseudoelasticity tests on Ni_2MnGa single crystals to experimentally determine the effect of compressive stress on the transformation temperatures and to determine the stress and temperature ranges where the I-phase and X-phase exist.
4) Using the data obtained from the thermal cycling and pseudoelasticity tests, the Clausius-Clapeyron relationship for each phase will be determined and used to construct the stress-temperature phase diagram.
5) Theoretically determine the maximum obtainable transformation strain for NiMnCoIn single crystals with crystallographic orientations in the [001], [087], and [25 7 15] directions.
6) Perform Differential Scanning Calorimetry (DSC) experiments to determine the transformation temperatures of NiMnCoIn for batches 1 and 2.
7) Determine the magnetization of both the parent and martensite phases of NiMnCoIn as well as the transformation temperatures using a Super Quantum Interference Device (SQUID) for batches 1 and 2.
8) Perform thermal cycling and pseudoelasticity tests on NiMnCoIn single crystals to experimentally determine the effect of compressive stress on the transformation temperatures.
9) Using the data obtained from the thermal cycling and pseudoelasticity tests, the Clausius-Clapeyron relationship for each orientation will be determined.
10) The experimental transformation strain will be deduced from the thermal cycling and pseudoelasticity results and compared to the theoretical calculations.

11) Using the Clausius-Clapeyron relationships in conjunction with the theoretical transformation strains, the entropy of transformation will be estimated.
12) The thermal cycling results will be used to determine the thermal hysteresis of the transformation, which will provide insight into NiMnCoIn's ability to exhibit MFIPT.
13) Lastly, the samples will be carefully inspected using optical microscopy to determine the existence of precipitates and to determine the mode of failure.

CHAPTER III
EXPERIMENTAL TECHNIQUES

3.1 Materials and Sample Preparation

a. Ni_2MnGa

An ingot of Ni_2MnGa with a nominal composition of 50Ni-25Mn-25Ga (in at. %) was prepared using vacuum induction melting. Single crystals were grown using the Bridgman technique in a He atmosphere. The composition of the single crystals was determined to be $Ni_{51.1}Mn_{24.0}Ga_{24.9}$ using inductively coupled plasma-atomic emission spectrometry (ICP-AES). The difference between the nominal and actual compositions is probably due to the evaporation of Mn during single crystal growth [47, 50]. The single crystal samples were cut into rectangular prisms with dimensions measuring approximately 4 mm x 4 mm x 8 mm using electro-discharge machining (EDM) to assure that both magnetic field and stress can be applied along known crystallographic directions. The face normals of the samples were along the [100], [011], and $[01\bar{1}]$ directions in the parent phase ($L2_1$ ordered structure [40]). Compressive stress was applied along the [100] direction. The samples were tested in as-grown condition.

b. NiMnCoIn

An ingot of NiMnCoIn with a nominal composition of 45Ni-36.5Mn-5Co-13.5In (in at. %) was prepared using vacuum induction melting. Two different batches of single crystals were grown using the Bridgman technique in a He atmosphere. The single crystal samples from batch 1 were cut into rectangular prisms with dimensions measuring approximately 4 mm x 4 mm x 8 mm using electro-discharge machining (EDM) with the long axes aligned either along the [100], [087], or [25 7 15] crystallographic directions. The single crystals from batch 2 were cut similar to those from batch 1, however the only samples tested had the long axes aligned along the [100] crystallographic direction. Prior to testing, all samples were sealed in quartz tubing under 10^{-6} mbar vacuum and homogenized at 900°C for 24 hours.

3.2 Experimental Setup

In order to fully characterize these materials, a testing system that has the capability to apply external stress and external magnetic field simultaneously, while also carefully controlling temperature is required. The experimental setup used in this study consists of four main subsystems: a servo-hydraulic load frame, custom-built compression grips, custom-built thermal control system, and an electromagnet. This custom Magneto-Thermo-Mechanical (MTM) test setup can be seen in Figure 3.1, while the details pertaining to the subsystems previously listed are discussed in the subsequent sections.

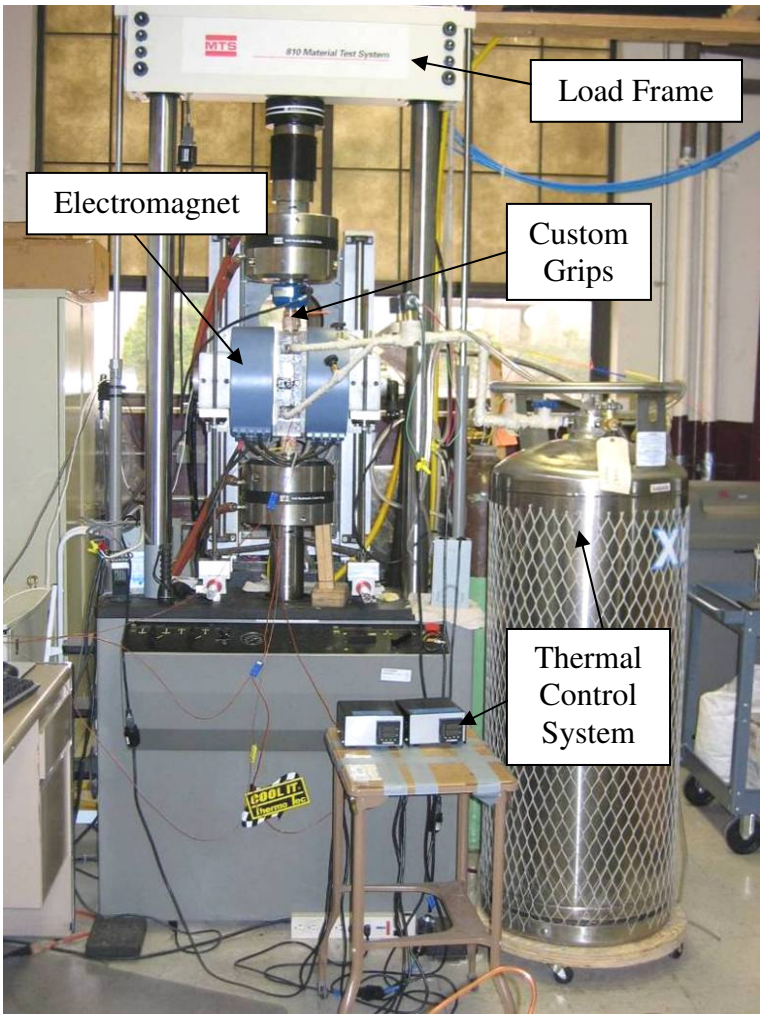

Figure 3.1 Magneto-Thermo-Mechanical (MTM) test setup used in this study.

a. Servo-Hydraulic Load Frame

As the main component in the experimental setup, the servo-hydraulic load frame, an MTS 810 Material Testing System, is capable of producing approximately 250 kN of force. Force is measured using an array of different load cells depending upon the type of experiment to be conducted. For pseudoelasticity tests, where large stresses are required, an MTS load cell rated to 250 kN is used to measure force. Meanwhile, for thermal cycling experiments where low, constant stress levels are needed, a 2500 lbf load cell is used. Crosshead displacement and load data is recorded using the MTS controller and data acquisition systems. The system is retrofit with both upper and lower hydraulic collet grips. The system can be seen in Figure 3.2.

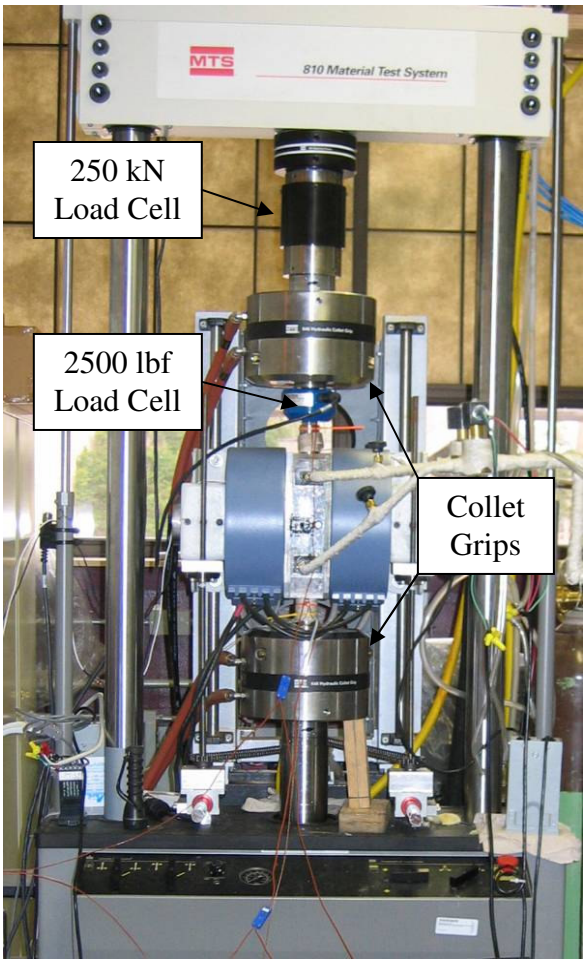

Figure 3.2 MTS 810 servo-hydraulic load frame and load cells used in this study.

b. Custom-Built Compression Grips

For this set of experiments, custom nonmagnetic compression grips and inserts were designed and fabricated out of Ti6Al-4V. The custom grips and inserts can be seen in Figure 3.3. The grip inserts were designed to accommodate a nonmagnetic capacitive displacement sensor (Capacitec, Ayer, MA), which is used to measure the axial strain of the specimen during the experiments. The custom grips were then fit with aluminum collet adapters, and rigidly secured in the hydraulic collet grips, which can be seen in Figure 3.4.

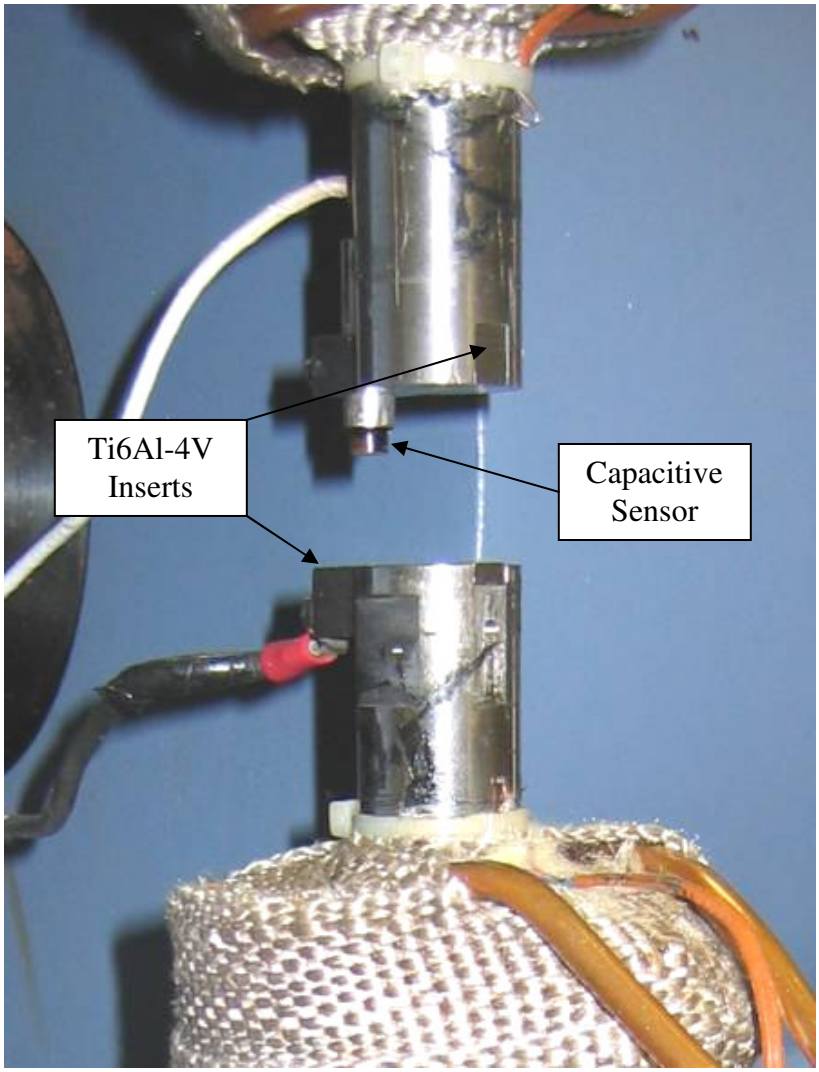

Figure 3.3 Custom compression grips with inserts.

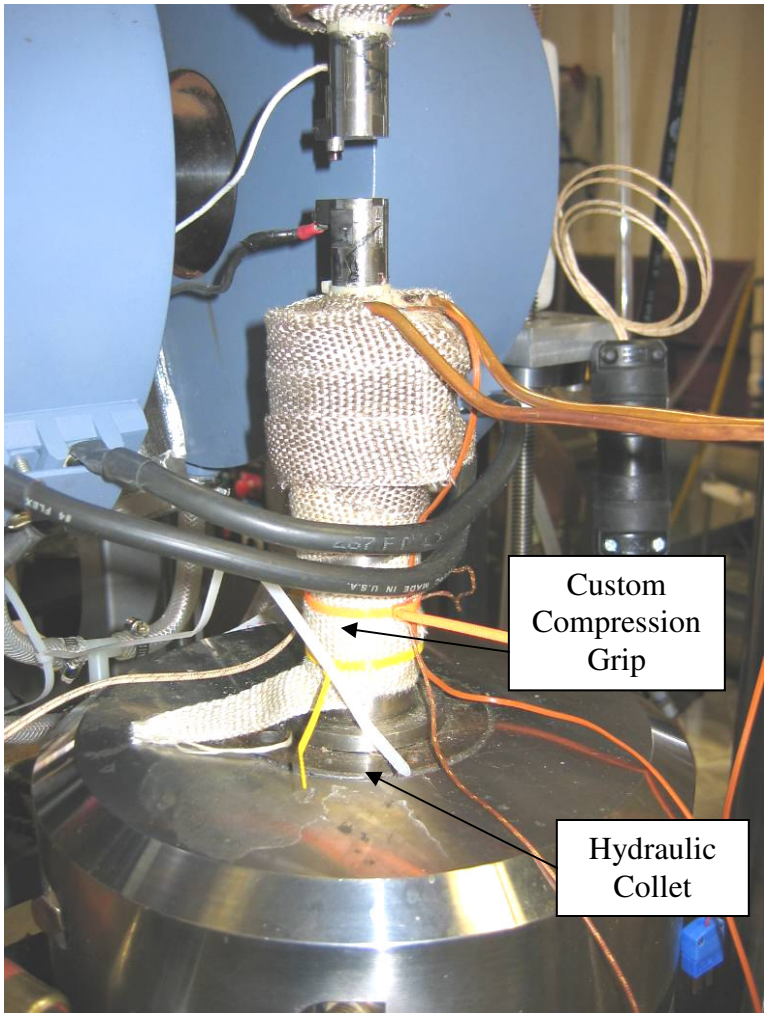

Figure 3.4 Custom compression grips installed using hydraulic collet grips.

c. Custom-Built Thermal Control System

In order to experimentally observe martensitic transformation and accurately identify the associated transformation temperatures, the thermal control system, shown in Figure 3.5, must meet several requirements:

- Must be capable of cooling the samples down to approximately -120°C.
- Must be capable of heating sample to approximately 400°C.
- Must heat/cool at a rate of approximately 10°C/min.
- Must maintain set temperature to ±1°C.

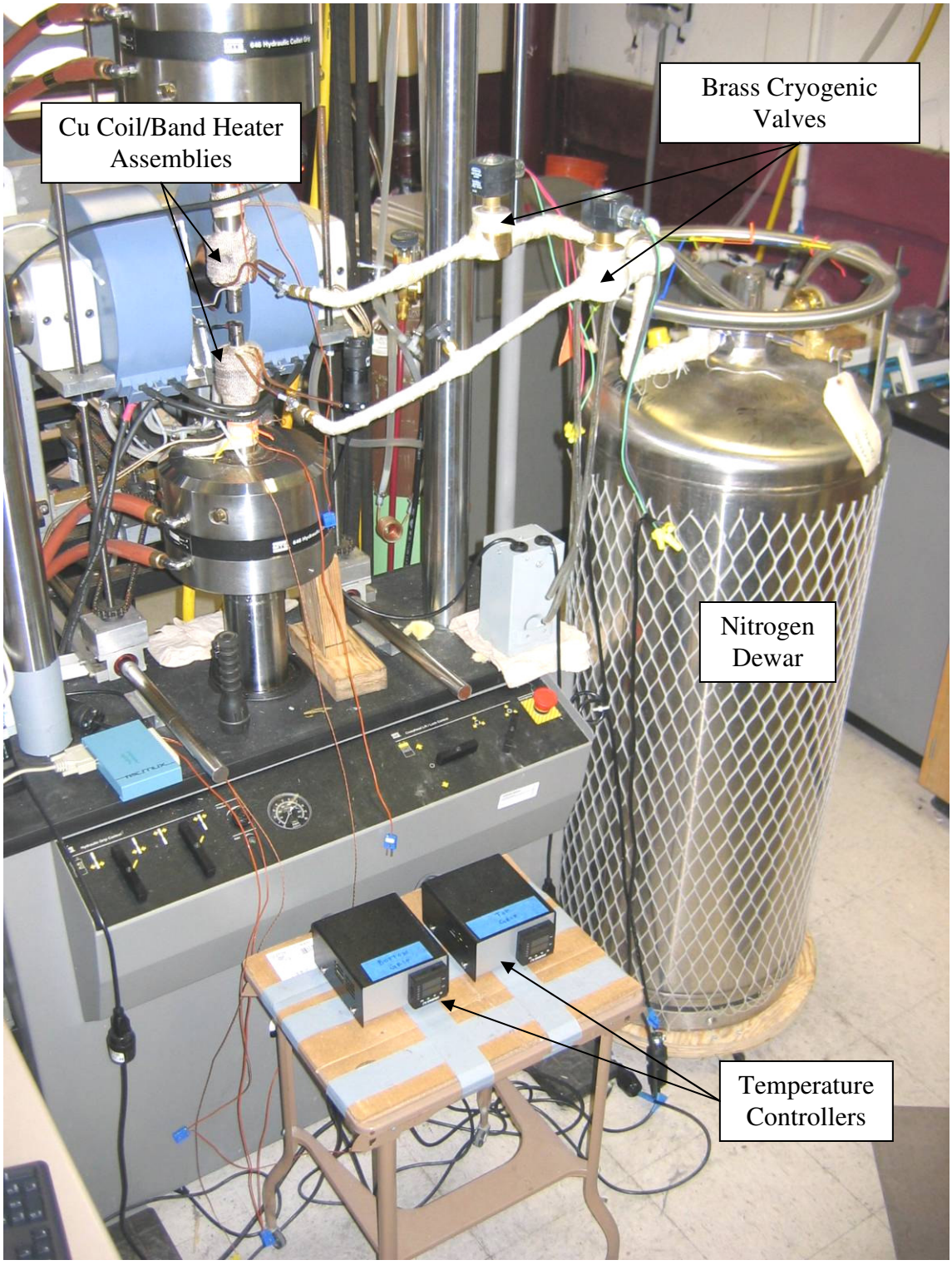

Figure 3.5 The complete custom-made thermal management system.

The selected mode of heat transfer used to control the temperature of the sample is conduction. Sample temperature is controlled by either heating or cooling the compression grips. In order to ensure the only mode of heat transfer present is conduction, a custom-built lexan box is used to minimize the convective heat transfer coefficient of the air surrounding the sample, ultimately reducing the temperature fluctuation due to convection. The custom lexan box can be seen in Figure 3.6. The lexan box fits securely between the electromagnet pole pieces and has recess holes allowing for unrestricted movement of the compression grips for testing.

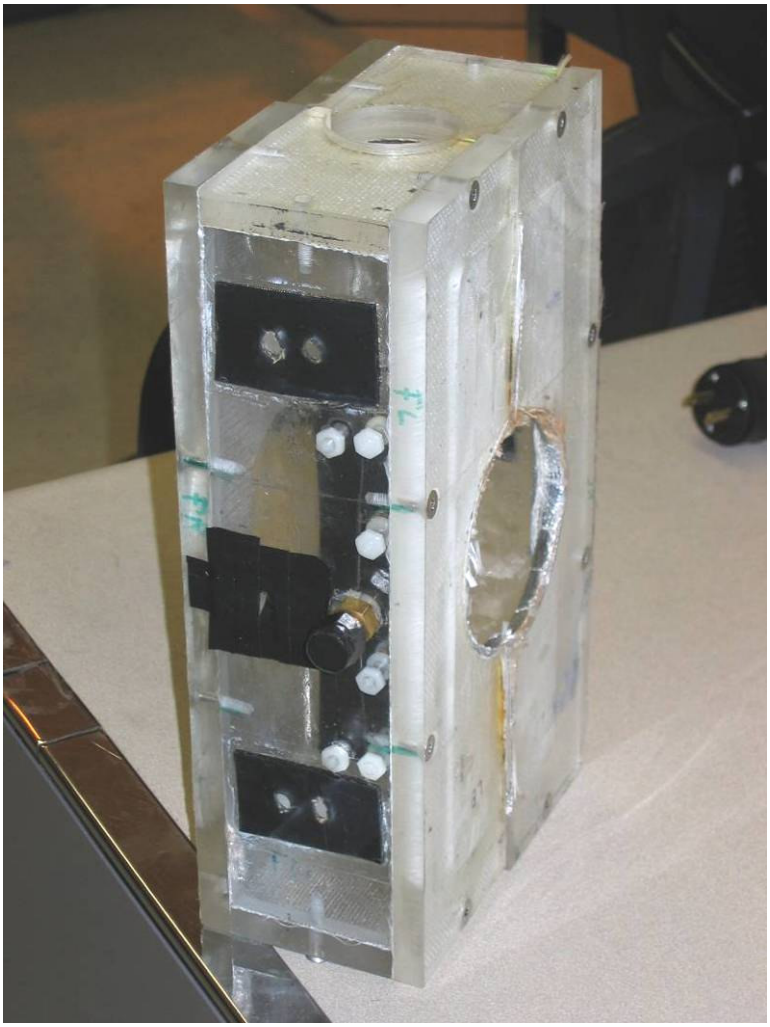

Figure 3.6 Custom lexan box with recess holes for electromagnet pole pieces and compression grips.

In order to achieve a minimum operating temperature of approximately -120°C, the compression grips are cooled using liquid nitrogen. The liquid nitrogen is supplied via two cryogenic grade ON/OFF brass solenoid valves, and is channeled through a pair of Cu coil windings press-fit to both the upper and lower grips. The Cu coil windings were manufactured using 3/16 in diameter Cu tubing and can be seen in Figure 3.7.

Figure 3.7 Cu coil windings used to channel liquid nitrogen.

The sample is heated using a pair of austenitic stainless steel thin-band mica heaters (Watlow, STB2C2AA-4) securely fastened around the Cu coil windings on both the upper and lower grips. The thin-band mica heaters can be seen in Figure 3.8.

Figure 3.8 Watlow thin-band mica heater used to heat compression grips.

The thin-band mica heaters are approximately 2 in wide and have a thickness of about 1/16 in. For maximum output, the heaters require 1A current and 240V. In order to supply sufficient power to the heaters, wall outlet voltage was increased from 120V to roughly 240V using two step-up transformers at 1A each. The transformers (ACME, T-2-53007-S) used can be seen in Figure 3.9. Under maximum operating conditions, the heaters are capable of reaching nearly 500°C.

Figure 3.9 ACME step-up transformer used to increase the voltage supplied to heaters.

In order to manage the heating and cooling systems during testing, a custom thermal management system, utilizing Proportional-Integral-Derivative (PID) control, was designed and fabricated. The thermal management system consists of two separate circuits, each consisting of an Omega brand temperature controller (model CN8202-R1-DC2-C2), which has multiple output capability. To maintain better thermal control and response, the temperature of each grip is controlled separately via a temperature controller, which can be seen in Figure 3.10.

Figure 3.10 Temperature controller used to control thermal management system.

The temperature controller's first output controls the cooling system, while the second output controls the heating system. Using a nonmagnetic T-type thermocouple affixed to the grips, the temperature controller measures the input temperature. If the input temperature is greater than the user-defined setpoint temperature, then the cooling system is activated. Likewise, if the input temperature is lower than the setpoint temperature, then the heating system is activated. After auto-tuning, the thermal

management system is capable of maintaining the temperature of the specimen to within ±1°C. Also, by using the temperature controller's ramp-soak function, a heating-cooling recipe can be programmed resulting in user-defined heating/cooling rate of 10°C/min.

d. Electromagnet

A Lake Shore Model EM4-CS electromagnet was combined with the MTS servo-hydraulic load frame and used to generate uniform magnetic fields up to 1.6 Tesla in a 2.5 cm x 2.5 cm x 2.5 cm control volume. The electromagnet is energized by a Lake Shore switching power supply (model 662) that is capable of producing ±35V and ±70A. The electromagnet can be seen in Figure 3.11.

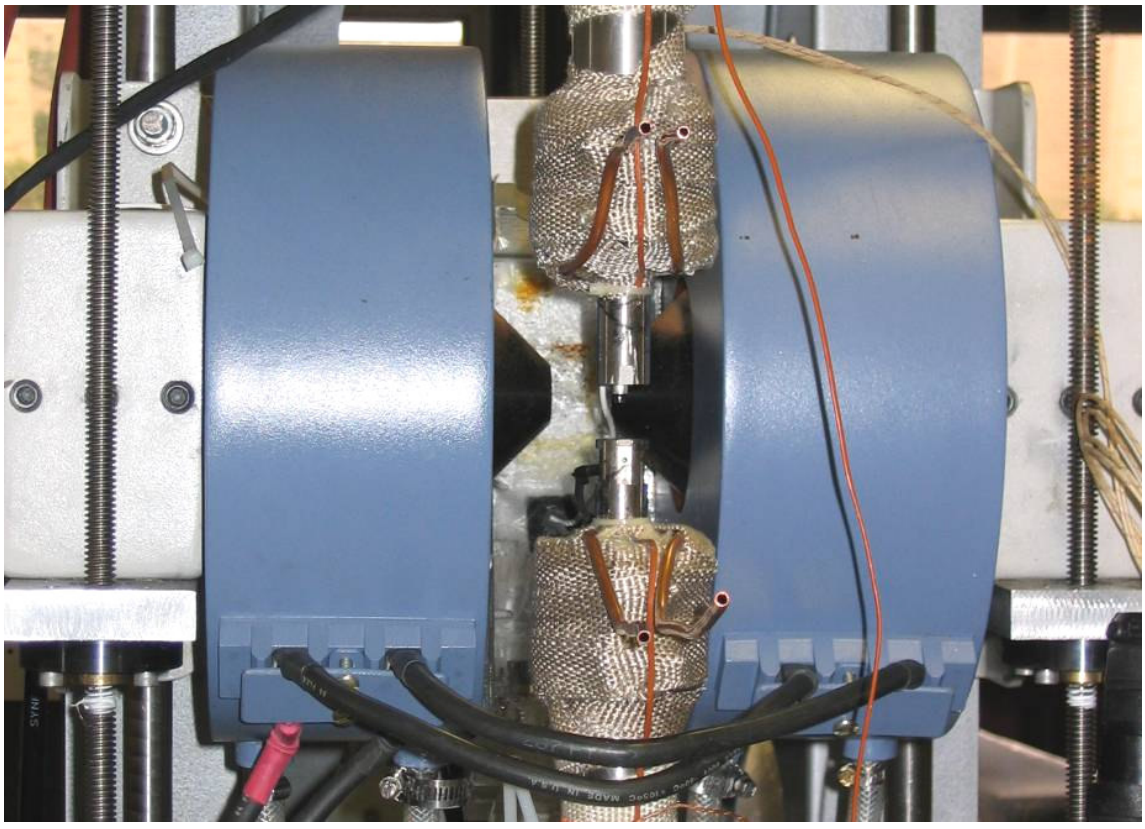

Figure 3.11 Lake Shore Model EM4-CS electromagnet.

The magnetic field measurements are performed by a Lake Shore model 450 gaussmeter utilizing a Lake Shore high sensitivity cryogenic transverse Hall probe with a resolution of ±0.00001 Tesla within ±30 Tesla range. The probe is positioned away from the specimen lying perpendicular to the magnetic field lines in between the pole pieces of the electromagnet. The gaussmeter and Hall probe sensor can be seen in Figure 3.12.

Figure 3.12 LakeShore 450 Gaussmeter and cryogenic transverse Hall Probe used to control electromagnet.

e. Experimental Details

In all of the experiments conducted, a non-magnetic T-type thermocouple is attached to outer surface of the specimen via thin, non-magnetic wire. This is done to

ensure that the thermocouple remains in constant contact with the sample for the duration of the experiment.

For thermal cycling tests, the externally applied compressive stress is held constant, while the temperature is cycled at a constant rate of 10°C/min. On the other hand, for pseudoelasticity tests, the temperature is held constant while the sample is loaded under displacement control at a strain rate of 0.004 mm/s and unloaded under force control at a rate of 10 N/s.

During thermal cycling and pseudoelasticity tests, data such as time, crosshead displacement, force, capacitive displacement, and temperature are recorded. From this data the stress and strain can be obtained.

CHAPTER IV

Ni_2MnGa RESULTS AND DISCUSSION

4.1 Testing Procedure

Since Ni_2MnGa has been known to exhibit multiple phase transformations, DSC and SQUID tests were conducted in order to experimentally determine the transformation temperatures for each phase. Likewise, in order to determine the transformation behavior of Ni_2MnGa as a function of temperature and stress, and to construct the stress-temperature phase diagram, two types of experiments were conducted: thermal cycling (a.k.a. heating-cooling tests) under constant stress levels (isobaric) and pseudoelasticity under constant temperatures (almost isothermal). Thermal cycling was used to determine the transformation temperatures at constant stress levels, while pseudoelasticity was used to identify the critical stresses for transformation at constant temperatures.

a. Differential Scanning Calorimetry (DSC)

A Perkin Elmer Pyris 1 Differential Scanning Calorimeter was used to measure the heat flow through the specimen as a function of temperature. As temperature was decreased at a rate of 10°C/min, the amount of heat flow required to change the sample temperature 1°C was measured. Upon phase transformation, the heat flow required changes abruptly, identifying the transformation temperatures. These transformation temperatures are then used to identify the different phases and the transformation sequence.

b. Superconducting Quantum Interference Device (SQUID)

SQUID tests were conducted in order to determine the magnetization of Ni_2MnGa as a function of temperature. The magnetization of Ni_2MnGa was determined by cycling the temperature from about -120°C up to 20°C under magnetic field. SQUID measurements are typically more sensitive and may sometimes reveal something that other methods might fail to notice. The data obtained from the SQUID measurements

may be used to determine the transformation temperatures for the different phases, as well as aid in identifying the phase transformation sequence.

c. Thermal Cycling

Strain was recorded as temperature was cycled between a temperature below M_f (martensite finish) and a temperature greater than A_f (austenite finish) under constant stress levels. Stress was incrementally increased in order to observe the shift in transformation temperatures, resulting in the construction of the Clausius-Clapeyron relationship for the various phases. Since the I-phase to X-phase transformation occurs at low stress levels [27], thermal cycling was performed at low stress levels in increments of 5 MPa in order to better understand the transformation behavior from parent phase to X-phase to I-phase to 10M martensite. At higher stress levels, thermal cycling was used to observe the transformation behavior from parent phase to X-phase to 10M martensite. The data recorded was subsequently analyzed and utilized to construct the stress-temperature phase diagram for Ni_2MnGa.

d. Pseudoelasticity

The stress-strain behavior of Ni_2MnGa was recorded at constant temperatures. Temperature was incrementally increased in order to observe the shift in critical stress for phase transformation. During the pseudoelasticity experiments, the sample was strained until the end of the transformation plateau (completely detwinned martensite). First, pseudoelasticity tests were conducted at different temperatures (in increments of 10°C) in the temperature range where the X-phase is known to exist [27-29], in order to demonstrate the two stage transformation behavior. However, it has been shown upon reverse transformation that the elastic region of the X-phase exhibits a small hysteresis, which indicates that the stress induced 10M martensite does not completely transform to the X-phase upon unloading [27]. Therefore, in order to better understand the I-phase to X-phase transformation behavior without the impact from the X-phase to 10M martensite transformation, pseudoelasticity tests were conducted in the low stress

regime. Lastly, pseudoelasticity tests were carried out at higher temperatures to determine the parent phase to X-phase transformation behavior. The critical stress for transformation was plotted as a function of temperature, yielding the Clausius-Clapeyron relationship for the various phases, which was then used to augment the stress-temperature phase diagram for Ni_2MnGa.

4.2 DSC Results

DSC was performed on a small Ni_2MnGa sample that weighed approximately 29.68 mg. The sample was sealed in a small aluminum pan, and then cycled twice between -60°C and 100°C. Heat flow vs. temperature for this specimen may be seen in Figure 4.1.

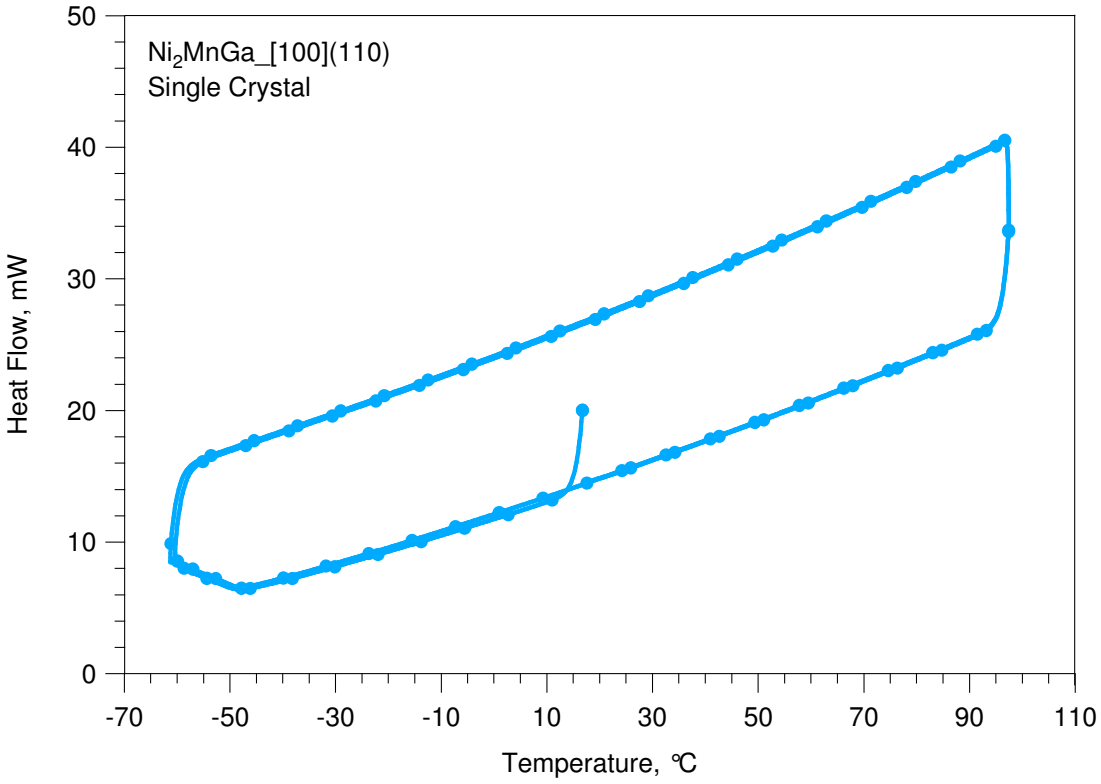

Figure 4.1 DSC results, showing heat flow vs. temperature, for Ni_2MnGa single crystal sample.

As can be seen in Figure 4.1, the existence of a phase transformation is not apparent. This implies that the martensitic transformation occurs at a temperature below -60°C and that, at zero stress, the parent phase transforms directly to the I-phase and not the X-phase. The reason that the parent to I-phase transformation does not appear in the DSC results is due to gradual phonon softening of the I-phase as temperature is decreased. Therefore, the X-phase may only be observed under an externally applied stress.

4.3 SQUID Results

SQUID was used to determine the magnetization of Ni_2MnGa as a function of temperature under an applied magnetic field of 200 Gauss. The results can be seen in Figure 4.2.

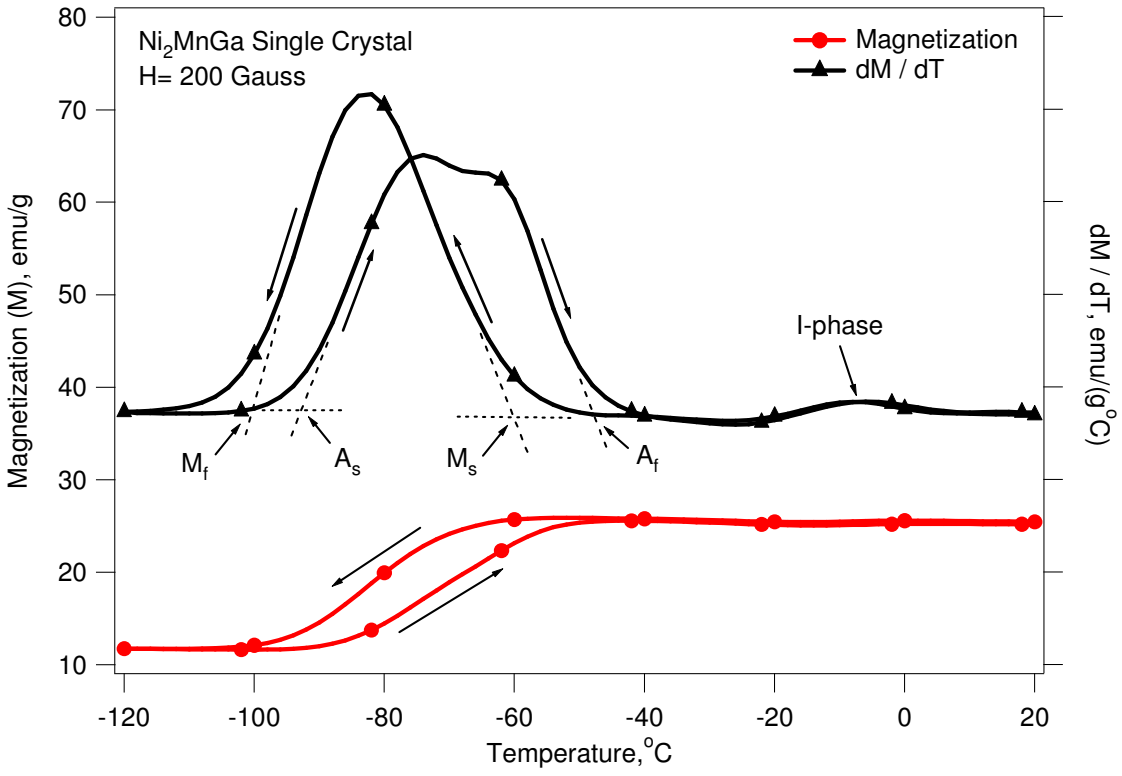

Figure 4.2 Magnetization as a function of temperature under magnetic field of 200 Gauss, as well as the derivative of the response detailing the transformation temperatures for the parent to I-phase to 10M martensite transformation sequence.

The magnetization curve, determined using SQUID, was then differentiated with respect to temperature and can also be seen in Figure 4.2. The dM/dT curve illustrates two separate phase transformations. The higher temperature, small peak on the right side of the figure represents the transformation from the parent phase to the I-phase, while the low temperature, larger peak on the left side of the figure represents the phase transformation from the I-phase to 10M martensite. Therefore, in agreement with previously reported results [27-29], the X-phase may only be observed under an externally applied load.

4.4 Thermal Cycling Results

Thermal cycling was conducted at stress levels ranging from 5 MPa up to 100 MPa. Since transformation from the I-phase to the X-phase occurs at low stress levels, thermal cycling was conducted at stress levels ranging from 5 MPa to 25 MPa in 5 MPa increments. The heating-cooling results for the low-stress conditions can be seen in Figure 4.3. As can be seen from the figure, the specimen exhibits approximately 4% transformation strain, which is expected of 10M martensite. Likewise, the transformation temperature for the I-phase to 10M martensite transformation increases with increasing stress, resulting in the expected positive Clausius-Clapeyron slope.

The lower stress region, where the parent phase to X-phase to I-phase transformation sequence occurs, may be seen in more detail in Figure 4.4. As can be seen in figure, the X-phase to I-phase transformation occurs at stress levels at or below 20 MPa, while the X-phase to martensite transformation occurs above 25 MPa. By following the thermal cycle curve for 20 MPa, the multiple phase transformation sequence can be seen. From these results, it becomes apparent that the temperatures for X-phase to I-phase transformation decrease with increasing stress level, up to about 25 MPa. This behavior is unique as it results in a negative Clausius-Clapeyron slope. On the other hand, the transformation temperatures for parent phase to X-phase and I-phase to 10M martensite increase with increasing stress levels, which are expected.

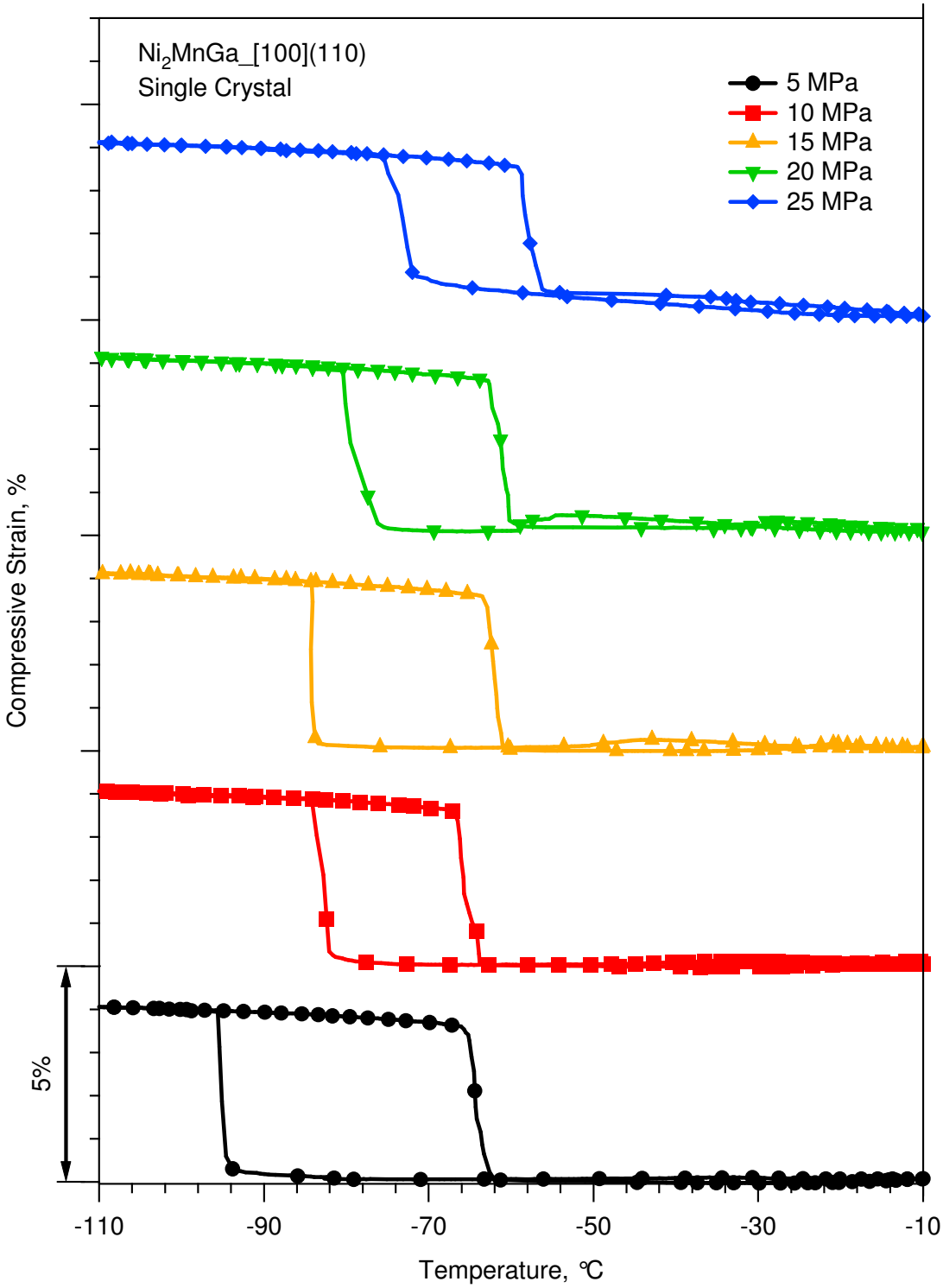

Figure 4.3 Low-stress thermal cycling results showing the increase in transformation temperatures with increasing stress levels.

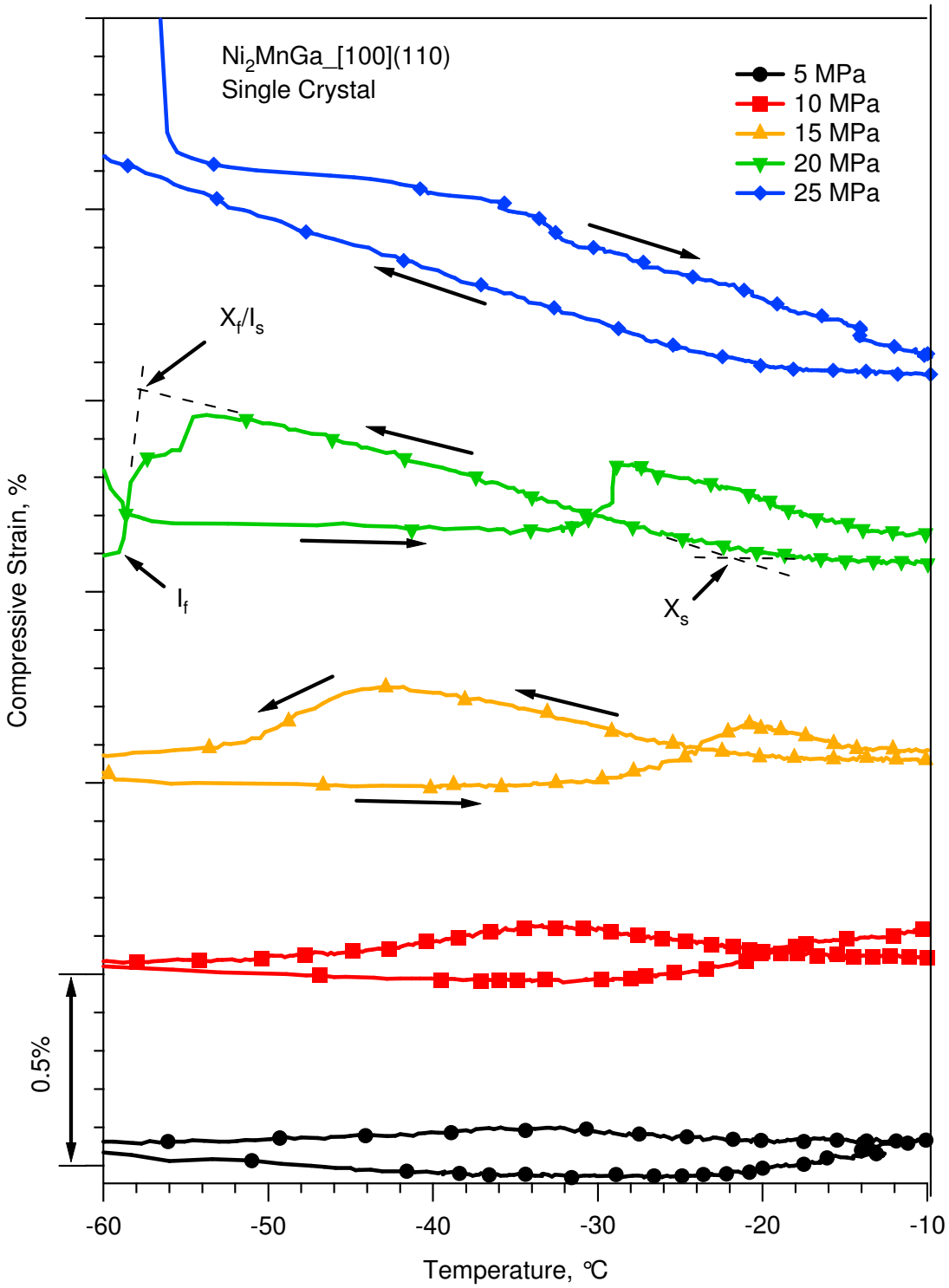

Figure 4.4 Low-stress thermal cycling results detailing the X-phase transformation.

Figure 4.5 details the multiple phase transformation sequence that occurs in Ni_2MnGa. Initially, the specimen is held at 20 MPa at an elevated temperature. Upon cooling, the specimen transforms from the parent phase to the X-phase. This transformation is denoted by the steadily increasing strain as temperature decreases. The specimen then transforms from the X-phase to the I-phase. Since the I-phase is similar in structure to the parent phase, the X-phase to I-phase transformation results in a tensile strain. Therefore, as the specimen transforms to the I-phase, the strain obtained from the X-phase is diminished. Finally, upon cooling the specimen transforms from the I-phase to 10M martensite.

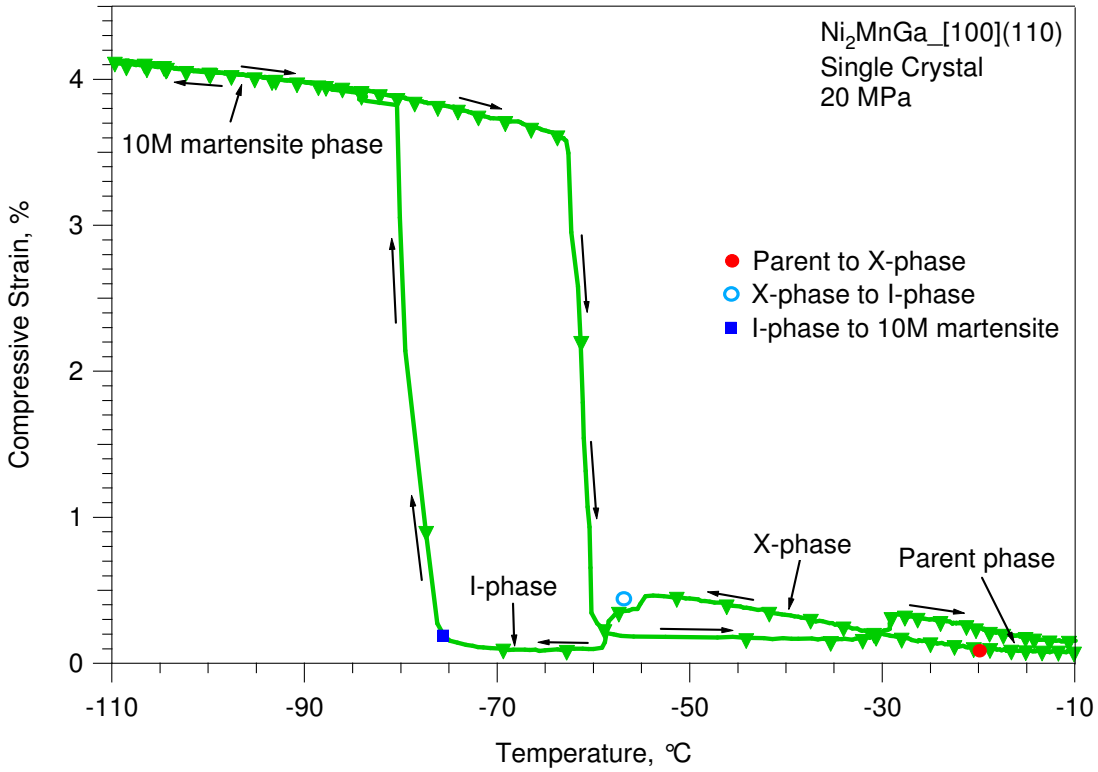

Figure 4.5 Thermal cycling response under a compressive load of 20 MPa illustrating the parent phase to X-phase to I-phase to 10M martensite transformation sequence in detail.

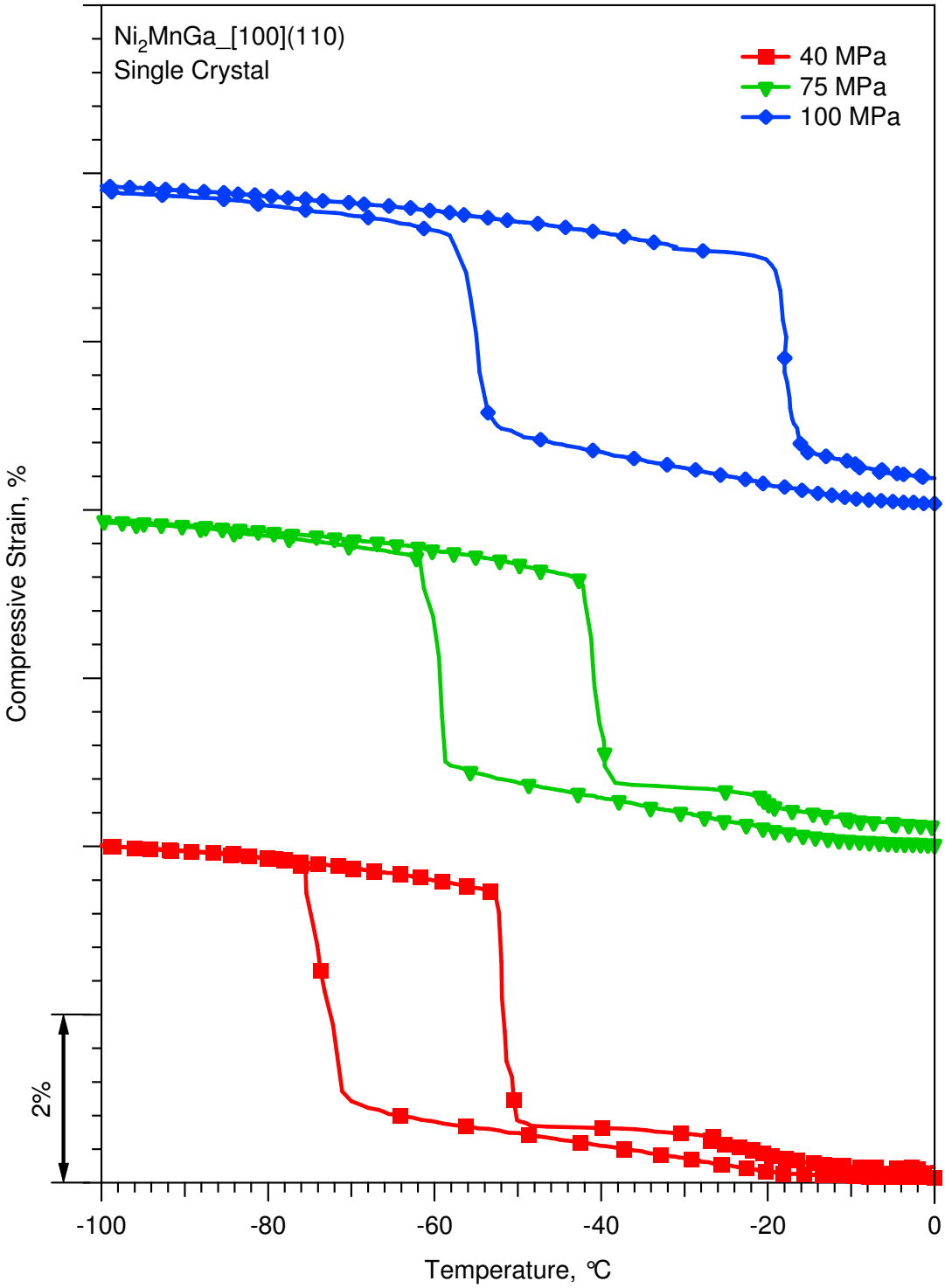

Figure 4.6 The phase transformation from austenite to X-phase to 10M martensite at stress levels greater than 25 MPa.

The heating-cooling curves for the higher stress levels (40 MPa to 100 MPa) can be seen in Figure 4.6. Since the applied stress levels are greater than 25 MPa, the austenite parent phase transforms directly to the X-phase. As can be seen from the figure, the specimen transforms from the parent phase to the X-phase and strain increases. However, unlike the response at lower stress levels, the specimen does not exhibit a tensile strain upon continued cooling. This implies that the X-phase transforms directly to the 10M martensite phase. This behavior occurs at stress levels at or above 25 MPa. As expected, the transformation temperatures for the parent phase to X-phase transformation increase with increasing stress levels.

4.5 Pseudoelasticity Results

The low-temperature pseudoelastic response of Ni_2MnGa showing two-stage phase transformation can be seen in Figure 4.7. As predicted by the heating-cooling curves, the transformation from the I-phase to the X-phase, denoted as the first stage, occurs at very low stress levels. The transformation from the X-phase to 10M martensite occurs upon continued loading. As illustrated by the pseudoelastic response at -50°C, a small hysteresis exists in the X-phase, which implies that the 10M martensite does not fully transform to the X-phase upon reverse transformation. In order to obtain the I-phase to X-phase transformation behavior without the impact from the 10M martensite, pseudoelastic tests were conducted on the first stage transformation, which can be seen in Figure 4.8.

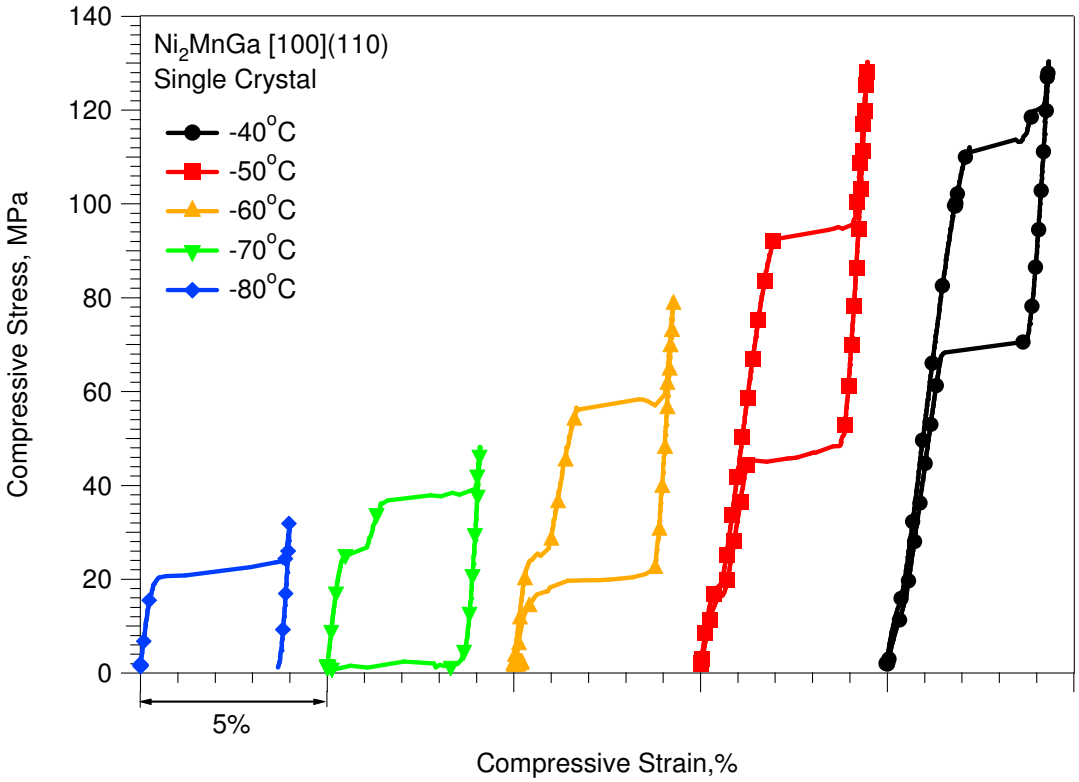

Figure 4.7 Low temperature pseudoelastic response for Ni_2MnGa showing two-stage phase transformations: I-phase to X-phase and X-phase to 10M martensite.

As previously shown by the thermal cycling results, the critical stress required for the I-phase to X-phase transformation decreases with increasing temperature. This behavior has been shown to occur at temperatures between -70°C and -30°C. However, the pseudoelastic response of Ni_2MnGa at -80°C exhibits only one stage transformation with a critical stress lower than that required at -70°C (Figure 4.5.1), which doesn't follow the trend previously discussed. This behavior illustrates that the phase transformation from I-phase to X-phase ceases to exist at temperatures between -70°C and -80°C. Below -80°C, the I-phase transforms directly to 10M martensite. Conversely, at temperatures above -30°C, the first stage transformation begins to disappear.

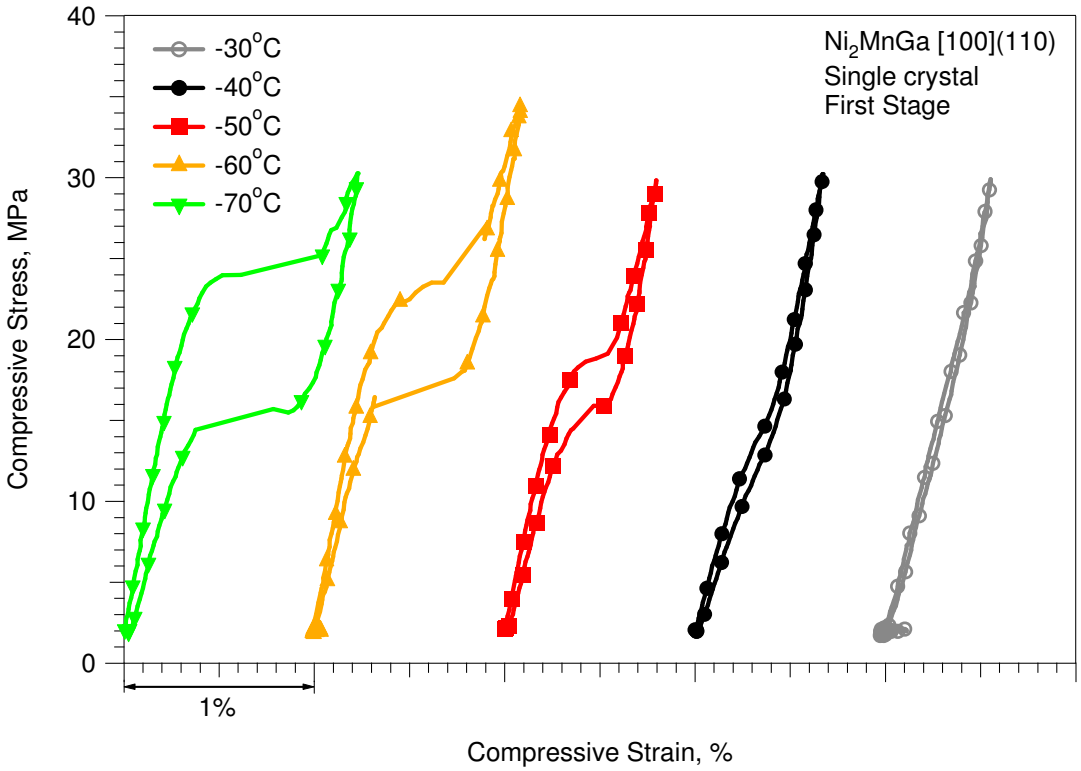

Figure 4.8 Stress-strain behavior of Ni_2MnGa detailing the first stage, I-phase to X-phase, transformation. The first stage exhibits a decrease in critical stress as temperature increases.

Figure 4.9 shows the pseudoelastic response of Ni_2MnGa at temperatures higher than -40°C. As can be seen, the critical stress necessary for phase transformation increases with increasing temperature, which is expected. However, the phase transformation shown in the pseudoelastic response does not represent the parent phase to X-phase transformation that was predicted in the heating-cooling results. Rather, the transformation illustrated is the parent to 10M martensite phase transformation. One possible reason why the parent phase to X-phase transformation was not recorded may be due to the unknown crystal structure of the recently discovered X-phase. Since the discovery of this phase is relatively fresh, the shape memory characteristics are still unresolved.

As temperature increases, the stress required for detwinning increases and, at some temperature above 10°C, surpasses that required for dislocation slip. This explains the low stress hysteresis and lack of plateau in the pseudoelastic response at 10°C.

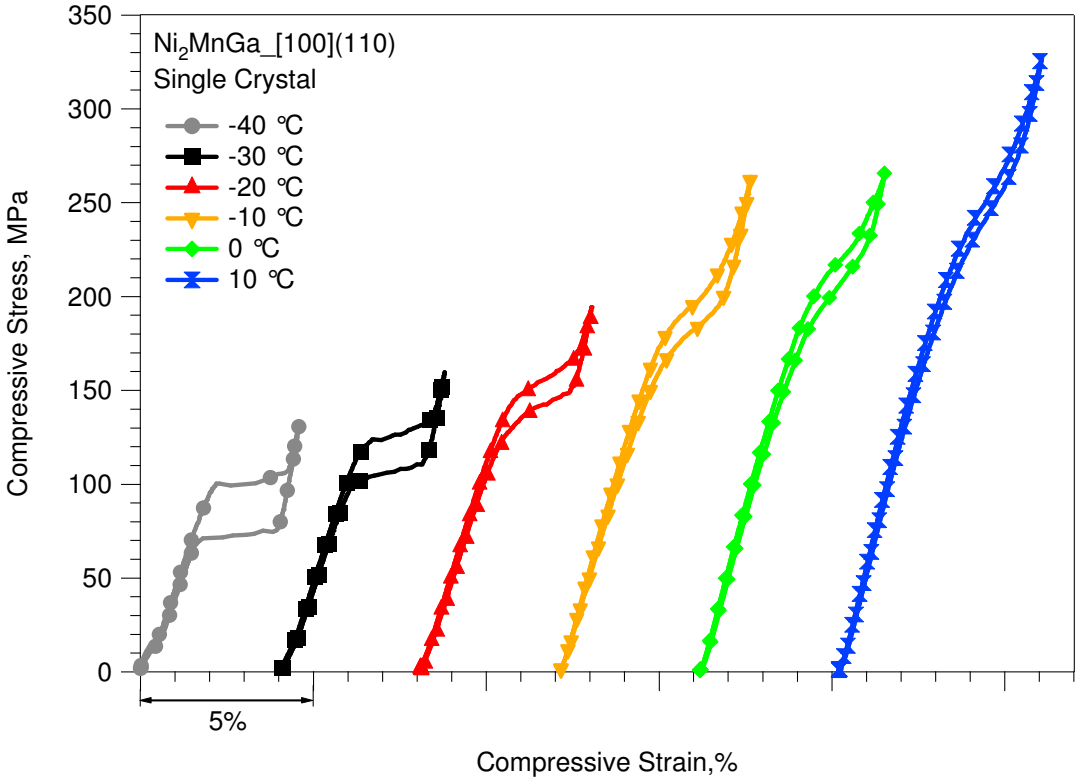

Figure 4.9 High temperature stress-strain behavior of Ni_2MnGa showing the parent to 10M martensite phase transformation.

4.6 Stress-Temperature Phase Diagram

The previously discussed results were analyzed and used to construct the stress-temperature phase diagram for Ni_2MnGa shown in Figure 4.10. The heating-cooling results were used to determine how the transformation temperatures for each phase changed as a function of externally applied compressive stress. This data was used to determine the Clausius-Clapeyron relationship of each phase. The martensite start (M_s), X-phase start (X_s), and the I-phase start (I_s) temperatures were determined using thermal cycling. Pseudoelasticity data was used to determine the stress-strain behavior of

Ni_2MnGa at different test temperatures. The critical stresses and temperatures were recorded and used to form the Clausius-Clapeyron relationship for each phase and can be seen in the stress-temperature phase diagram. The martensite start (M_s) and the I-phase start (I_s) temperatures were determined using pseudoelasticity. The heating-cooling results are shown with solid markers, while the pseudoelasticity results are shown with hollow markers.

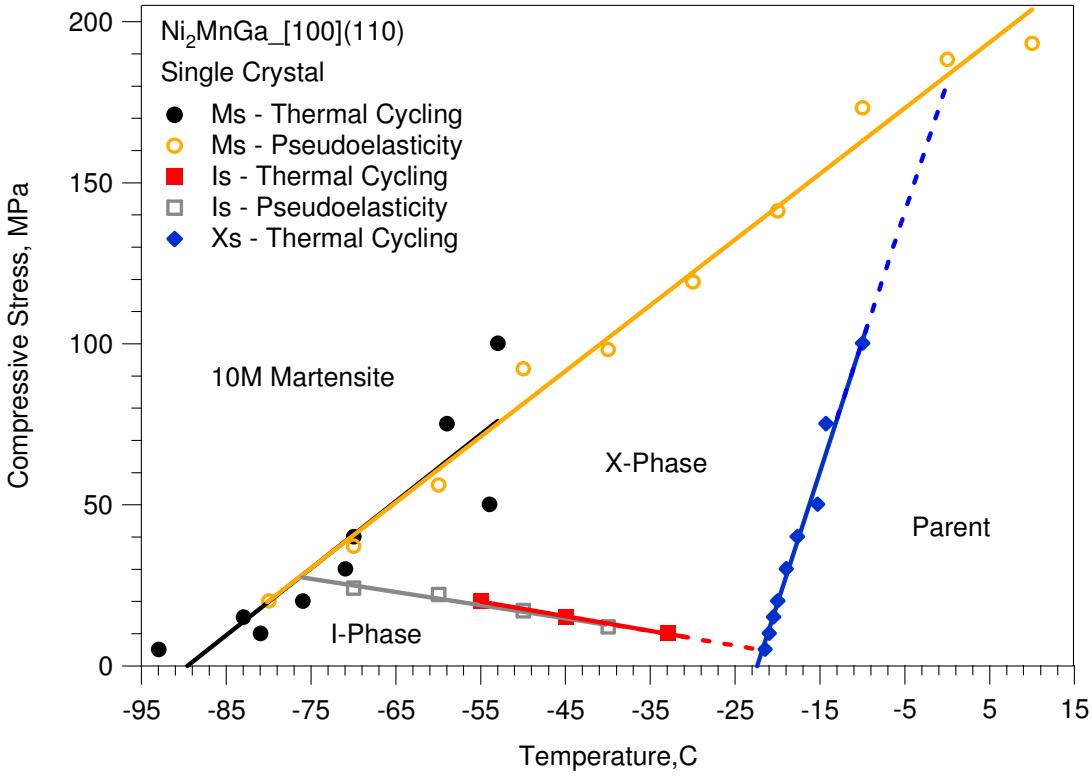

Figure 4.10 Stress-temperature diagram for Ni_2MnGa illustrating the multiple phase transformations.

As shown by the figure, the I-phase ↔ X-phase transformation temperatures decrease with increasing stress levels. This denotes a negative Clausius-Clapeyron relationship, which has been previously attributed to a change in the crystal structure of the X-phase as it approaches the I-phase [27]. For temperatures above -20°C, the I-phase ↔ X-phase transformation is not detected, however the parent phase ↔ X-phase

transformation may be seen. Identified by thermal cycling experiments, but not seen in the pseudoelastic response, the parent phase ↔ X-phase transformation exhibits an increase in transformation temperatures with increasing stress. This corresponds to a positive Clausius-Clapeyron slope, which is expected. However, at applied stress levels above 100 MPa, the parent phase ↔ X-phase transformation behavior is unknown, though it is expected to increase with the trend previously discussed and terminate at the parent phase ↔ 10M martensite transformation. The construction of the stress-temperature phase diagram shown in Figure 4.10 identifies the stress and temperature region where reversible magnetic field induced phase transformation is possible [28, 29], as well as the stress and temperature ranges where the X-phase exists.

CHAPTER V

NiMnCoIn RESULTS AND DISCUSSION

5.1 Theoretical Predictions

Using energy minimization methods [2], the orientation dependence of the transformation strain was determined. Knowing the lattice parameters of the parent and martensite phases the maximum theoretical transformation strain was calculated, and can be seen in Table 5.1.

Table 5.1 Summary of theoretical transformation strains for different crystallographic orientations in the NiMnCoIn single crystal system.

Theoretical Transformation Strain		
	Transformation	Detwinning
100		
14M	-5.81	-5.81
123		
14M	-3.68	-3.92
011		
14M	-2.87	-3.37

These theoretical predictions will be later compared to the experimentally determined transformation strains obtained during thermal cycling and pseudoelasticity tests. Also, these values will be used in conjunction with the experimentally determined Clausius-Clapeyron relationships to empirically determine the entropy of transformation.

5.2 Testing Procedure

As previously stated, NiMnCoIn experiments were carried out on two different batches. The first batch contained samples with long axes along the crystallographic

orientations: [100], [087], and [25 7 15]. The second batch contained samples with the long axes along the [100] crystallographic direction. The single crystals for each batch were grown the same way under the same conditions however, due to Mn evaporation during the crystal growth process [47, 50], the compositional makeup of each batch, and possibly each crystal, may be different.

With the intention of observing the transformation temperatures and the magnetic response of NiMnCoIn, both DSC and SQUID tests were conducted. DSC was used to determine the transformation temperatures under zero stress, while SQUID was used to verify the transformation temperatures and demonstrate the unique magnetic properties inherent to this new alloy. In order to determine the transformation behavior of NiMnCoIn as a function of temperature and stress, two types of experiments were conducted: thermal cycling (a.k.a. heating-cooling tests) and pseudoelasticity. Thermal cycling was used to determine the transformation temperatures at constant stress levels (isobaric), orientation dependence of transformation strain, and thermal hysteresis. Likewise, pseudoelasticity was used to identify the critical stresses for transformation at constant temperatures (isothermal), orientation dependence of transformation strain, and stress hysteresis. Pseudoelastic tests were performed both with and without magnetic field in order to determine the magnetostress as a function of magnetic field and the capability of NiMnCoIn to exhibit magnetic field induced phase transformation. Lastly, optical microscopy was conducted so as to gain an understanding of the fracture behavior in addition to quantifying the homogenization treatment.

a. Differential Scanning Calorimetry (DSC)

A Perkin Elmer Pyris 1 Differential Scanning Calorimeter was used to measure the heat flow through the specimen as a function of temperature. As temperature was decreased at a rate of 10°C/min, the amount of heat flow required to change the sample temperature 1°C was measured. Upon phase transformation, the heat flow required changes abruptly, identifying the transformation temperatures.

b. Superconducting Quantum Interference Device (SQUID)

SQUID tests were conducted in order to determine the magnetization of NiMnCoIn as functions of temperature and magnetic field. The dependence of magnetization on magnetic field was determined by cycling the magnetic field from 0 kOe to 70 kOe at different temperatures. The magnetization of NiMnCoIn as a function of temperature was determined by cycling the temperature from about 390K down to 50K under various magnetic fields. The data obtained from the SQUID measurements may be used to determine the effect of magnetic field on the transformation temperatures.

c. Thermal Cycling

Strain was recorded as temperature was cycled between a temperature below M_f (martensite finish) and a temperature greater than A_f (austenite finish) under constant stress levels. Stress was incrementally increased in order to observe the shift in transformation temperatures, resulting in the creation of the Clausius-Clapeyron relationship. The heating-cooling results were analyzed to experimentally deduce both the transformation strain and thermal hysteresis during transformation.

d. Pseudoelasticity

The stress-strain behavior of NiMnCoIn was recorded at constant temperatures. Temperature was incrementally increased in order to observe the shift in critical stress for phase transformation. The critical stress for transformation was combined with the thermal cycling results and plotted as a function of temperature, yielding the Clausius-Clapeyron relationship. Similar to thermal cycling, the pseudoelastic response was examined in order to measure the transformation strain and stress hysteresis during transformation. These findings were then used in conjunction with the thermal cycling results to estimate the entropy of transformation and to examine the possibility of reversible MFIPT.

e. Optical Microscopy

After testing, the samples were mechanically polished using the following sequence of grinding papers (grit): 180 → 240 → 400 → 600 → 800 → 1000 → 1200. After polishing with 1200 grit grinding paper, final polishing was done using 0.05 μm alumina powder. Optical micrographs were taken on a Nikon optical microscope. These micrographs were then used to study the mode of failure and to determine the quantity of precipitates (second phase) in the matrix.

5.3 DSC Results

a. NiMnCoIn Batch 1

Similar to Ni_2MnGa, DSC tests were conducted on both batches of NiMnCoIn. For the first batch, a small specimen weighing approximately 9.354 mg was sealed in an aluminum pan and cycled twice between -60°C and 100°C. The heat flow as a function of temperature may be seen in Figure 5.1. As can be seen, the peaks that denote phase transformation are very shallow and broad, which implies that the energy required for the nucleation of martensite is similar in magnitude to the energy required for propagation. Therefore, the martensitic transformation is expected to begin slowly and take several degrees to complete. Despite having broad and shallow peaks, the DSC results predict the martensite start temperature to occur at about -26°C. Upon heating another peak illustrates the reverse transformation from martensite to parent phase. This peak predicts that the reverse transformation will begin at approximately -10°C and finish at about 20°C, which is very long. This result implies that the specimen will exhibit a large thermal hysteresis on the order of approximately 40°C to 50°C.

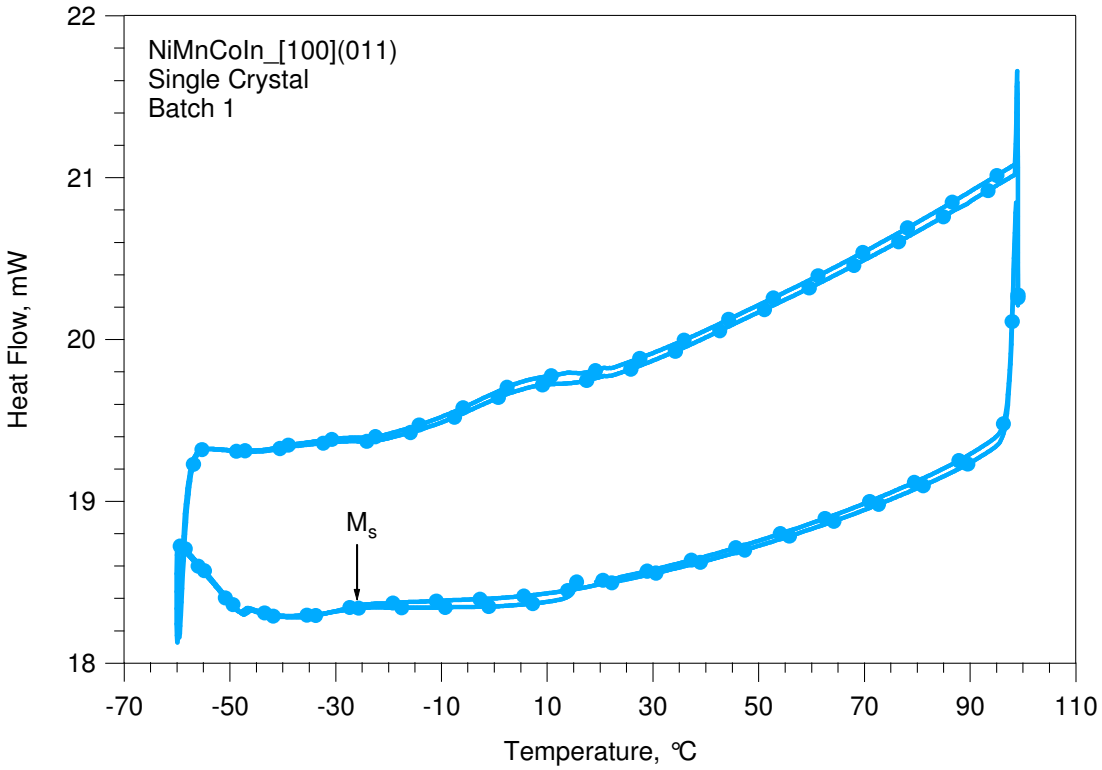

Figure 5.1 DSC results showing heat flow as a function of temperature for NiMnCoIn batch 1 specimen. Martensite start temperature is shown to be about -26°C.

b. NiMnCoIn Batch 2

For the second batch, a small specimen weighing approximately 34.3 mg was sealed in an aluminum pan and cycled twice between -60°C and 100°C. The heat flow as a function of temperature may be seen in Figure 5.2. As can be seen, the peak that denotes reverse phase transformation is very shallow and broad, similar to that shown for batch 1. The limits of the DSC prohibit the observation of the martensite transformation temperatures. Therefore, it can be expected that the martensite transformation temperatures are below -60°C. Upon heating, the peak predicts that the reverse transformation will begin at approximately -25°C and finish at about -5°C, which is shorter than that observed in batch 1.

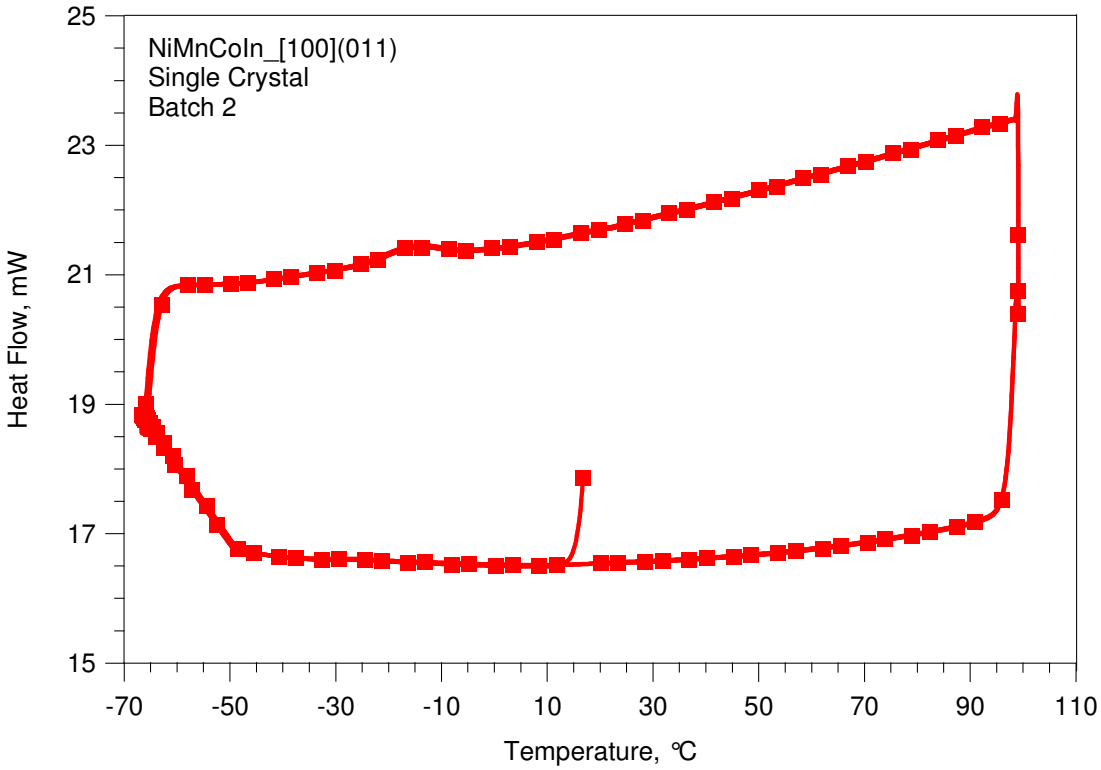

Figure 5.2 DSC results showing heat flow as a function of temperature for the NiMnCoIn batch 2 specimen. Martensitic transformation is expected below -60°C.

5.4 SQUID Results

a. NiMnCoIn Batch 1

SQUID tests were conducted in order to determine the effect of magnetic field on saturation magnetization and to determine the transformation temperatures. In order to better understand the meta-magnetic shape memory behavior of this new alloy, magnetization was measured as a function of magnetic field. This behavior may be seen in Figure 5.3. NiMnCoIn has been shown to exhibit ferromagnetic parent phase and paramagnetic martensite phase. However, as shown in the figure, the martensite phase of the NiMnCoIn samples from batch 1 are not fully paramagnetic as the saturation magnetization increases to approximately 20 emu/g. At 200K, the specimen is initially in the martensite phase. Upon the application of an external magnetic field, the sample begins to magnetize. At approximately 25 kOe, the energy required for phase

transformation is exceeded and MFIPT occurs. As the magnetic field is decreased, the specimen experiences a reverse transformation back to the martensite phase. Similar behavior may be observed at 250K though the sample is initially almost parent phase, which explains the higher saturation magnetization as magnetic field is increased.

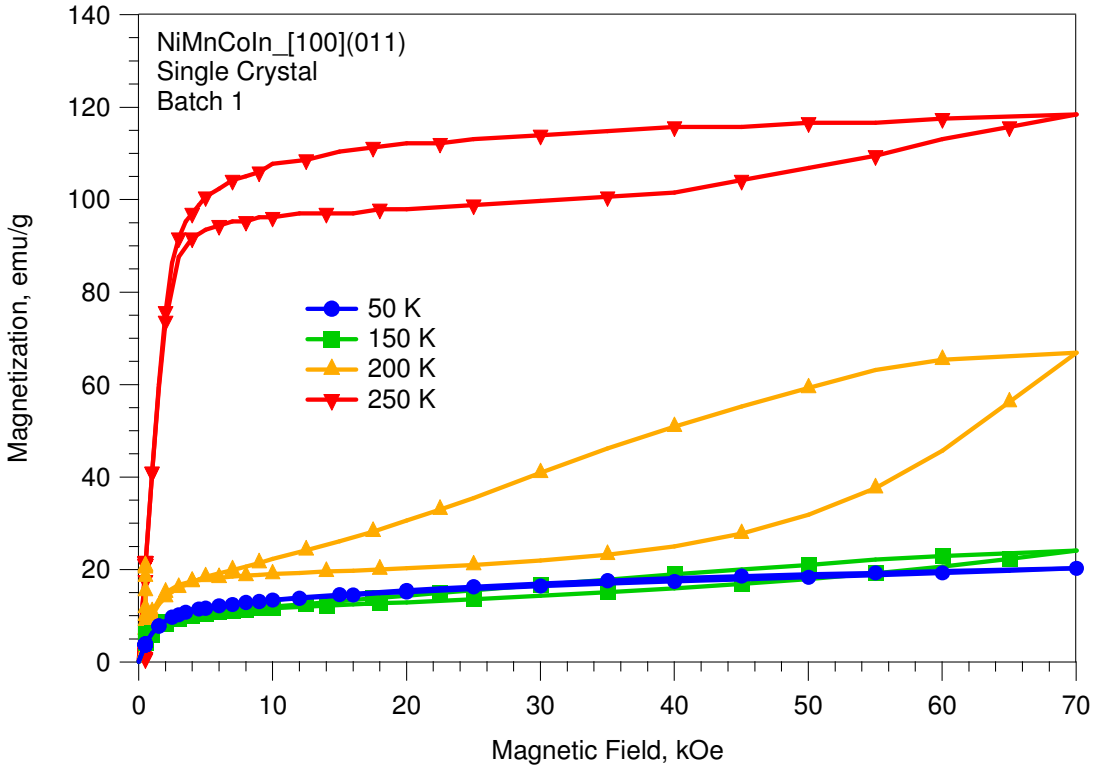

Figure 5.3 Magnetization of NiMnCoIn batch 1 sample as a function of externally applied magnetic field demonstrating fully reversible MFIPT.

The magnetization as a function of temperature was also determined. The results may be seen in Figure 5.4. The magnetization of the sample as a function of temperature was recorded at different magnetic fields. As magnetic field is increased, the transformation temperatures decrease, which is expected. However, as previously stated, the martensite phase is not fully paramagnetic, which clarifies why the saturation magnetization of the martensite upon phase transformation increases with magnetic

field. As predicted by the DSC results, the thermal hysteresis is nearly 50°C, which increases the magnetic field required for MFIPT to occur.

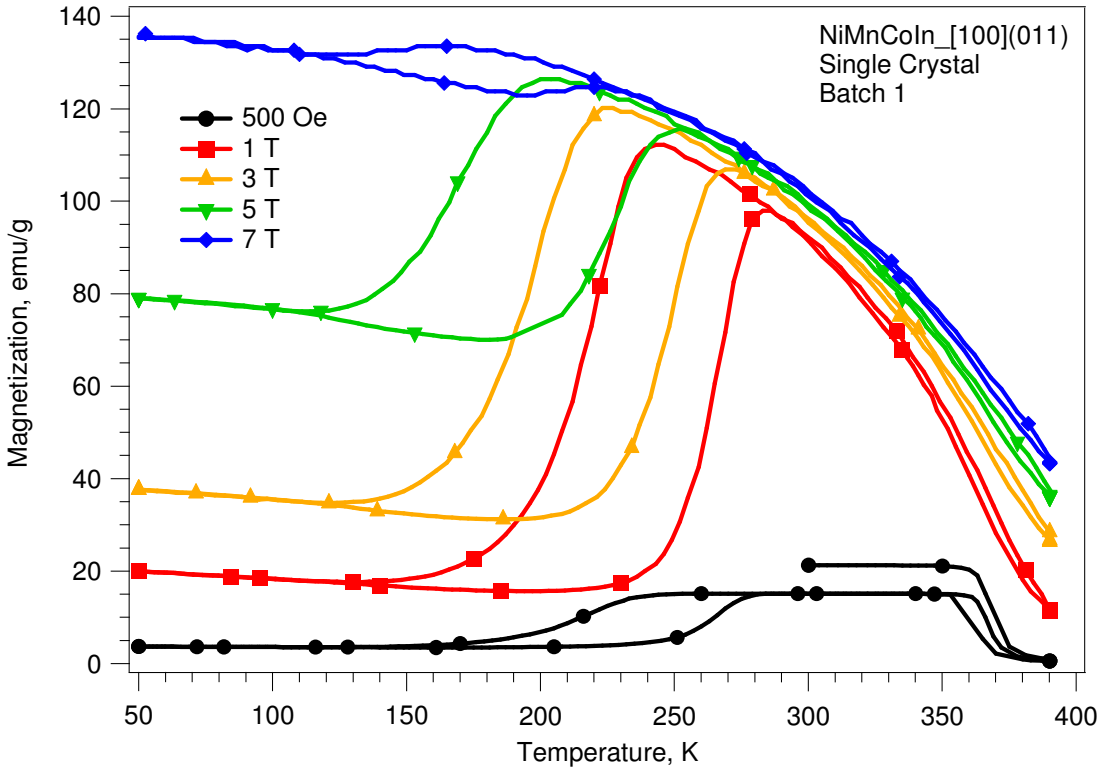

Figure 5.4 Magnetization of NiMnCoIn batch 1 sample as a function of temperature at different magnetic fields.

By differentiating the 500 Oe curve shown in Figure 5.4, one can determine the transformation temperatures. The magnetization versus temperature and the corresponding dM/dT curves for the 500 Oe case may be seen in Figure 5.5. As can be seen, the transformation temperature for the parent to martensite phase transformation is predicted to be about -28°C, which is in good agreement with the DSC results.

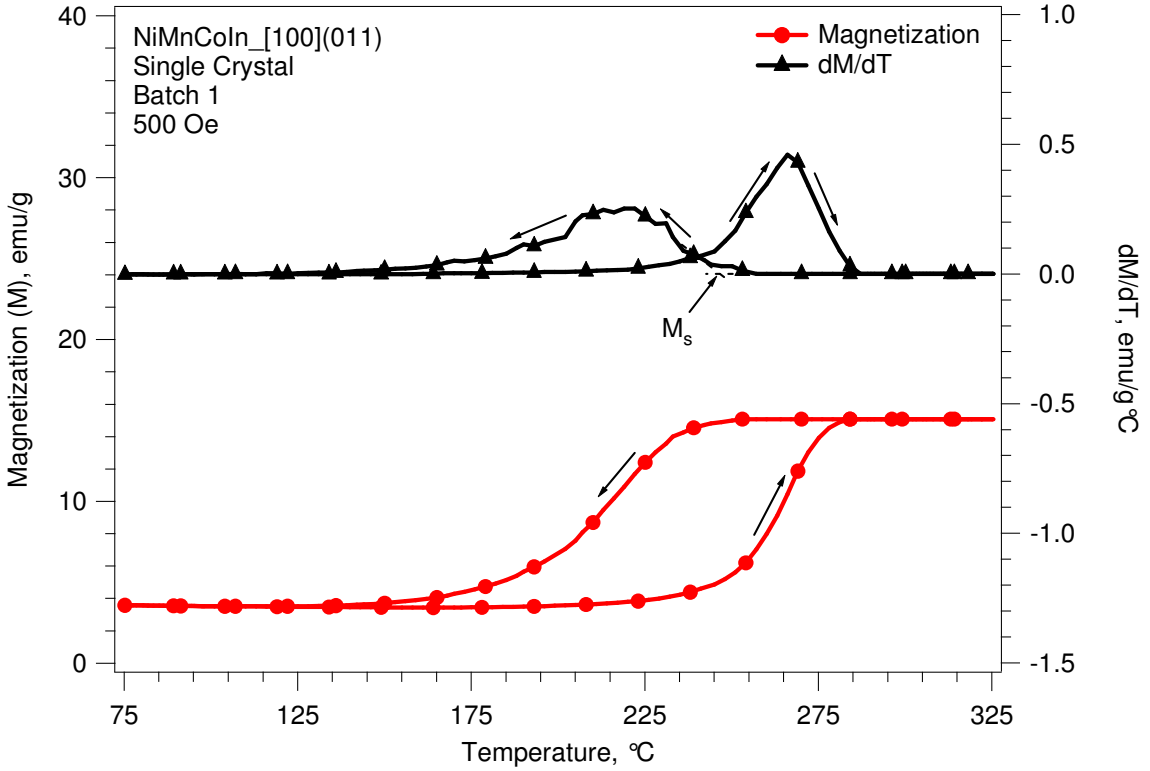

Figure 5.5 Magnetization as a function of temperature under 500 Oe externally applied magnetic field for NiMnCoIn batch 1. The dM/dT curve identifies the transformation temperatures.

By taking the derivatives of the magnetization curves with respect to temperature, it is possible to determine the effect of magnetic field on the transformation temperatures. The dM/dT curves were determined for each magnetic field and the transformation temperatures were recorded. The effect of magnetic field on transformation temperature can be seen in Figure 5.6. As magnetic field increases, the temperature decreases linearly at a rate of -9.25°C/T. Despite such a dramatic decrease in transformation temperatures, MFIPT is difficult due to the large thermal hysteresis.

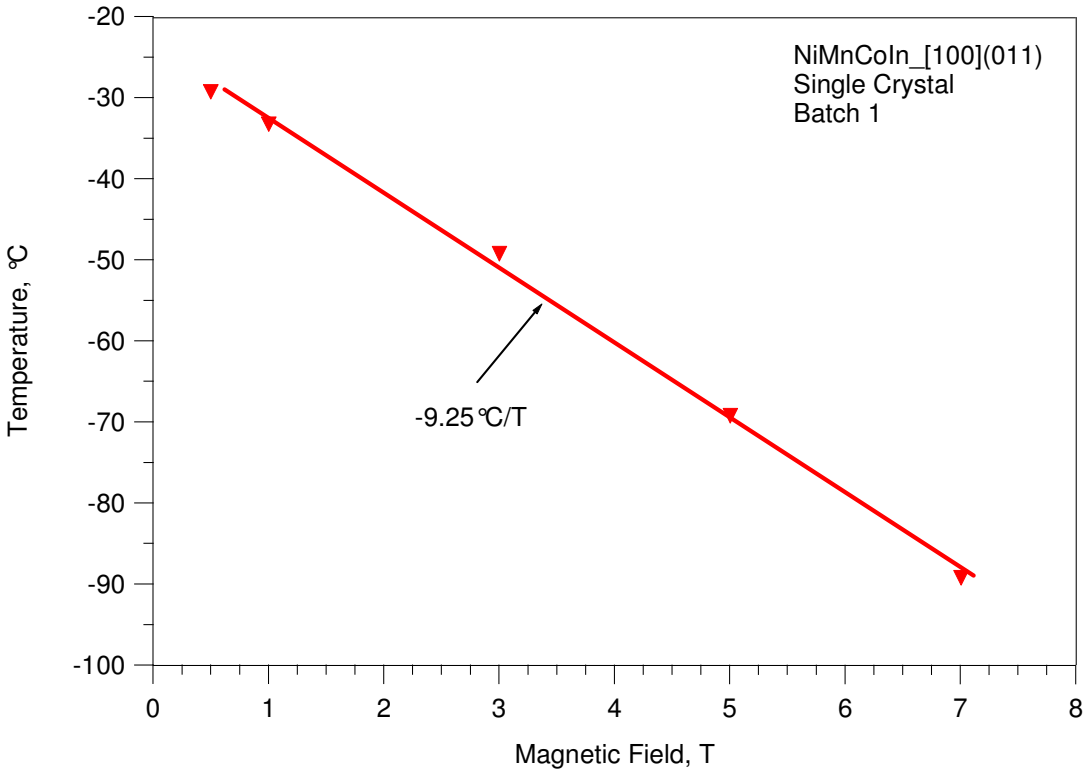

Figure 5.6 Temperature as a function of externally applied magnetic field for NiMnCoIn batch 1, as derived from the magnetization data obtained from SQUID measurements.

b. NiMnCoIn Batch 2

The magnetization of NiMnCoIn batch 2 as a function of temperature was measured using SQUID in order to gain an understanding of the magnetic properties of batch 2, as well as to determine the transformation temperatures. The effect of temperature on magnetization at different magnetic fields may be seen in Figure 5.7. As can be seen, the saturation magnetization of the martensite phase is significantly greater than that for batch 1. This means that the difference in saturation magnetizations between the parent and martensite phases is smaller, resulting in a much reduced Zeeman energy. As a result, the phase transformation is suppressed at higher magnetic fields. This is evidenced by the SQUID results for both 5T and 7T.

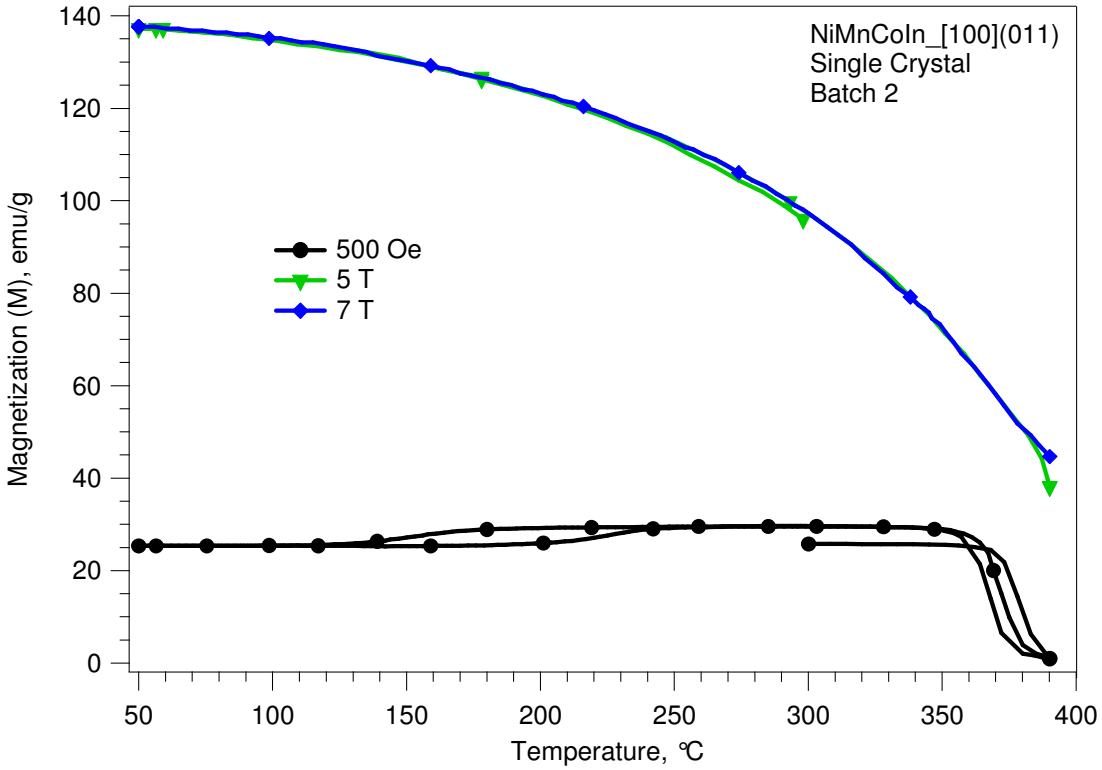

Figure 5.7 Magnetization as a function of temperature for different magnetic fields for NiMnCoIn batch 2, as obtained from SQUID measurements.

Similar to the results obtained for batch 1, the magnetization was differentiated with respect to temperature in order to determine the transformation temperatures. The magnetization and dM/dT curves may be seen in Figure 5.8. As predicted by the DSC results, the transformation temperature is expected to be about -75°C, which is well below the lower limit of the DSC. Likewise, the transformation from parent to martensite is expected to take several degrees and the thermal hysteresis during the transformation is expected to be very large. Since the phase transformation at high magnetic fields was suppressed due to the large saturation magnetization of the martensite phase, the effect of magnetic field on transformation temperature was not obtainable.

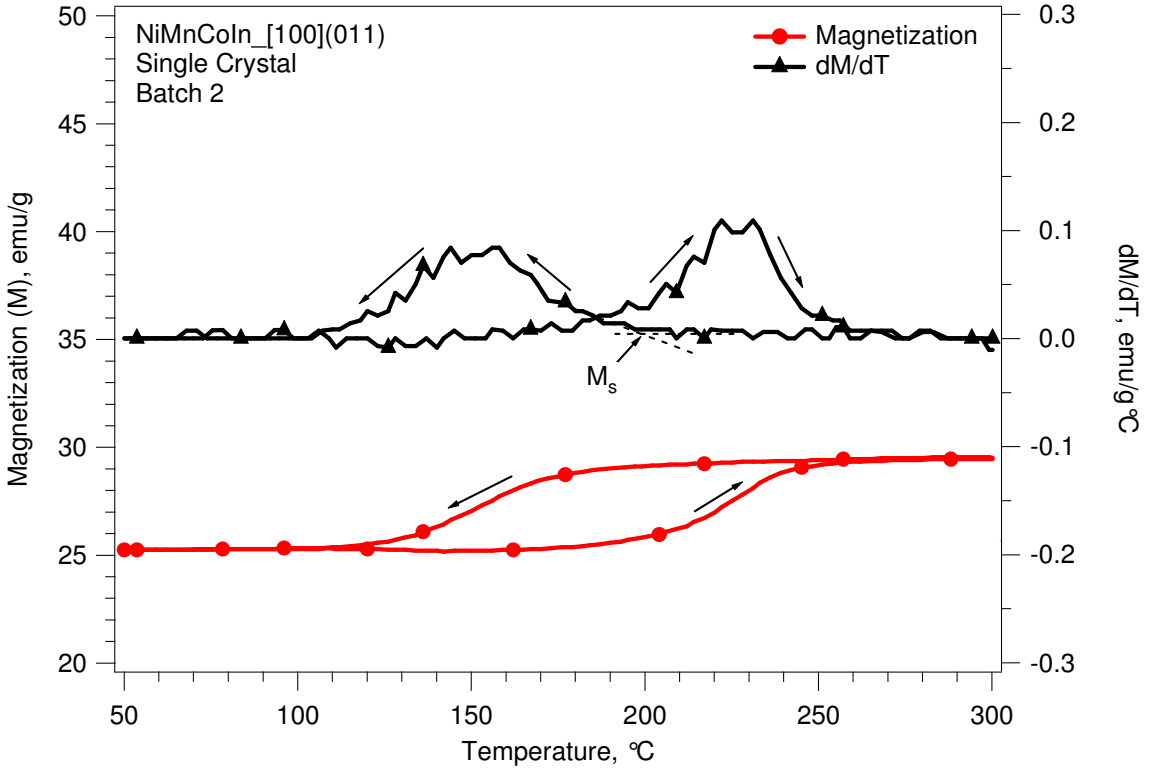

Figure 5.8 Magnetization as a function of temperature under 500 Oe externally applied magnetic field for NiMnCoIn batch 2.

5.5 Thermal Cycling Results

a. NiMnCoIn_[100](110) Batch 1

Thermal cycling tests were performed on the [100](011) specimen from batch 1 at stress levels ranging from 25 MPa to 100 MPa in increments of 25 MPa. The sample was cycled between temperatures ranging from -60°C to 80°C at different stress levels, and compressive strain as a function of temperature was recorded. The thermal cycling results can be seen in Figure 5.9. As can be seen, the transformation temperatures steadily increase with increasing stress. This results in a positive Clausius-Clapeyron slope, which will be presented in a later section. Also, the maximum obtainable transformation strain is 5.91% and, as predicted by the DSC and SQUID results, the transformation is slow and the thermal hysteresis is about 45°C. The transformation strain and thermal hysteresis will be examined in a later section as well.

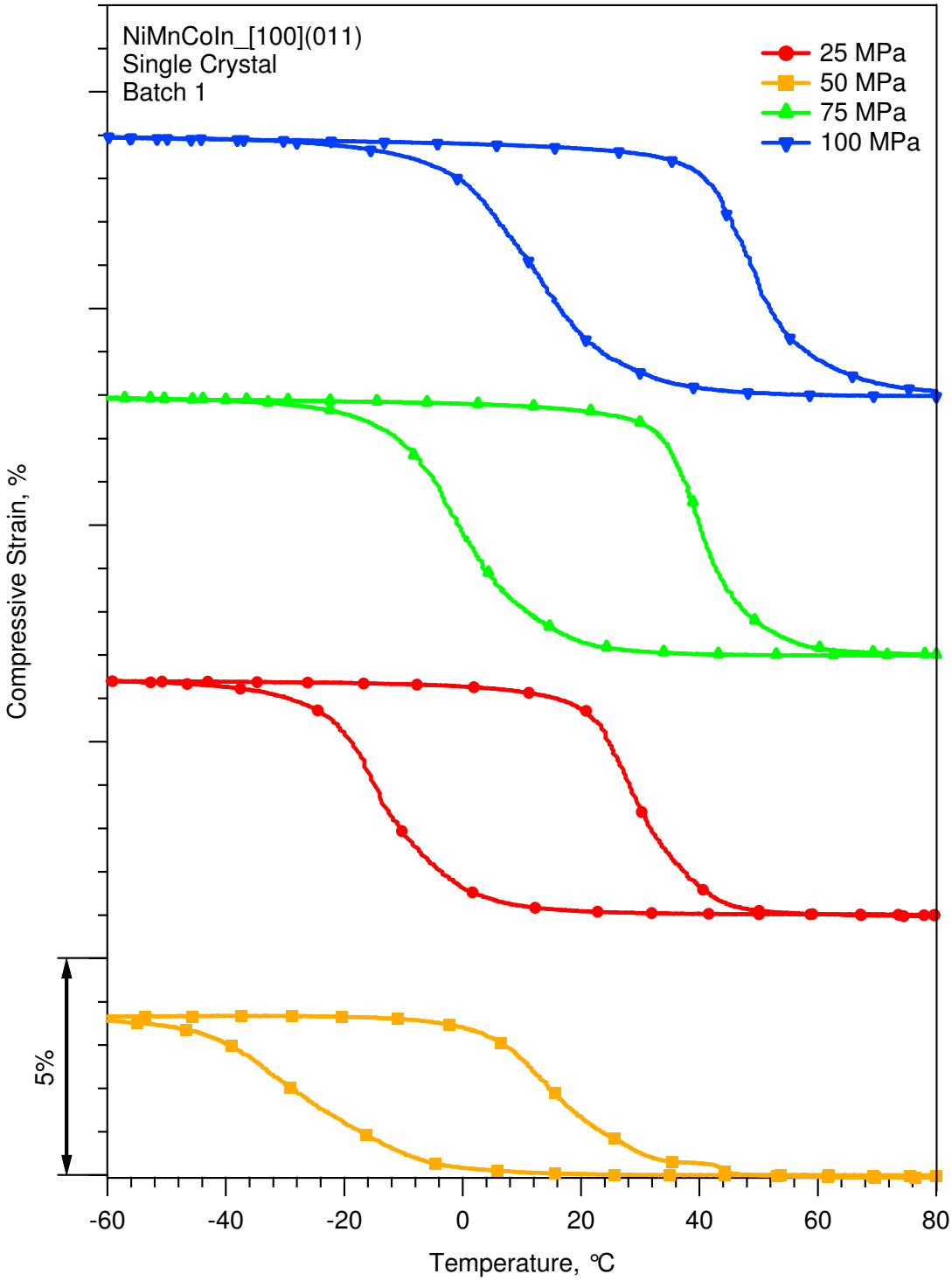

Figure 5.9 Thermal cycling results for NiMnCoIn_[100](011) batch 1 single crystal at different stress levels.

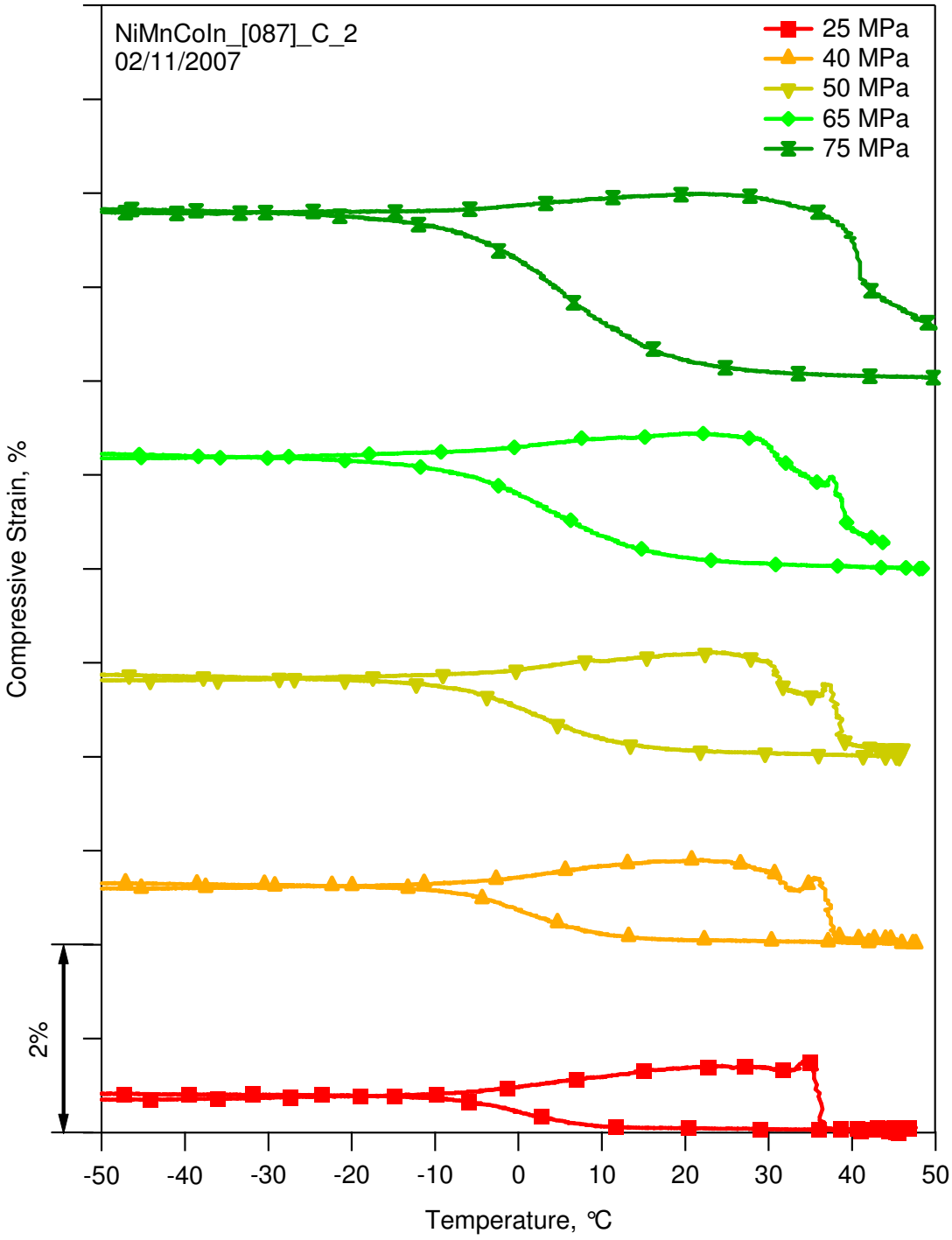

Figure 5.10 Thermal cycling results for NiMnCoIn_[087] batch 1 single crystals under various stress levels.

b. NiMnCoIn_[087] Batch 1

The thermoelastic response from the NiMnCoIn [087] single crystal can be seen in Figure 5.10. Thermal cycling tests were carried out at stress levels ranging from 25 MPa to 75 MPa. The sample temperature was cycled from about -50°C to 50°C. As can be seen from the figure, the transformation temperatures increase with increasing stress. The increase is much less noticeable than that seen in the NiMnCoIn [100](011) single crystals. This represents a steep Clausius-Clapeyron relationship, which will be presented in more detail later. Also, the transformation strain increases steadily with increasing stress levels, meaning that the maximum transformation strain has not yet been reached. The full response from this specimen was not revealed to the extremely brittle nature of this crystal.

c. NiMnCoIn_[25 7 15] Batch 1

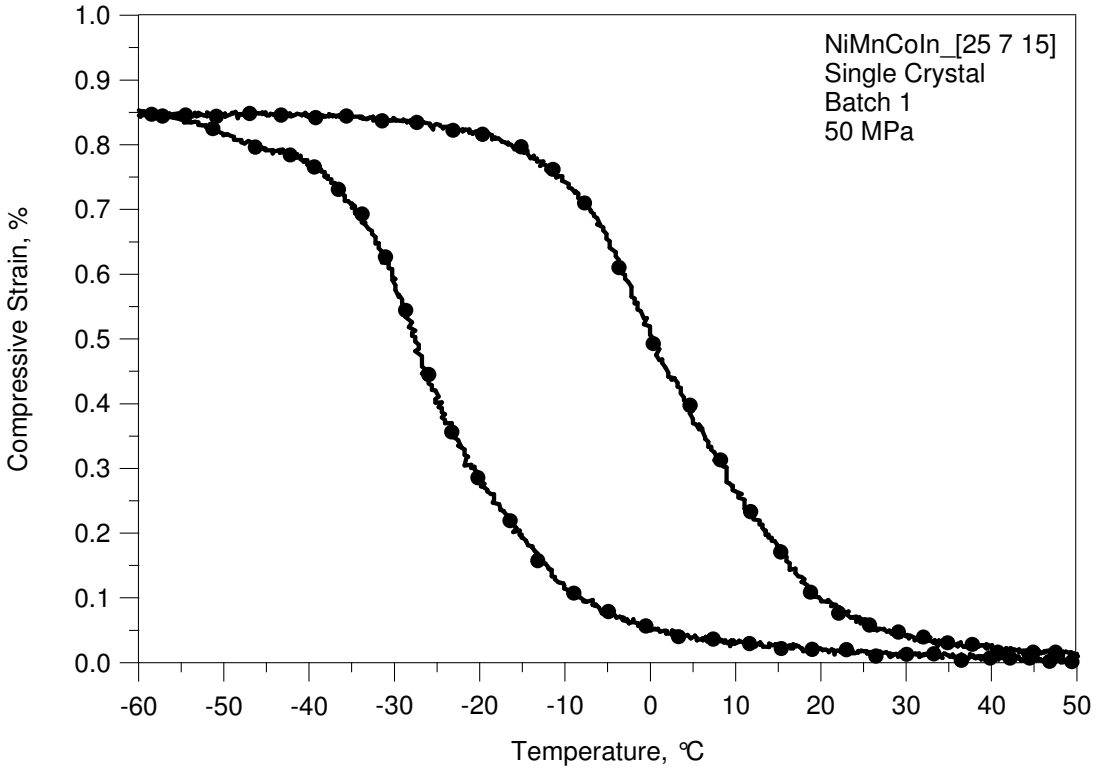

Figure 5.11 Thermal cycling results for NiMnCoIn_[25 7 15] batch 1 single crystal under a compressive stress of 50 MPa.

The thermal cycling results for the NiMnCoIn [25 7 15] batch 1 sample can be found in Figure 5.11. The sample was cycled between -60°C and 50°C, and the compressive strain was recorded as a function of temperature. As shown in the figure, the martensitic transformation takes nearly 40°C to complete and the thermal hysteresis during the transformation is about 30°C. The transformation strain obtained is about 0.85%, however this may not be the maximum obtainable transformation strain as thermal cycling was not conducted at higher stress levels.

d. NiMnCoIn_[100](110) Batch 2

The NiMnCoIn_[100](011) batch 2 specimen was also cycled thermally between temperatures ranging from -120°C to 60°C under different stress levels. Thermal cycling occurred under stress levels of 50 MPa and 75 MPa, and the compressive strain was recorded. The thermal cycling results may be seen in Figure 5.12. As seen, the transformation temperatures increase with increasing stress and the maximum obtainable strain is approximately 5%. Similar to the previously discussed results, the thermal hysteresis during transformation is about 55°C, which agrees with both the DSC and SQUID measurements.

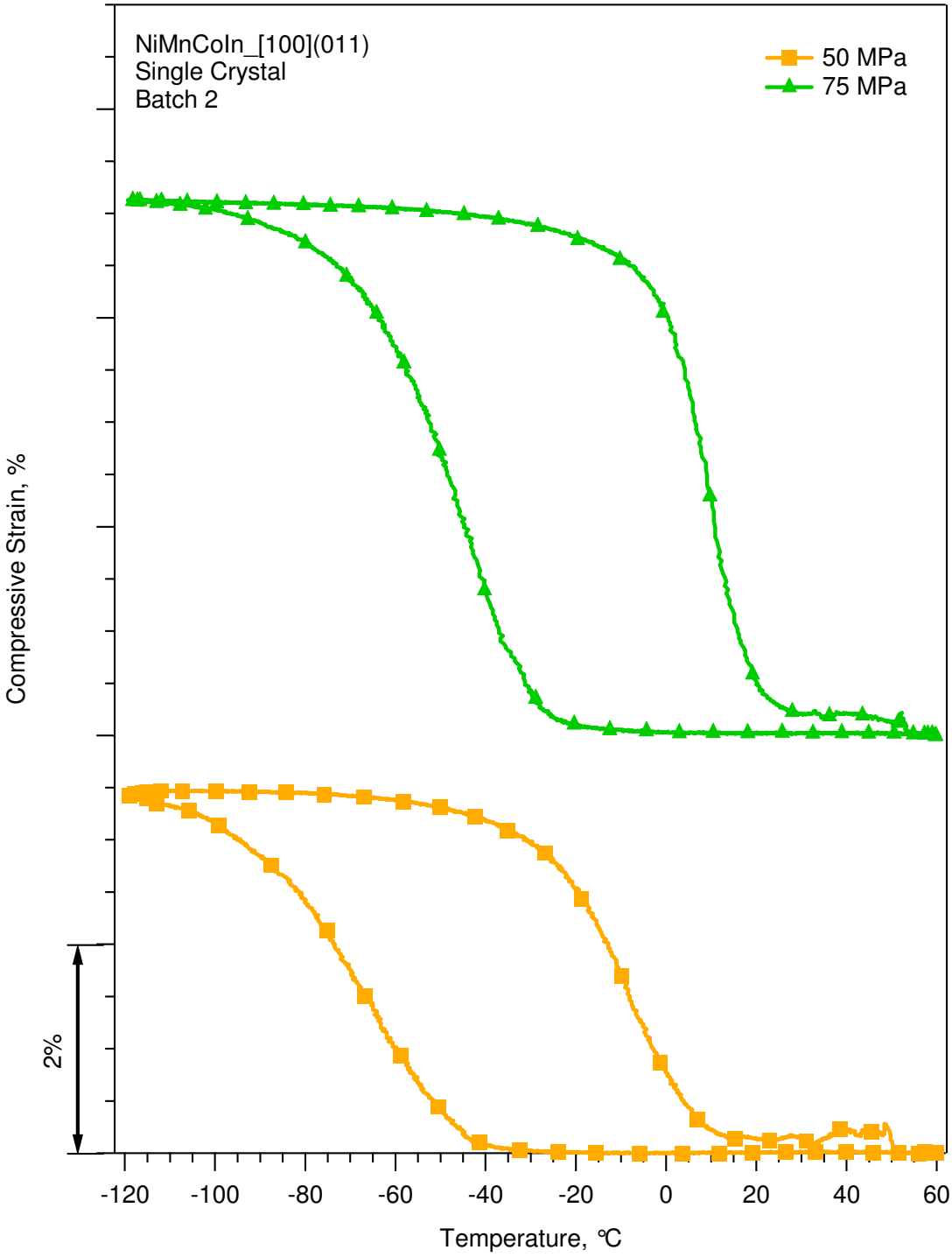

Figure 5.12 Thermal cycling results for NiMnCoIn_[100](011) batch 2 single crystal under different stress levels.

5.6 Pseudoelasticity Results

a. NiMnCoIn_[25 7 15] Batch 1

The pseudoelastic response of the NiMnCoIn_[25 7 15] batch 1 specimen was obtained at different temperatures ranging from 0°C to 100°C in increments of about 25°C. Previously attempted experiments have revealed the brittle nature of this alloy, therefore the pseudoelasticity tests were carried out until 4%. The pseudoelastic behavior of this sample may be seen in Figure 5.13. As illustrated, the critical stress for phase transformation increases with increasing temperature. However, the pseudoelastic response at 100°C shows a decrease in critical stress, which has been attributed to specimen failure. As the pseudoelastic experiments did not explore the full phase transformation, the maximum obtainable transformation strain and stress hysteresis are not available.

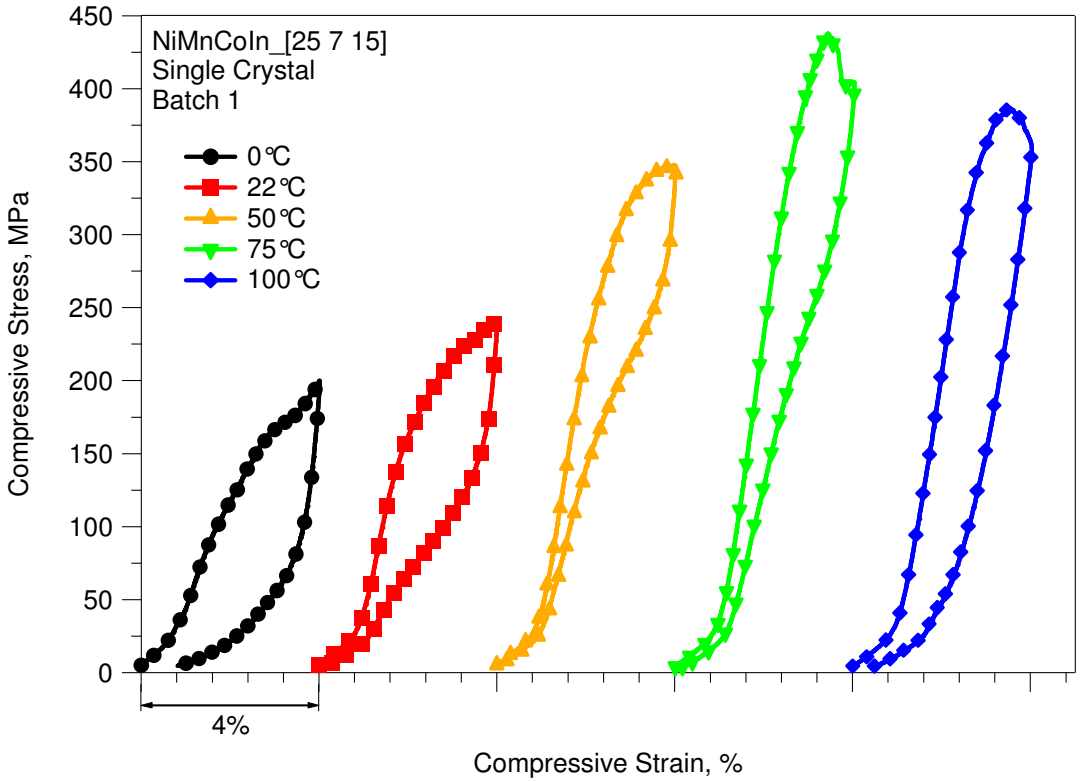

Figure 5.13 Pseudoelastic response for the NiMnCoIn_[25 7 15] batch 1 single crystal at different temperatures.

b. NiMnCoIn_[100](110) Batch 2

Pseudoelasticity tests were conducted on the NiMnCoIn_[100](011) batch 2 specimen at different temperatures. The sample was tested at 0°C, 20°C, and 50°C, and the results may be seen in Figure 5.14. As demonstrated, the critical stress for transformation increases with increasing temperature. The pseudoelastic response details the complete phase transformation and the maximum transformation strain obtained was 6.49%. The stress hysteresis is approximately 100 MPa and seems to increase with temperature. The sample failed at 50°C, which is why the pseudoelastic response does not show the complete transformation plateau.

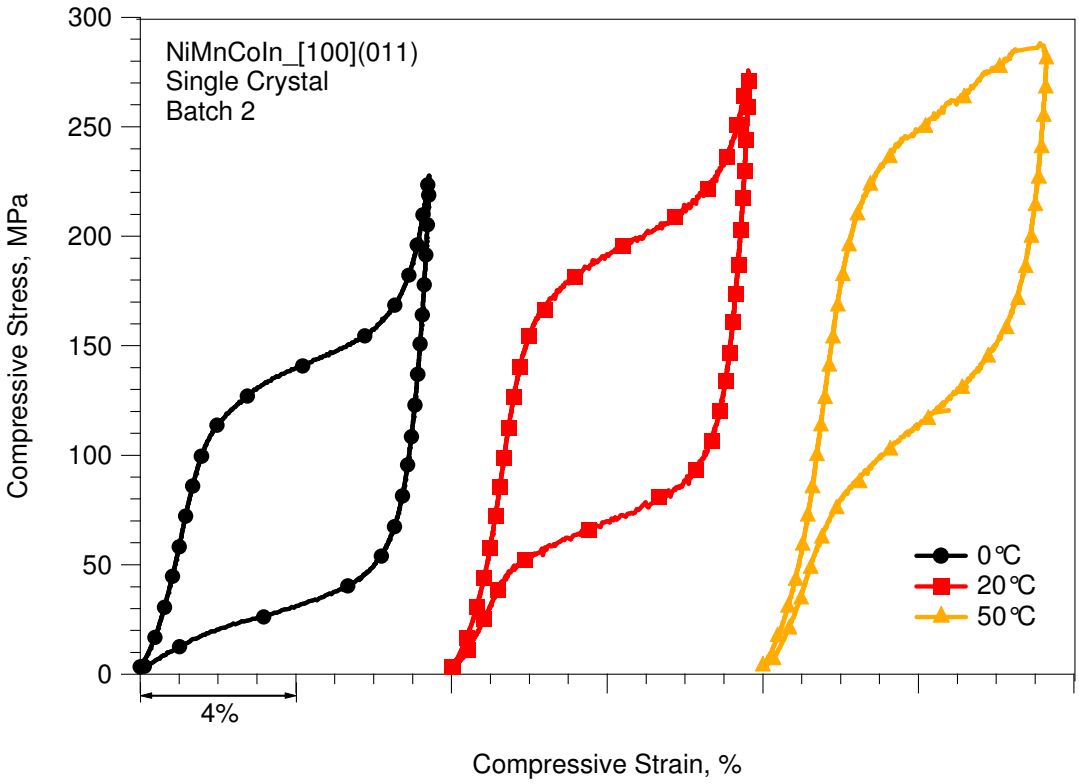

Figure 5.14 Pseudoelastic response for the NiMnCoIn_[100](011) batch 2 single crystal at different temperatures.

5.7 Clausius-Clapeyron Relationship

The previously discussed results: DSC, SQUID, thermal cycling, and pseudoelasticity, have been analyzed to determine the martensite start temperatures as a function of applied compressive stress. The DSC and SQUID measurements were used to determine the transformation temperatures under zero load, while thermal cycling and pseudoelasticity were used to observe the shift in martensite start temperature with increasing stress levels. The sum of this data was compiled and used to construct a stress-temperature phase diagram for the NiMnCoIn single crystal system. The resulting stress-temperature phase diagram may be seen in Figure 5.15.

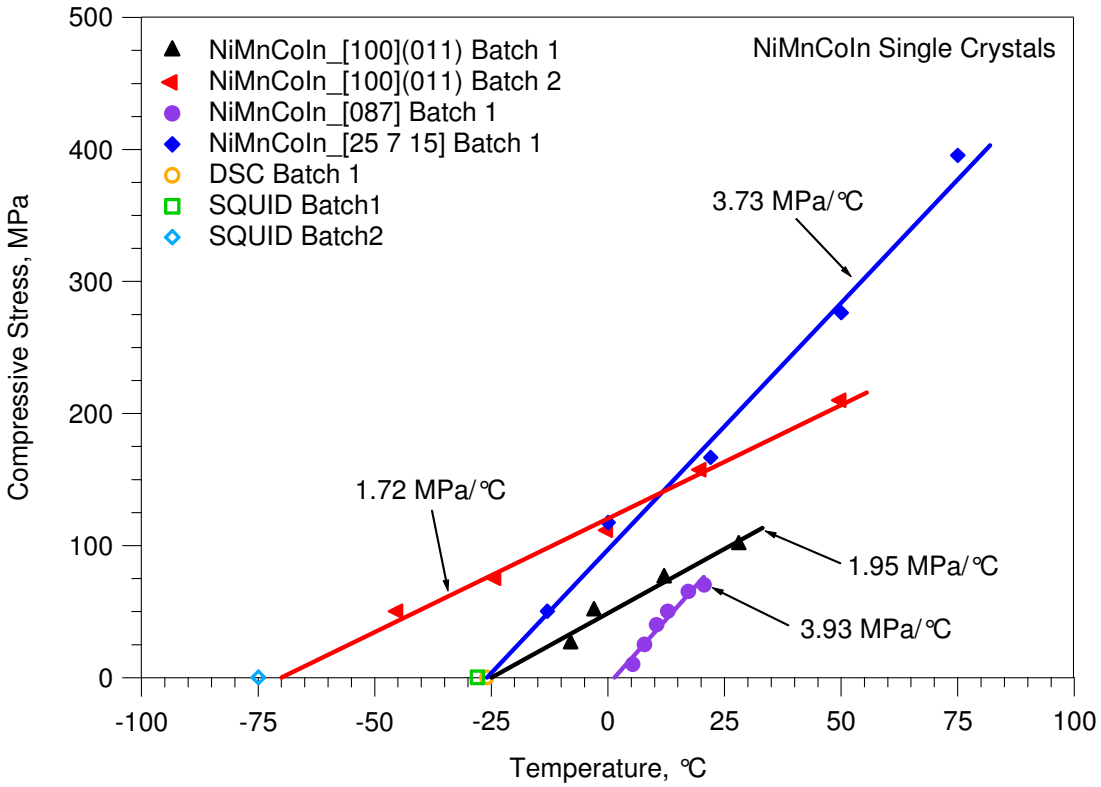

Figure 5.15 NiMnCoIn stress-temperature phase diagram illustrating the Clausius-Clapeyron relationship for the different crystallographic orientations of both batches 1 and 2.

As can be seen, the phase diagram shows that the martensite start temperature for NiMnCoIn batch 1 is approximately -26°C, which is in good agreement with both the DSC and SQUID measurements. On the other hand, the martensite start temperature for NiMnCoIn batch 2 is about -70°C, which is also in good agreement with the DSC and SQUID results. The Clausius-Clapeyron slope of batch 2 is slightly lower than that for batch 1, which may be attributed to the different compositional makeup between the two batches.

5.8 Transformation Strain

Using the thermal cycling and pseudoelasticity results, the maximum transformation strain as functions of applied compressive stress and temperature was empirically deduced, and can be seen in Figure 5.16. The maximum transformation strain for [100](011) batch 1 was observed during thermal cycling experiments and determined to be about 5.91%. The heating cooling results for the [100](011) batch 2 sample to not exhibit maximum transformation strain. The transformation strain from the [087] sample gradually increased, however due to the inherent brittleness of the specimen the maximum transformation strain was not observed. Since the trend for the [087] specimen is increasing, the maximum transformation strain is expected to be more than shown in Figure 5.16. Likewise, the [25 7 15] batch 1 sample was very brittle and only about 0.85% transformation strain was observed under 50 MPa compressive stress. However according to the theoretical transformation strains previously calculated more transformation strain is expected at higher stress levels.

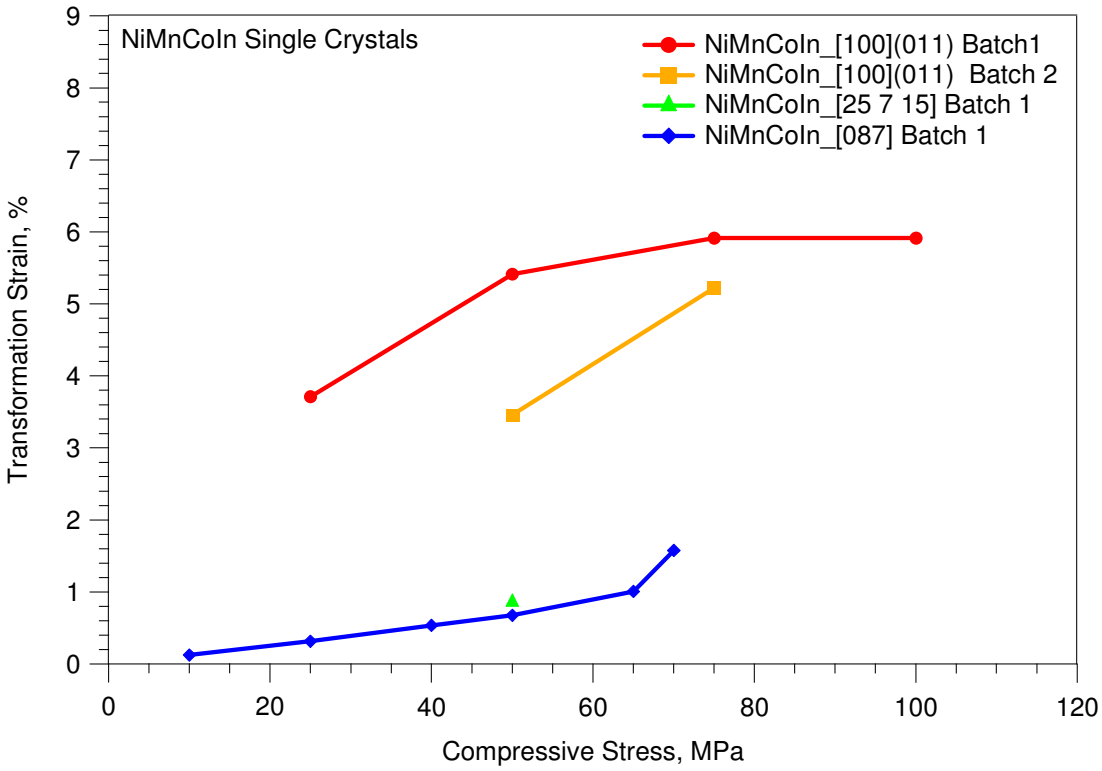

Figure 5.16 Transformation strain, for different crystallographic orientations and batches, as a function of applied compressive stress in NiMnCoIn single crystals.

The transformation strain for the [100](011) batch 2 sample was determined using the pseudoelastic response, and can be seen in Figure 5.17. The [100](011) batch 2 specimen is capable of exhibiting nearly 6.5% transformation strain, which is slightly higher than predicted by the energy minimization method. On the other hand, the Clausius-Clapeyron slope for the [100](011) batch 2 specimen was slightly lower than that for batch 1, which exhibited about 5.9% transformation strain. As will be shown in the subsequent section, the resulting entropies of transformation for these two batches are very similar despite the differences in Clausius-Clapeyron slopes and transformation strains.

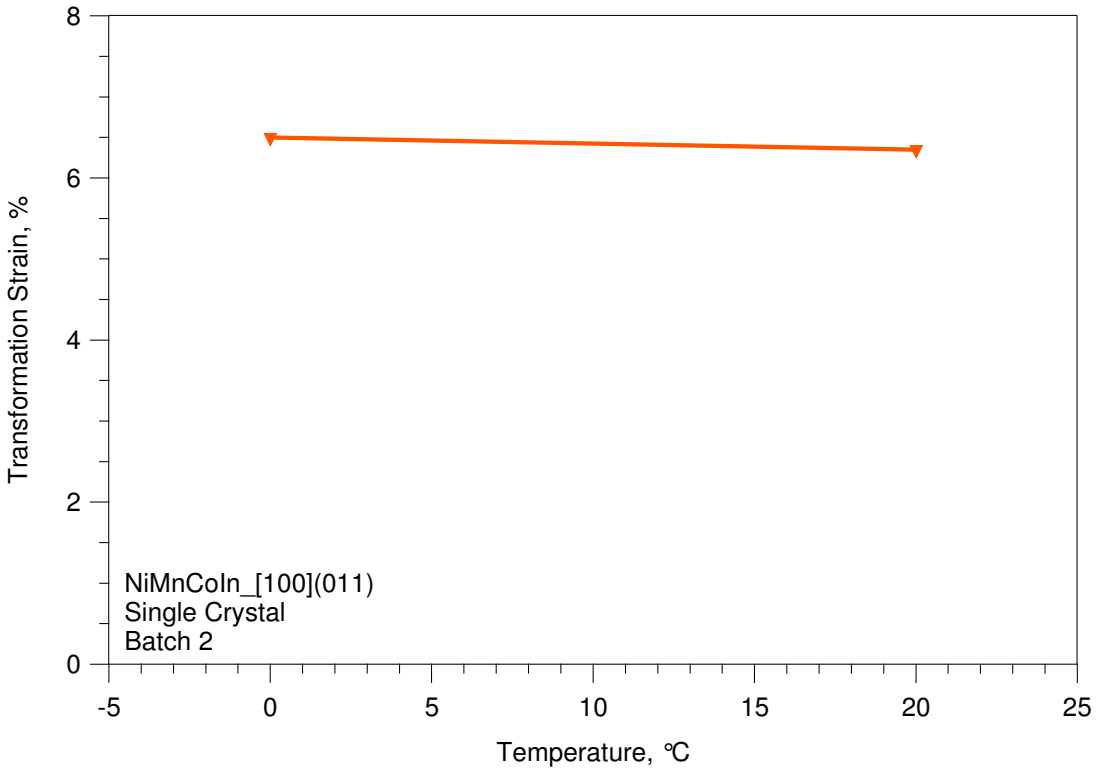

Figure 5.17 Transformation strain as a function of temperature for the [100](011) batch 2 specimen as determined from the pseudoelastic responses at 0°C and 20°C.

5.9 Entropy of Transformation

Using the Clausius-Clapeyron equation (equation 9), the entropy of transformation may be estimated for the NiMnCoIn single crystals. Recall from equation 9, the change in stress over the change in temperature (a.k.a. Clausius-Clapeyron slope) is directly proportional to the entropy of transformation over the maximum transformation strain. Therefore, using the experimentally determined Clausius-Clapeyron slopes and theoretical transformation strains, one can empirically calculate the entropy of transformation. The empirically determined entropy of transformation may be found in Table 5.2. As can be seen, the entropies for the [100](011) batch 1, [100](011) batch 2, and [087] batch 1 single crystal samples are very similar. Despite the slightly higher transformation entropy for the [25 7 15] batch 1 sample, it is still fairly close to those predicted for the other crystallographic

orientations. It can be said that the entropy of transformation for this composition of NiMnCoIn is approximately 11.92 MPa/°C.

Table 5.2 Summary of Clausius-Clapeyron slopes, theoretical transformation strains, and estimations of transformation entropy for each crystallographic orientation and batch.

Orientation	Batch	Clausius-Clapeyron Slope (MPa/°C)	Transformation Strain (%)	Entropy of Transformation (MPa/°C)
[100](011)	1	1.95	5.81	11.33
[100](011)	2	1.72	6.49	11.16
[087]	1	3.93	2.87	11.28
[25 7 15]	1	3.73	3.68	13.73

5.10 Thermal and Stress Hysteresis

The thermal cycling results were analyzed in order to determine the thermal hysteresis during transformation for each crystal. Thermal hysteresis as a function of applied compressive stress is shown in Figure 5.18. The thermal hysteresis exhibited in the batch 1 samples was lower than that from batch 2, which is beneficial when attempting to separate the thermomagnetization curves with an externally applied magnetic field. If the thermal hysteresis is small, then less magnetic field is required to separate the curves, which leads to MFIPT. Batch 1 exhibited between 30°C and 45°C, depending upon the crystallographic orientation, and batch 2 demonstrated about 60°C thermal hysteresis.

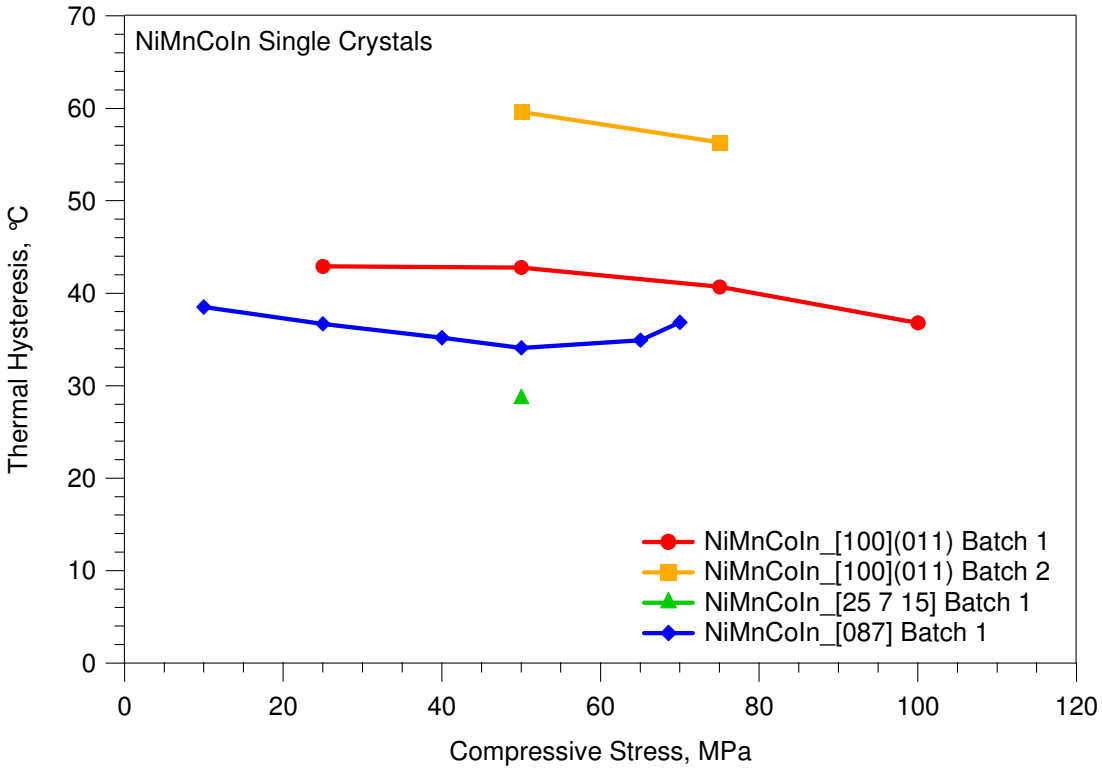

Figure 5.18 Thermal hysteresis, for different crystallographic orientations and batches, as a function of applied compressive stress in NiMnCoIn single crystals.

The stress hysteresis during transformation in the NiMnCoIn [100](011) batch 2 single crystal was deduced from the pseudoelasticity results. Stress hysteresis versus temperature may be seen in Figure 5.19. As shown, the stress hysteresis during transformation is about 134 MPa. Similar to thermal hysteresis, smaller stress hysteresis during transformation will reduce the additional driving force needed to separate the pseudoelastic loops, resulting in MFIPT.

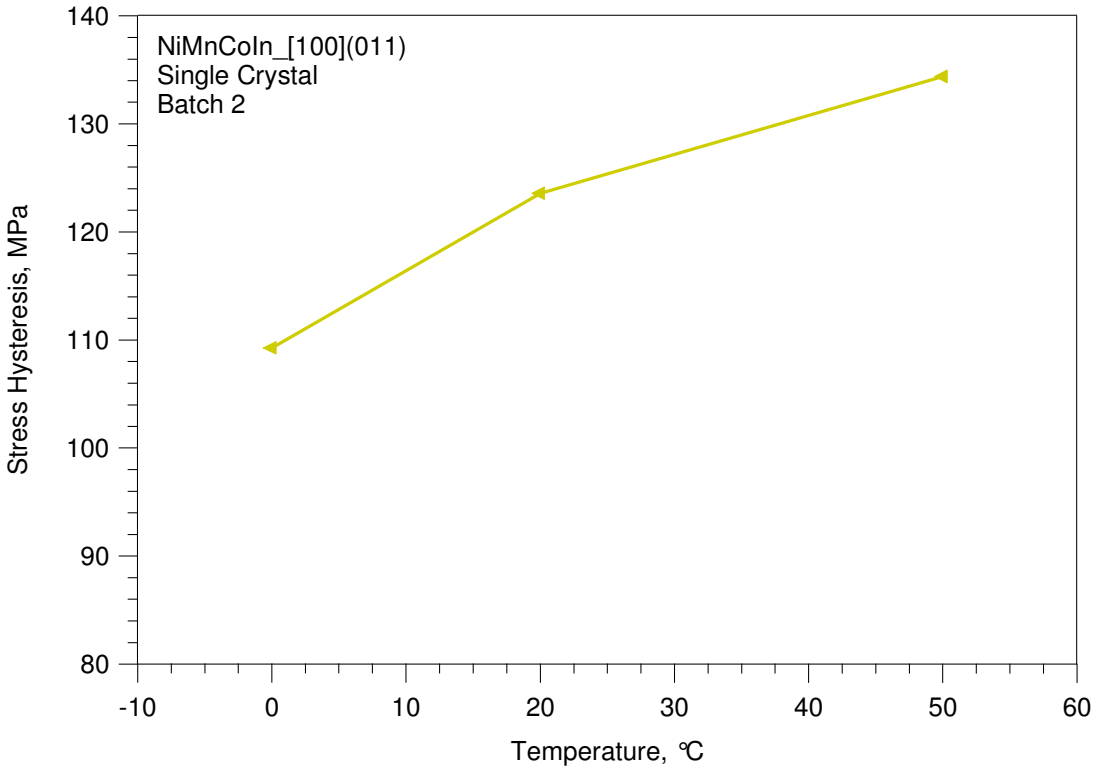

Figure 5.19 Stress hysteresis, for the NiMnCoIn_[100](011) batch 2 single crystal as a function of temperature.

5.11 Magnetostress in NiMnCoIn

In order to better understand the behavior of NiMnCoIn under the application of an external magnetic field, pseudoelastic tests were conducted at different magnetic field magnitudes. Pseudoelasicity was observed in NiMnCoIn [100](011) batch 2 single crystal at magnetic field magnitudes ranging from 0T to 1.6T in increments of 0.4T. The results may be seen in Figure 5.20. As can be seen, the NiMnCoIn single crystal exhibited an increase in the critical stress required for phase transformation with increasing magnetic field magnitudes. This increase in critical stress for phase transformation is known as the magnetostress.

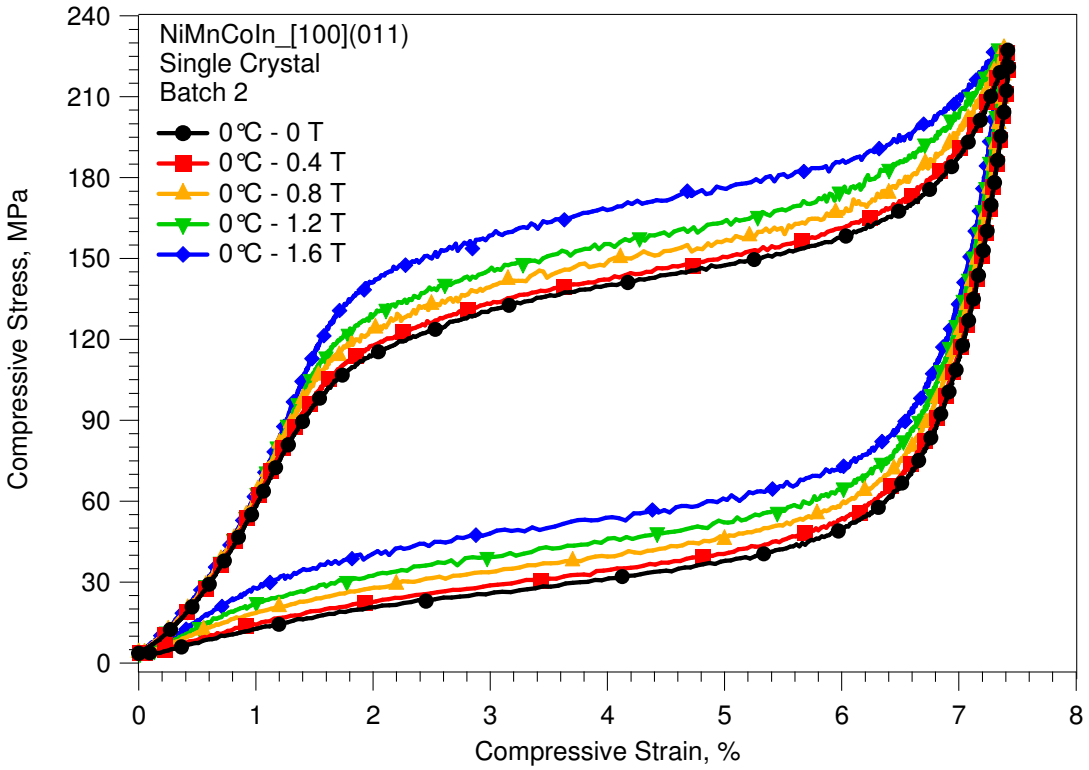

Figure 5.20 Pseudoelasticity at different magnetic field magnitudes for the NiMnCoIn [100](011) batch 2 single crystal.

The magnetostress as a function of the externally applied magnetic field may be seen in Figure 5.21. Under 1.6T, the magnetostress is approximately 30 MPa, however the deviation from the linear trend may be attributed to the first cycle effect typically seen in SMAs. Assuming a linear trend, as shown by the dashed line, the magnetostress under a 1.6T magnetic field is expected to be about 20 MPa, which is much larger than that shown in other MSMAs. For instance, the magnetostress previously exhibited in Ni_2MnGa single crystals [23, 24] for reversible MFIPT was approximately 7 MPa. The large magnetostress observed under 1.6T magnetic field results in increased actuation stress levels and identifies NiMnCoIn as a legitimate MSMA.

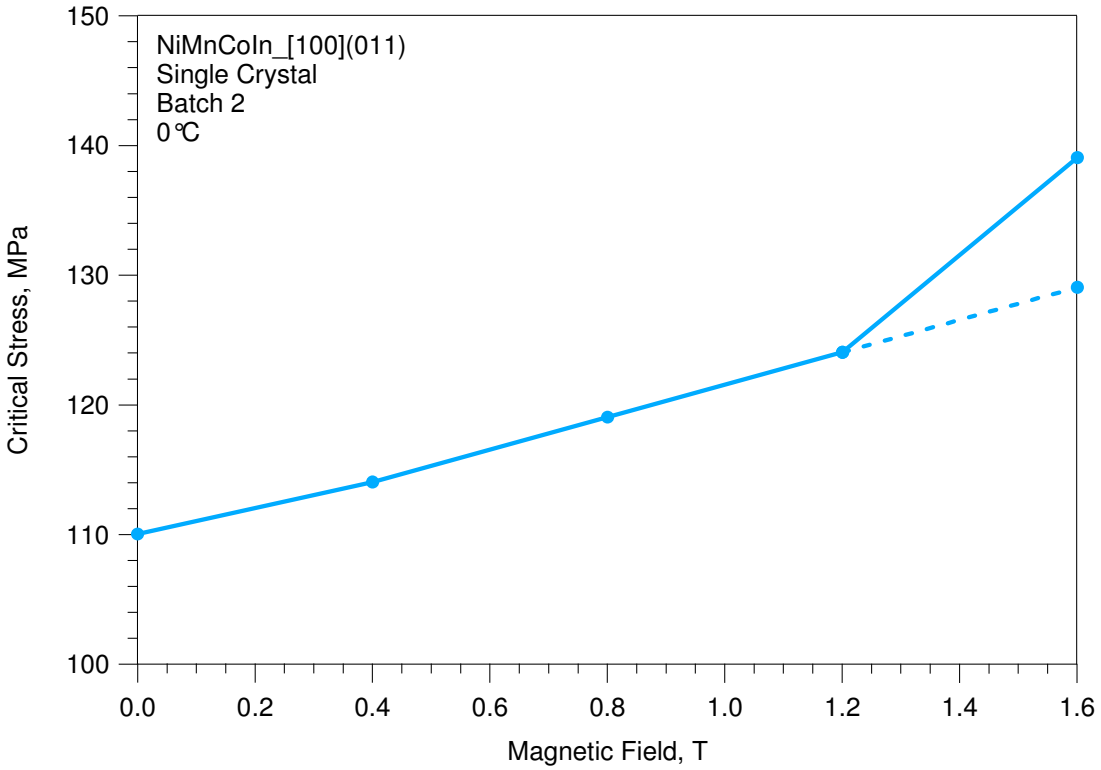

Figure 5.21 Critical stress for phase transformation under different magnetic fields for NiMnCoIn [100](011) batch 2 sample. The sample exhibits ~20 MPa magnetostress under 1.6T magnetic field.

5.12 Optical Microscopy Results

Previous experiments have shown that this composition is extremely brittle and it has been theorized that the second phase may either be the cause of the brittleness or increase the ductility. Optical microscopy was performed on the NiMnCoIn [100](011) batch 1 single crystal specimen after testing. The sample was mechanically polished and examined for the existence of second phase. A micrograph of the [100](011) batch 1 sample under 5x magnification may be seen in Figure 5.22. As can be seen, the sample contains several precipitates that are fairly uniform in size, yet they are not evenly distributed. The sample shown in Figure 5.22 seemed to be fairly ductile during testing, and multiple sets of repeatable data were recorded. Therefore, the second phase seems to increase the ductility of this alloy.

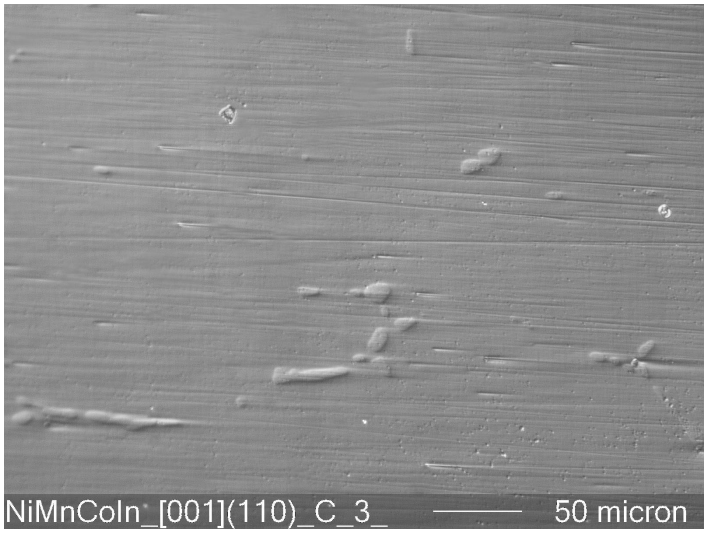

Figure 5.22 Optical microscopy (5x) of the NiMnCoIn [100](011) batch 1 single crystal, showing that several precipitates exist in the matrix.

Similarly, the [100](011) batch 2 sample was examined under the microscope and a macroscopic view of the sample surface at 5x magnification can be seen in Figure 5.23.

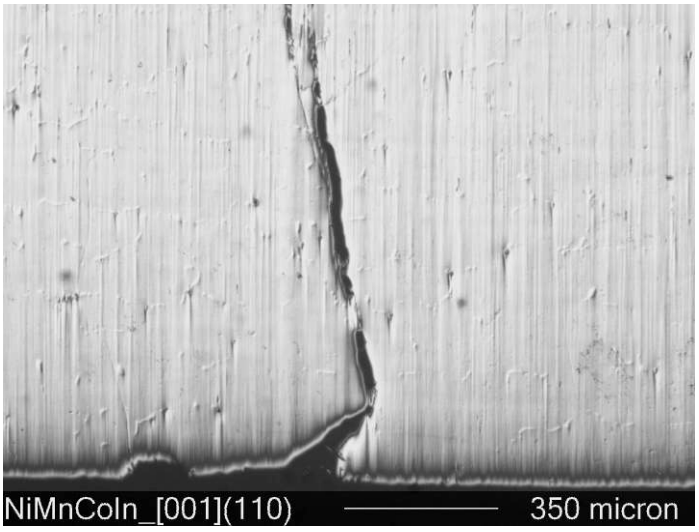

Figure 5.23 Optical microscopy (5x) of the NiMnCoIn [100](011) batch 2 single crystal, showing that several precipitates exist in the matrix.

As can be seen, small precipitates uniformly exist in the matrix. Upon inspection, the only interaction between the second phase and the fracture occurs at the top of Figure 5.23. It seems that the second phase may have altered the fracture path, implying that the second phase is more ductile than the matrix.

A close-up view of the second phase may be seen in Figure 5.24. The small craters on the surface of the sample were caused by the 0.05μm alumina powder.

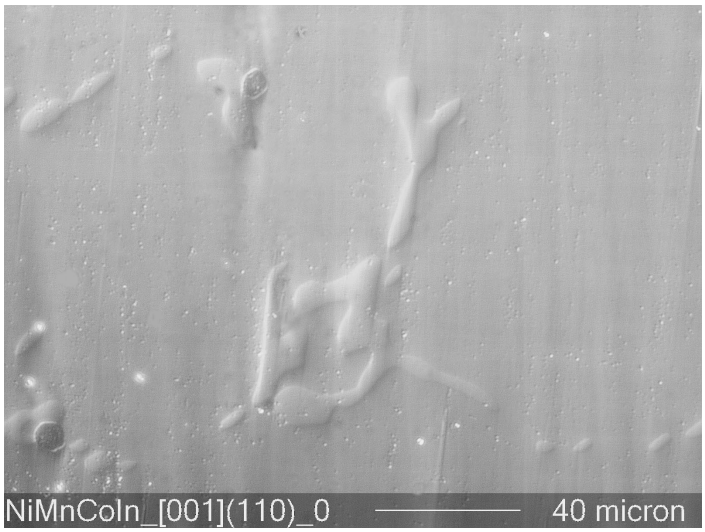

Figure 5.24 Close-up view (20x) of second phase in the NiMnCoIn [100](011) batch 2 single crystal.

The second phase, shown in Figure 5.24, was located at the top of the specimen, which was opposite of the fracture. The precipitates at the top of the specimen were similar in size compared to those at the bottom, however they were not uniformly distributed.

Optical microscopy was also performed on the [087] and [25 7 15] orientations from batch 1. The micrographs taken during inspection may be seen in Figures 5.25 and 5.26. Figure 5.25 shows the surface of the [25 7 15] batch 1 sample. Upon examination, the matrix does not contain second phase as seen in the [100](011) specimens. The

brittle nature of the [25 7 15] batch 1 sample may be attributed to the lack of second phase.

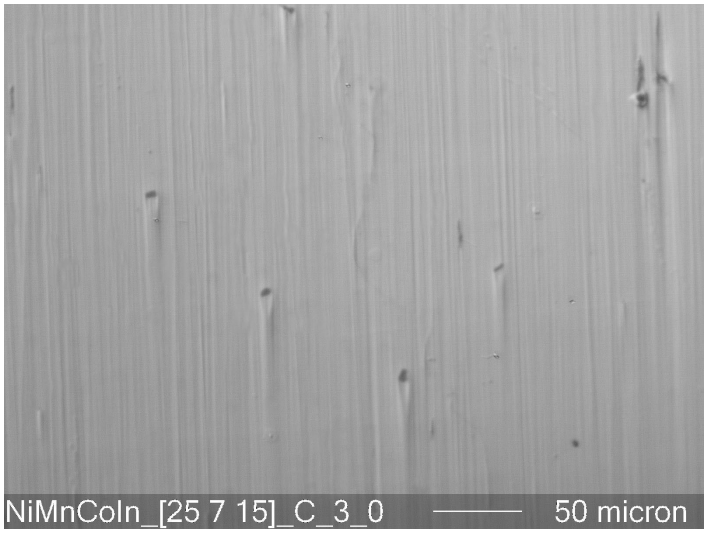

Figure 5.25 Optical microscopy (5x) of the NiMnCoIn [25 7 15] batch 1 single crystal, showing a clean surface without the presence of precipitates.

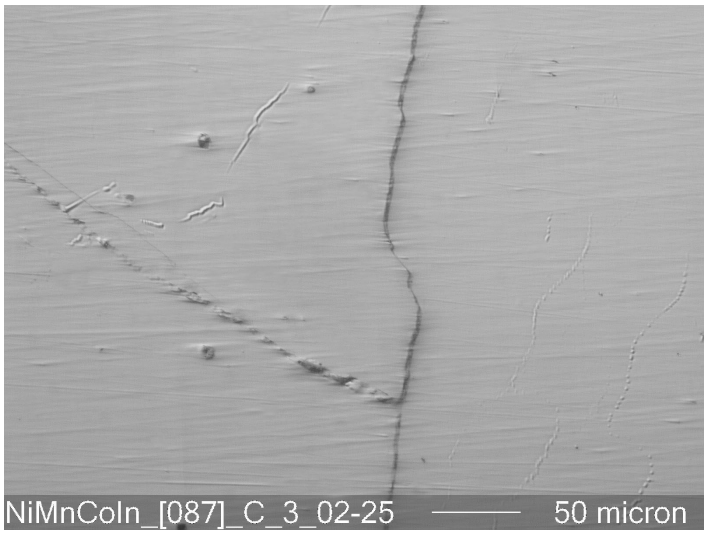

Figure 5.26 Optical microscopy (5x) of the NiMnCoIn [087] batch 1 single crystal, showing a fractured surface without the presence of precipitates.

The surface of the [087] batch 1 sample may be seen in figure 5.26. Upon examination, it was revealed that the [087] sample contained no second phase, however there several small surface cracks. The lack of second phase and the presence of the surface cracks explain the difficulties in experimentation and the brittle nature of the alloy.

The [100](011) orientations from both batches were fairly ductile during testing, and contained an unevenly distributed amount of second phase in the matrix. On the other hand, the [25 7 15] and [087] batch 1 samples were very brittle and, upon inspection, revealed several small surface cracks in a clean (no precipitates) matrix.

CHAPTER VI

CONCLUSIONS AND FUTURE RECOMMENDATIONS

6.1 Conclusions

In this study, the shape memory response of Ni_2MnGa and NiMnCoIn magnetic shape memory alloys under compression was investigated. Ni_2MnGa was subjected to thermal cycling and pseudoelasticity tests in order to determine the transformation behavior and the corresponding transformation temperatures for the many martensitic phase transformations. It was also shown that Ni_2MnGa exhibits a phase transformation to a recently discovered phase [22-24], termed the X-phase, which only exists under an externally applied load. The resulting stress-temperature phase diagram explicitly identifies the stress and temperature ranges where the I $\leftrightarrow$ X phase transformation may be found, which has been previously shown to exhibit MFIPT [23, 24]. This phase diagram also illustrates the region where the X-phase is expected to exist. This information will aid in future investigations including the determination of the unique crystal structure of the X-phase.

NiMnCoIn is a new meta-magnetic shape memory alloy that has unique magnetic properties that imply a strong candidacy for MFIPT. In order to better understand this new alloy's abilities, the shape memory response was revealed using thermal cycling and pseudoelasticity experiments. Using the data recorded during experimentation, a stress-temperature phase diagram showing the orientation dependence on the Clausius-Clapeyron relationships was created. The thermal and stress hysteresis during the phase transformation, as well as the transformation strain, were used to analyze the potential for MFIPT. The samples tested revealed large thermal hysteresis (40°C to 60°C) and large stress hysteresis (110 MPa to 135 MPa). Using the SQUID measurements, it was determined that the martensite start temperature for batch 1 samples shifts -9.25°C for every 1T of externally applied magnetic field. Based on the Clausius-Clapeyron slopes, for every 1T of externally applied magnetic field the resulting magnetostress is expected to be about 18 MPa for the [100](011) orientation, 32 MPa for the [25 7 15] orientation, and 36 MPa for the [087] orientation. For batch 2, the effect of magnetic field on the

critical stress for phase transformation was determined by examining the pseudoelastic response under different magnetic fields. It was experimentally determined that batch two exhibits a magnetostress of about 11 MPa for every 1T of externally applied magnetic field. The exhibition of large magnetostresses under fairly low magnetic fields results in a large increase in actuation stress levels. During experimentation, the brittle nature of this alloy was observed. Based upon the optical microscopy results, the second phase only exists in the [100](011) samples, which seemed to be much more ductile than the [25 7 15] and [087] samples during testing. Therefore, the presence of the second phase seems increase the ductility of the NiMnCoIn alloy system. In conclusion, the shape memory response has been established for different crystallographic orientations and the magnetic response has been demonstrated. However, this material still remains very brittle and any potential applications are therefore limited.

Ni_2MnGa is a MSMA that has ferromagnetic parent and martensite phases. Therefore, the main mechanism behind MFIS in Ni_2MnGa is magnetic field induced variant reorientation, which operates primarily on the MAE energy difference between the parent and martensite phases. However, Ni_2MnGa has previously been shown to exhibit fully reversible stress induced MFIPT in the I $\leftrightarrow$ X phase transformation due to a magnetostress of ~7 MPa and a small stress hysteresis. On the other hand, NiMnCoIn is a meta-magnetic SMA, meaning that the parent phase is ferromagnetic and the martensite phase is paramagnetic. Therefore, the MAE contribution is small, but the Zeeman energy contribution may be exploited. With increasing magnetic field, the available Zeeman energy contribution increases and the maximum actuation stress, or blocking stress, increases. Based on the results of the current study, the increased contribution from the Zeeman energy is responsible for a large magnetostress of about 29 MPa (under 1.6T magnetic field), which is more than four times that reported in Ni_2MnGa. Therefore, the maximum obtainable actuation stress is limited only by the available magnetic field. Despite the promising magnetic response of NiMnCoIn, the large thermal and stress hysteresis exhibited during phase transformation limit the possible applications by increasing the field requirement for MFIPT. In conclusion, it

has been revealed that NiMnCoIn is a strong candidate for several mechanical applications such as actuation, sensing, and power generation and additional studies focused on increasing ductility and magnetostress, and reducing thermal and stress hysteresis are recommended.

6.2 Future Recommendations

1) Conduct thermal cycling tests are higher stress levels to complete the parent to X-phase transformation curve.
2) Using micro-tensile stage, perform x-ray diffraction analysis on Ni_2MnGa under external stresses in order to determine crystal structure of X-phase.
3) Perform inductively coupled plasma-atomic emission spectrometry (ICP-AES) on NiMnCoIn batch 1 and batch 2 to determine the compositional makeup.
4) Perform nano-indentation tests to establish hardness of second phase and matrix to determine whether second phase increases or decreases ductility.
5) Conduct a heat treatment study to determine the best way to increase ductility by increasing/decreasing the second phase.
6) Conduct a heat treatment study in order to determine how to reduce thermal and stress hysteresis during transformation.
7) Perform composition study in order to observe the effect of composition on mechanical and magnetic properties.

REFERENCES

1. Funakubo H. Shape Memory Alloys, Gordon & Breach Publishing Group, Amsterdam 1987.
2. Otsuka K, Wayman CM. Shape Memory Materials, Cambridge University Press, Cambridge 1998.
3. Liu Y, Liu Y, Humbeeck JV. Acta Mater 1999;47:199.
4. Shaw JA, Kyriakides S. J Mech Phys Solids 1995;43:1243.
5. Kulkarni AV. M.S. Thesis. Texas A&M University. 2004.
6. Sehitoglu H, Karaman I, Anderson R, Zhang X, Gall K, Maier HJ, Chumlyakov Y. Acta Mater 2000;48:3311.
7. Kiefer B, Lagoudas DC. Philos Mag 2005;85:4289.
8. O'Handley RC. Modern Magnetic Materials: Principles and Applications, John Wiley and Sons, New York, 2000.
9. Heczko O. J Magn and Magn Mater 2005;290:787.
10. Jeong S, Inoue K, Inoue S, Koterazawa K, Taya M. Mater Sci Eng A 2003;359:253.
11. Karaca HE, Karaman I, Basaran B, Chumlyakov YI, Maier HC. Acta Mater 2006;54:233.
12. Sosinov A, Likhachev AA, Lanska N, Ullakko K. Appl Phys Lett 2002;80:1746.
13. James RD, Wuttig M. Philos Mag A 1998;77:1273.
14. Ullakko K, Huang JK, Kantner C, O'Handley RC, Kokorin VV. Appl Phys Lett 1996;69:1966.
15. Marioni MA, O'Handley RC, Allen SM, Hall SR, Paul DI, Richard ML, Feuchtwanger J, Peterson BW, Chambers JM and Techapiesancharoenkij R, J Magn and Magn Mater 2005;290:35.
16. Müllner P, Chernenko VA, Kostorz G. J Magn Magn Mater 2003;267:325.
17. Takeuchi I, Famodu OO, Read JC, Aronova MA, Chang KS, Craciunescu C, Lofland SE, Wuttig M, Wellstood F, Knauss L, Orozco A. Nature Materials 2003;2:180.
18. Murray SJ, Marioni MA, Kukla AM, Robinson J, O'Handley RC, Allen SM, J Appl Phys 2000;87:5774.

19. O'Handley RC. J Appl Phys 1998;83:886.
20. Murray SJ, Marioni M, Allen SM, O'Handley RC, Lograsso TA. Appl Phys Lett 2000;77:886.
21. Chernenko VA, Pons J, Cesari E, Ishikawa K. Acta Mater 2005;53:5071.
22. Chernenko VA, Kokorin VV, Babii OM, Zasimchuk IK. Intermetallics 1998;6:29.
23. Gonzalez-Comas A, Obrado E, Manosa L, Planes A, Chernenko VA, Hattink BJ, Labarta A. Phys Rev B 1999;60(10):7085.
24. Khovailo VV, Takagi T, Bozhko AD, Matsumoto M, Tani J, Shavrov VG. J Phys Condens Matter 2001;13:9655.
25. Chernenko VA, Segui C, Cesari E, Pons J, Kokorin VV. Phys Rev B 1998;57(5):2659.
26. Zheludev A, Shapiro SM. Solid State Commun 1996;98(1):35.
27. Kim JH, Fukuda T, Kakeshita T. Scripta Mater 2006;54:585.
28. Karaca HE, Karaman I, Basaran B, Lagoudas DC, Chumlyakov YI, Maier HJ. Scripta Mater 2006;55(9):803.
29. Karaman I, Karaca HE, Basaran B, Lagoudas DC, Chumlyakov YI, Maier HJ. Scripta Mater 2006;55(4):403.
30. Straka L, Heczko O, Lanska N. IEEE Trans Magn 2002;38(5):2835.
31. Vasil'ev AN, Bozhko AD, Khovailo VV, Dikshtein IE, Shavrov VG, Buchelnikov VD, Matsumoto M, Suzuki S, Takagi T, Tani J. Phys Rev B 1999;59(2):1113.
32. Pons J, Chernenko VA, Santamarta R, Cesari E. Acta Mater 2000;48:3027.
33. Wedel B, Suzuki M, Murakami Y, Wedel C, Suzuki T, Shindo D, Itagaki K. J Alloy Compd 1999;290:137.
34. Zuo F, Su X, Wu KH. Phys Rev B 1998;58(17):11127.
35. Ma Y, Awaji S, Watanabe K, Matsumoto M, Kobayashi N. Solid State Commun 2000;113:671.
36. Brown PJ, Crangle J, Kanomata T, Matsumoto M, Neumann K-U, Ouladdial B, Ziebeck KRA. J Phys Condens Matter 2002;14:10159.
37. Chernenko VA, Pons J, Segui C, Cesari E. Acta Mater 2002;50:53.

38. Zheludev A, Shapiro SM, Wochner P, Schwartz A, Wall M, Tanner LE. Phys Rev B 1995;51(17):11310.
39. Segui C, Chernenko VA, Pons J, Cesari E, Khovailo V, Takagi T. Acta Mater 2005;53:111.
40. Yu SY, Liu ZH, Liu GD, Chen JL, Cao ZX, Wu GH, Zhang B, Zhang XX. Appl Phys Lett 2006;89:162503-1.
41. Krenke T, Acet M, Wassermann EF, Moya X, Manosa L, Planes A. Phys Rev B 2005;72:014412-1.
42. Oikawa K, Ito W, Imano Y, Sutou Y, Kainuma R, Ishida K, Okamoto S, Kitakami O, Kanomata T. Appl Phys Lett 2006;88:122507-1.
43. Koyama K, Okada H, Watanabe K, Kanomata T, Kainuma R, Ito W, Oikawa K, Ishida K. Appl Phys Lett 2006;89:182510-1.
44. Kainuma R, Imano Y, Ito W, Sutou Y, Morito H, Okamoto S, Kitakami O, Oikawa K, Fujita A, Kanomata T, Ishida K. Nature 2006;439:957.
45. Koyama K, Watanabe K, Kanomata T, Kainuma R, Oikawa K, Ishida K. Appl Phys Lett 2006;88:132505-1.
46. Kainuma R, Imano Y, Ito W, Morito H, Sutou Y, Oikawa K, Fujita A, Ishida K, Okamoto S, Kitakami O, Kanomata T. Appl Phys Lett 2006;88:192513-1.
47. Sutou Y, Imano Y, Koeda N, Omori T, Kainuma R, Ishida K, Oikawa K. Appl Phys Lett 2004;85(19):4358.
48. Brown PJ, Gandy AP, Ishida K, Kainuma R, Kanomata T, Neumann K-U, Oikawa K, Ouladdial B, Ziebeck KRA. J Phys Condens Matter 2006;18:2249.
49. Murakami Y, Yano T, Shindo D, Kainuma R, Oikawa K, Ishida K. Scripta Mater 2006;55:683.
50. Schlagel DL, Wu YL, Zhang W, Lograsso TA. J Alloy Compound 2000;312:77.

VITA

Andrew Brewer, son of Terry and Karen Brewer, and elder brother of Aimee Brewer, was born in Albuquerque, NM, USA in 1981. He graduated from the University of New Mexico with a Bachelor of Science degree in Mechanical Engineering in May 2004. In August 2004, he began study at Texas A&M University to pursue a master's degree in the Department of Mechanical Engineering. Upon completion of his research, he received a Master of Science degree in Mechanical Engineering in May 2007. Following graduation, Andrew will pursue a career with the United States federal government.

His permanent contact information is:
c/o Professor Ibrahim Karaman
Texas A&M University
Department of Mechanical Engineering
College Station, TX
77843-3123
E-mail: albrewe@gmail.com